12-17-2015

Measurement of ϕ Meson Production and Nuclear Modification in Cu+Au Collisions at $\sqrt{(sNN)}$ = 200 GeV with the PHENIX Detector at RHIC

Margaret Annette Jezghani
Georgia State University

MEASUREMENT OF ϕ MESON PRODUCTION AND NUCLEAR MODIFICATION IN Cu+Au COLLISIONS AT $\sqrt{s_{NN}} = 200$ GeV WITH THE PHENIX DETECTOR AT RHIC

by

MARGARET ANNETTE JEZGHANI

Under the Direction of Xiaochun He, PhD

ABSTRACT

The PHENIX experiment at the Relativistic Heavy Ion Collider (RHIC) has measured ϕ meson production and nuclear modification in asymmetric Cu+Au heavy-ion collisions at $\sqrt{s_{NN}} = 200$ GeV at both forward Cu-going direction ($1.2 < y < 2.2$) and backward Au-going direction ($-2.2 < y < -1.2$) rapidities. Due to its very short lifetime, the ϕ meson is an excellent probe for studying the hot and dense state of nuclear matter, referred to as the quark-gluon plasma (QGP), that is produced in high-energy heavy-ion collisions, such as those at RHIC. Furthermore, the absence of strong interactions between muons and the surrounding hot hadronic matter makes the $\phi \rightarrow \mu^+\mu^-$ decay channel particularly useful for studying nuclear matter effects on ϕ meson production. Additionally, the rapidity dependence of ϕ meson production in asymmetric heavy-ion collisions provides a unique means of accessing the entanglement of hot and cold nuclear matter effects. However, the large combinatorial

background produced at forward and backward rapidities in heavy-ion collisions results in a very challenging environment for extracting the ϕ meson signal. Accordingly, previous measurements at RHIC were limited to smaller collision species, *p*+*p* and *d*+Au. In this paper, a procedure for modeling and removing the backgrounds is detailed, and the first ϕ meson measurement at forward and backward rapidites in heavy-ion collisions at RHIC is presented. The ϕ meson invariant yield and nuclear-modification factor R_{CuAu} are reported as a function of the number of participating nucleons, rapidity, and transverse momentum in the kinematic region $1.2 < |y| < 2.2$ and $1.0 < p_T < 5.0\ \mathrm{GeV}/c$. Results of this analysis provide insight into the mixture of hot and cold nuclear matter effects on ϕ meson production in asymmetric heavy-ion collisions, bringing scientists one step closer to understanding the QGP.

INDEX WORDS: high-energy physics, nuclear physics, heavy-ion collisions, low-mass vector mesons, nuclear modification, phi meson, quark-gluon plasma, dimuons, strangeness

MEASUREMENT OF ϕ MESON PRODUCTION AND NUCLEAR MODIFICATION IN Cu+Au COLLISIONS AT $\sqrt{s_{NN}} = 200$ GeV WITH THE PHENIX DETECTOR AT RHIC

by

MARGARET ANNETTE JEZGHANI

A Dissertation Submitted in Partial Fulfillment of the Requirements for the Degree of

Doctor of Philosophy

in the College of Arts and Sciences

Georgia State University

2015

MEASUREMENT OF ϕ MESON PRODUCTION AND NUCLEAR MODIFICATION IN Cu+Au COLLISIONS AT $\sqrt{s_{NN}} = 200$ GeV WITH THE PHENIX DETECTOR AT RHIC

by

MARGARET ANNETTE JEZGHANI

Committee Chair: Xiaochun He

Committee: Murad Sarsour

Raphael Tieulent

Russel White

Electronic Version Approved:

Office of Graduate Studies

College of Arts and Sciences

Georgia State University

December 2015

DEDICATION

To my parents, Abbas and Sharon Jezghani, whose unfaltering love and support are the foundation of my success.

ACKNOWLEDGEMENTS

I would first like to thank my family and friends for all of their love and encouragement that has helped me to achieve this goal. My sisters, Amy and Katie, motivated and supported me whenever I needed it most. My Grandmother Annette and Uncle Mark never failed to let me know how proud they were, which was something I needed to hear from time-to-time. My Aunt KK and cousin Mary invited me on some memorable girls' weekends to help keep me refreshed and relaxed. My niece, Karrie, and nephews, Brice and Brooks, inspired me to push myself to be a good role model for them. My parents always encouraged me to pursue my dreams, no matter how difficult the road may be. Aaron Sprow, my boyfriend who is also a nuclear physicist, would regularly stop by my office for a coffee break and listen to the newest challenges in my analysis, all the while telling me how impressed he is with my work. And finally, I would like to acknowledge some of my wonderful friends whose support will always be appreciated: Lee Cook, Lee Ellen Dixon, Lilli Faraj, Thomas Legare, Ann Marie and Karen Lowman, Gretel Placer, Mila Raeva, and Olesya Sarajlic. This has been a long journey, and I will always be grateful for the family and friends that have stood by me through it all.

My graduate studies in nuclear physics would not have been possible without first receiving an excellent undergraduate education. First, I would like to thank Donald Singer of Georgia Perimeter College for helping me to complete the requirements for my associate's degree prior to my high school graduation. Next, I would like to recognize Richard Prior and Mark Spraker, the professors at UNG who first sparked my interest in nuclear physics. Furthermore, I would like to thank Sarah Formica, Claud Elliott, and Robin Webber of UNG for their continuing encouragement toward my success in physics. I would also like to thank Sergo Jindariani, Satyajit Behari, and Benedetto Di Ruzza at Fermi National Accelerator Laboratory;

Kenneth Watkins at Polymer Aging Concepts; and John Byrd and Derun Li at Lawrence Berkeley National Laboratory for providing me with the thrilling undergraduate research experiences that helped shape the scientist I am today.

Next, I would like to recognize my collaborators at Los Alamos National Laboratory (LANL), who took me in for half a year and provided significant contributions to this analysis. Melynda Brooks, my mentor at LANL, always had her door open for my questions – even in the middle of her lunch. I would also like to recognize Cesar da Silva, Ming Liu, Michael McCumber, Matthew Snowball, Matthew Durham, and the other members of my team at LANL for making physics fun and always being available for me to bounce ideas off of.

Lastly, I would like to recognize my adviser Xiaochun He for introducing me to the field of heavy-ion collisions, and Murad Sarsour and Raphael Tieulent for sparking my interest in the study of low-mass vector-meson production. Furthermore, I would like to thank the three of them in addition to my remaining committee member, Russel White, for all of their insight and support. And finally, I'd like to thank some former and current members of my group at Georgia State University, including Abhisek Sen, Laura Patel, Carola Butler, Liang Xue, Tristan Haseler, Olesya Sarajlic, Xiaohang Zhang, Hari Guragain, Ping Wong, Todd Elder, and others, for making PHENIX shifts, conferences, and days in the lab more exciting.

Thank you all.

This material is based upon work supported by the U.S. Department of Energy (DOE), Office of Science, Office of Workforce Development for Teachers and Scientists, Office of Science Graduate Student Research (SCGSR) award program. The SCGSR award program is administered by the Oak Ridge Institute for Science and Education for the DOE under contract number DE-AC05-06OR23100.

TABLE OF CONTENTS

LIST OF ABBREVIATIONS

A+A	nucleus-nucleus (symmetric)
A+B	nucleus-nucleus (asymmetric)
$A\varepsilon_{\mathrm{rec}}$	detector **a**cceptance and **e**fficiency for **rec**onstruction
ALICE	**A** **L**arge **I**on **C**ollider **E**xperiment
Au	gold
BBCs	**b**eam-**b**eam **c**ounters
BNL	**B**rookhaven **N**ational **L**aboratory
BRAHMS	**B**road **Ra**nge **H**adron **M**agnetic **S**pectrometers Experiment
CNM	**c**old **n**uclear **m**atter
Cu	copper
FVTX	**f**orward silicon **v**er**t**e**x** detector
GEANT	**ge**ometry **an**d **t**racking
HNM	**h**ot **n**uclear **m**atter
LHC	**L**arge **H**adron **C**ollider
MB	**m**inimum **b**ias
MuID	**m**uon **i**dentifier
MuTr	**m**uon **t**racker
PDG	**p**article **d**ata **g**roup
PISA	**P**HENIX **I**ntegrated **S**imulation **A**pplication
N_{coll}	number of binary nucleon-nucleon collisions
N_{part}	number of participating nucleons
p+A	**p**roton-nucleus

p+p	**p**roton-**p**roton
Pb	lead
PHENIX	**P**ioneering **H**igh **E**n**e**r**g**y **N**uclear **I**nteraction E**x**periment
QCD	**q**uantum **c**hromo**d**ynamics
QGP	**q**uark-**g**luon **p**lasma
R_{AA}	nuclear-modification factor
RHIC	**R**elativistic **H**eavy-**I**on **C**ollider
STAR	**S**olenoidal **T**racker **a**t **R**HIC
U	Uranium
VTX	silicon **v**er**t**e**x** tracker

LIST OF TABLES

LIST OF FIGURES

1 INTRODUCTION

One of the most captivating fields of physics today is ultra-relativistic heavy-ion collisions, a sub-field of nuclear physics in which scientists explore the frontier of Quantum Chromodynamics (QCD, or the fundamental theory of strong interactions) in a laboratory setting by employing cutting-edge technology. An example of such technology is the Relativistic Heavy-Ion Collider (RHIC) at Brookhaven National Laboratory (BNL) in Upton, New York, USA. RHIC is an extremely versatile accelerator capable of colliding various species, including proton-proton (p+p), proton-nucleus (p+A), and nucleus-nucleus (A+B) collisions. It is theorized that when the energy density of matter reaches about 1 GeV/fm^3, corresponding to a critical temperature of approximately 10^{12} K or 170 MeV, hadrons begin to break down into their constituent particles, quarks and gluons [1,2]. By colliding heavy ions at relativistic speeds, RHIC is able to reproduce this extraordinary type of matter, called the quark-gluon plasma (QGP), which has not existed since microseconds after the Big Bang. The main goal of RHIC is to study QGP and, in particular, the QCD phase transition itself [2] in order to quantify and characterize the properties of this hot, dense medium. In the remainder of this section, an introduction to the standard model and field of heavy-ion collisions is provided, followed by a discussion of previous measurements, and finally, an outline of the dissertation.

1.1 The Standard Model

The standard model is the name given to a comprehensive model that incorporates the most up-to-date knowledge of fundamental particles and how they interact. Throughout history, the information contained in the standard model has been experimentally studied and confirmed, starting with the discovery of the electron by J. J. Thomson in 1897 [3] and including the recent

observation of the Higgs boson at the Large Hadron Collider (LHC) in 2012 [4,5]. Today, nuclear and particle physicists, such as those who take data at RHIC, continue to study the fundamental particles and forces to help broaden our understanding of the standard model.

The classification of elementary particles as described by the standard model begins with three different species of particles: quarks, leptons, and gauge bosons. Quarks and leptons are both spin-½ particles, also called fermions, while bosons carry integer spin.

Quarks come in six different types, or flavors: up, down, charm, strange, truth, and beauty. Of these flavors, up and down are the lightest and most stable quarks, while truth and beauty are the heaviest quarks with the shortest lifetimes. It follows that the up and down quarks are the building blocks of all stable matter in the universe, as described in further detail below. In addition to carrying an electric charge, quarks also carry a color charge, and all composite particles formed via quarks are colorless.

Similar to quarks, leptons also come in six different types: electron, muon, and tau, and their associated neutrinos. The neutrino, which literally means “little neutral one” in Italian, is a neutral particle with very little mass, while the remaining three leptons all carry a charge and much larger mass.

Finally, gauge bosons are the force carriers. According to the standard model, there are only four fundamental forces: weak, electromagnetic, gravitational, and strong, and each force has an associated force-carrying particle called a boson. The electromagnetic force and weak force can be combined into a unified electroweak interaction, although that will not be described in detail in this paper. The force carriers for the electroweak force are the W and Z bosons and the photon, which is a massless, neutral particle. The W and Z bosons carry the weak force and act on quarks and leptons, while the photon carries the electromagnetic force and interacts with

all electrically charged particles. The graviton, which is the theorized force carrier for the gravitational interaction, is the only gauge boson in the standard model that has not yet been observed. The strong force is fundamentally mediated by gluons, massless, neutral particles that carry color charge and interact with partons, which is just a classification for a group that contains both quarks and other gluons. Since it is the force responsible for holding nuclei together, the strong force is also sometimes referred to as the nuclear force.

Together, the elementary particles and their associated antiparticles form all matter currently known. Composite particles are colorless and carry integer charge. Hadrons, which are made up of partons, come in two types: mesons (quark-antiquark pairs) and baryons (three quarks or three antiquarks bound together). The two most notable baryons are the proton (two up quarks and one down quark) and neutron (one up quark and two down quarks). Protons and neutrons, collectively called nucleons, come together to form nuclei, which are orbited by electrons inside of atoms. Atoms are the building blocks of all macroscopic matter in our universe.

1.1.1 The ϕ Meson

The ϕ meson was discovered at BNL, the same laboratory in which this experiment was conducted, by P. L. Connolly, et al. in 1963 [6]. As described in the previous section, mesons consist of a quark-antiquark pair. In the case of the ϕ meson, this is a strange-antistrange ($s\bar{s}$) pair, which means that the ϕ meson is, in fact, its own antiparticle. Although the strangeness carried by the two quarks cancels out, the ϕ meson contains hidden strangeness and may thus provide information on strangeness production and enhancement in QGP. Table 1.1 below lists

some of the characteristics of the ϕ meson, including the spin, mass, and quark content, as taken from the Particle Data Group (PDG) at Lawrence Berkeley National Laboratory [7].

Table 1.1. Properties of the ϕ meson.

Property	Value
Spin	1
Mass *m*	$1019.461 \pm 0.019\ \mathrm{MeV/c^2}$
Full width Γ	$4.266 \pm 0.031\ \mathrm{MeV/c^2}$
Lifetime τ	$(1.54 \pm 0.01) \times 10^{-22}$ s
Interactions	Strong, Weak
Electric charge	0
Quark content	$s\bar{s}$

The lifetime of the ϕ meson is very short, on the order of 10^{-22} seconds, after which it will decay to a more stable state. The probability that a particle will decay by process *i* during a time interval *dt* can be written as $k_i dt$, where k_i is simply the decay constant for process *i*. Many particles, including the ϕ meson, have several decay modes. In this case, the total decay constant *k* is just the sum of all possible decay constants, or:

$$k = \sum_{i=0}^{i<n} k_i \,, \tag{1.1}$$

where n is the total number of possible decay modes. It follows that the branching ratio BR_i for subprocess i can be defined as the number of particles decaying by that mode compared to the total number decaying, as described in Eq. 1.2,

$$BR_i = \frac{k_i}{k} \,. \tag{1.2}$$

Hence, the branching ratio can also be seen as a likelihood of a particle decaying by a particular mode. Some of the ϕ meson decay modes and the associated branching ratios are tabulated in Table 1.2.

Table 1.2. ϕ meson decay modes and branching ratios.

Decay mode	***BR***
$\boldsymbol{\phi \rightarrow \mu^+ + \mu^-}$	$(2.87 \pm 0.19) \times 10^{-4}$
$\boldsymbol{\phi \rightarrow e^+ + e^-}$	$(2.954 \pm 0.030) \times 10^{-4}$
$\boldsymbol{\phi \rightarrow K^+ + K^-}$	$(4.89 \pm 0.05)\ ) \times 10^{-1}$

The three decay modes listed in Table 1.2 are regularly used to measure ϕ mesons in nuclear and particle physics experiments. Although the ϕ meson decays to kaons nearly half of the time, kaons interact with the strong force and thus may be affected by the QGP itself. The leptonic decay modes, more specifically to dimuons or dielectrons, are arguably a more precise way to study the QGP since they do not experience any final-state effects and can carry important information about the QGP itself. Even so, the measurement of ϕ mesons via dimuons or dielectrons suffers a huge loss of statistics compared with the kaonic decay mode since these decays each only occur about 0.03% of the time. In this paper, dimuons are used to measure the ϕ meson in an extremely low-statistics and high-background environment for the very first time in heavy-ion collisions at RHIC.

1.2 Heavy-Ion Collisions

A heavy-ion is simply a relatively large atomic nucleus that is stripped of its electrons so that only the protons and neutrons of the nucleus remain. In heavy-ion collisions, the nucleons from nucleus A collide with those of nucleus B at speeds very close to the speed of light. Scientists then study the collision data via various observables in order to make physics conclusions. In this section, the collision kinematics and geometry will be presented, followed by a discussion of the various physics processes at play in such collisions.

1.2.1 Kinematics

In order to measure observables in heavy-ion collisions, a coordinate system must first be defined, such as the one for PHENIX shown in Fig. 1.1.

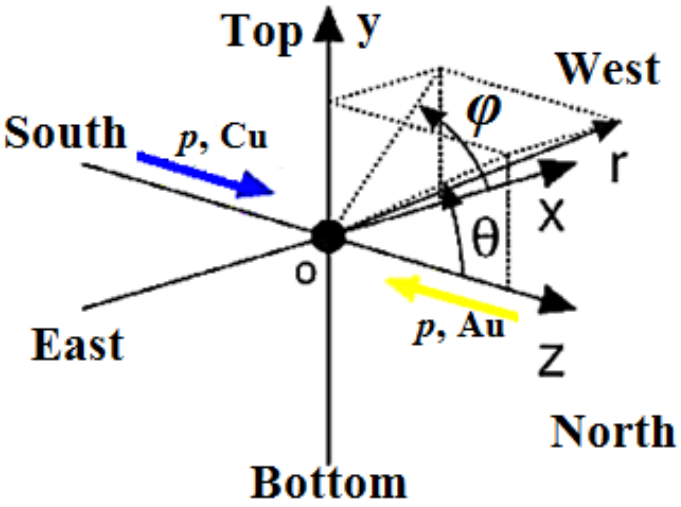

Figure 1.1. The global coordinate system for the PHENIX experiment with the Cu-going and Au-going directions clearly marked for this analysis.

The standard coordinate system in high-energy physics is defined relative to the beam axis. In Fig. 1.1, the z-axis is along the beam axis, with the origin placed at the center of the experiment. At PHENIX, the x-axis is the horizontal direction and the y-axis is the vertical direction. The particle direction can be determined by the polar angle θ and the azimuthal angle φ as shown in Fig. 1.1 and described in Eqs. 1.3 and 1.4 below,

$$\theta = \tan^{-1}\left(\frac{y}{z}\right), \tag{1.3}$$

$$\varphi = \tan^{-1}\left(\frac{y}{x}\right). \tag{1.4}$$

In high-energy physics, another useful way of describing the direction of the particle with respect to the beam axis is via the pseudorapidity η, which is defined as:

$$\eta = -\ln\left(tan\left(\frac{\theta}{2}\right)\right). \tag{1.5}$$

The pseudorapidity is equal to zero when the angle from the z-axis is 90 degrees, and it approaches infinity as the angle decreases to 0 degrees. Fig. 1.2 shows how the pseudorapidity changes as the angle from the beam axis increases.

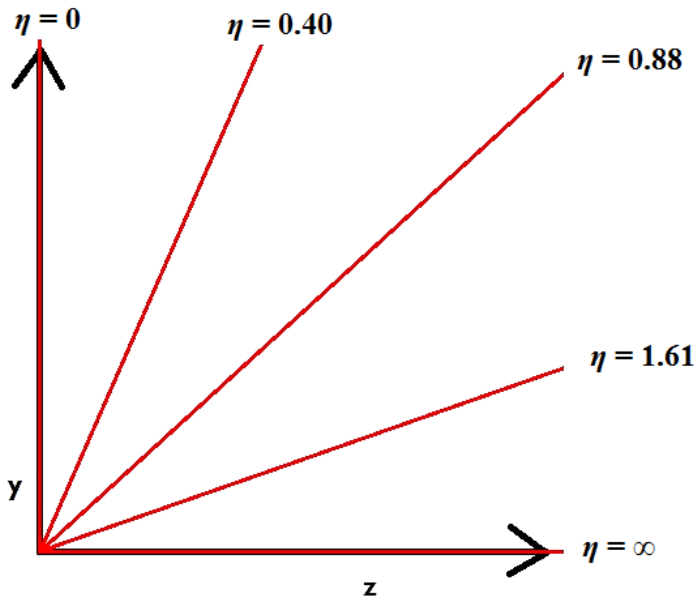

Figure 1.2. Pseudorapidity values for different angles from the beam axis.

In high-energy collisions, such as those at RHIC, the pseudorapidity η is approximately equal to the rapidity y, which is defined not by the direction of the particle, but rather by the energy E and the momentum along the beam axis p_z as described in Eq. 1.6 below:

$$y = \frac{1}{2}\ln\left(\frac{E-p_z}{E+p_z}\right). \tag{1.6}$$

The rapidity coverage of the PHENIX experiment is discussed in Chapter 2.

Another useful variable in high-energy physics is the center-of-mass energy $\sqrt{s_{NN}}$ for the collision of two particles with masses m_1 and m_2, which can be expressed as:

$$\sqrt{s_{NN}} = \sqrt{(E_1 + E_2)^2 - (\boldsymbol{p}_1 + \boldsymbol{p}_2)^2}\,, \qquad (1.7)$$

where E_1 and E_2 are the energies of particles 1 and 2, respectively, and $\boldsymbol{p}_1$ and $\boldsymbol{p}_2$ are the corresponding momenta. For this experiment, the center-of-mass energy is 200 GeV.

This analysis requires a measurement of the $\phi \rightarrow \mu^+\mu^-$ decay, which is a two-body decay as represented in Fig. 1.3.

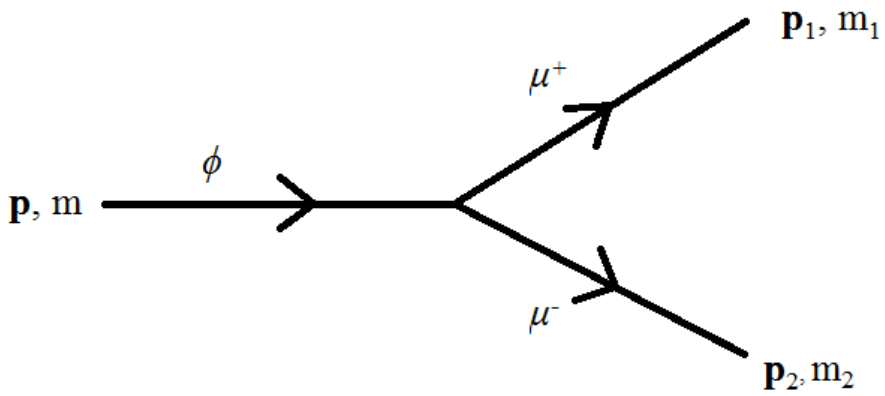

Figure 1.3. Diagram of the ϕ to dimuon decay.

In a two-body decay, a particle with invariant mass m and momentum $\boldsymbol{p}$ decays into two particles with masses of m_1 and m_2 and corresponding momenta $\boldsymbol{p}_1$ and $\boldsymbol{p}_2$. Due to the extremely short lifetime of the ϕ meson as discussed in Sec. 1.1.1, physicists are unable to directly measure the ϕ

meson itself. Instead, the decay products, in this case dimuons, are measured and used to reconstruct the parent particle, in this case a ϕ meson. Conservation of momentum means that the total momentum before the decay must be equal to that after the decay. Similarly, the total energy before the decay must be equal to the total energy after due to conservation of energy. Combining these two laws and recalling the relation $E^2 = p^2c^2 + m^2c^4$, the equation for the invariant mass of the parent particle can be derived as described in Eq. 1.8,

$$m = \sqrt{(E_1 + E_2)^2 - (\boldsymbol{p_1} + \boldsymbol{p_2})^2}\,. \tag{1.8}$$

The last kinematic variable that needs to be defined for this analysis is the transverse momentum of the particle, which is defined as described in Eq. 1.9,

$$p_T = \sqrt{p_x^2 + p_y^2}\,, \tag{1.9}$$

where p_x and p_y are the particle momenta in the x- and y-directions, respectively.

1.2.2 Collision Geometry

In addition to studying the particle kinematics, it is also important to study details of the collision itself, including the geometry. The Glauber Model can be utilized to analyze the collision between two ions whose centers are separated by impact parameter *b*, which is a distance perpendicular to the beam axis, as seen in Fig. 1.4.

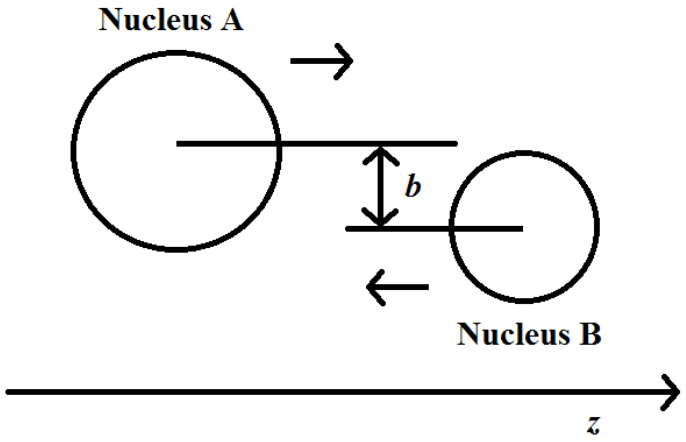

Figure 1.4. Schematic of the collision of two nuclei separated by impact parameter *b*.

The possible values of impact parameter for a specific collision system define the centrality of a collision. If the impact parameter is very small, the collision is said to be central, and a large impact parameter refers to a peripheral collision. These possible values can be separated into centrality bins, where 0% is the most central and 100% is the most peripheral. The reaction-plane is defined by the direction of the impact parameter and the beam axis as shown in Fig. 1.5.

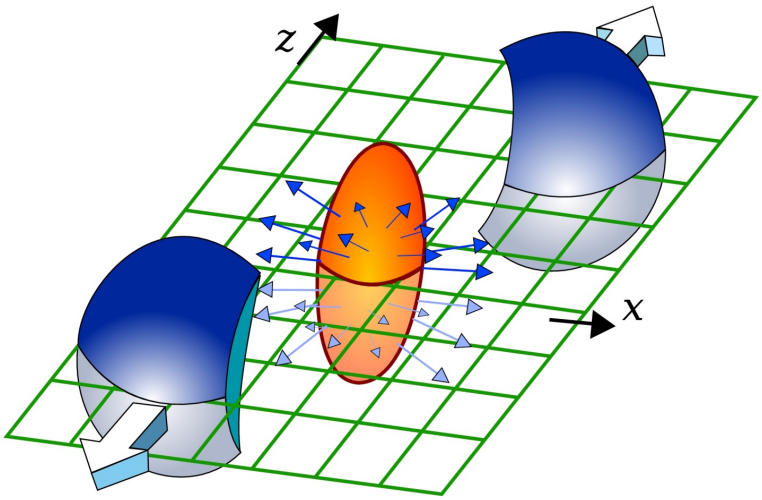

Figure 1.5. Sketch of the reaction plane in a heavy-ion collision.

In the Glauber Model, the ions are considered as two groups of nucleons that are described by the nuclear density distribution function ρ given in Eq. 1.10, where ρ_0 is the nucleon density at the center of the nucleus, w is a measure of the deviation of the nuclear shape from a sphere, r is the distance from the center of the nucleus to the nucleon, R is the nuclear radius, and a is the Woods-Saxon diffuseness parameter [8],

$$\rho(r) = \rho_0 \frac{1+w\left(\frac{r}{R}\right)^2}{1+e^{\frac{r-R}{a}}}. \tag{1.10}$$

During the collision of two ions, the nucleons that undergo one or more nucleon-nucleon, or binary, collision are called participants, while all other nucleons are called spectators. Figure 1.6 shows the overlap region, which contains the participants, and the outside region, where the spectators exist. The spectators are also shown in Fig. 1.5 by the nucleons that continue to move along the beam axis after the collision.

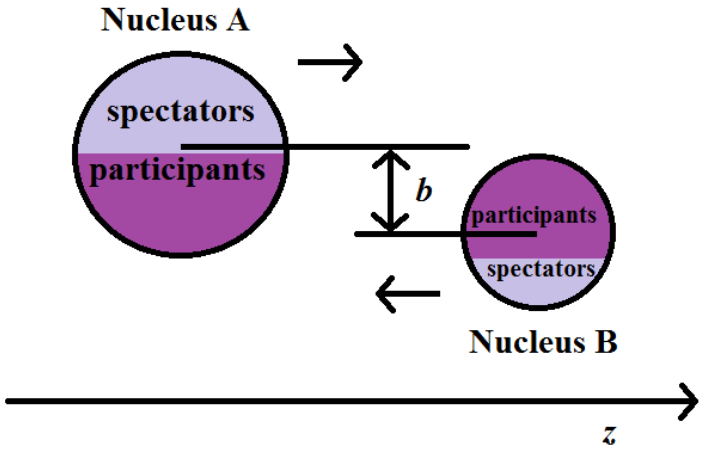

Figure 1.6. The regions of spectators and participants in nuclei A and B during a heavy-ion collision.

Glauber Monte Carlo simulations provide a way to estimate important physics variables, such as the number of participants or number of participating nucleons, N_{part}, and the number of binary collisions, N_{coll}. Figure 1.7 shows how two different collisions with the same number of participating nucleons can have a dramatically different number of collisions.

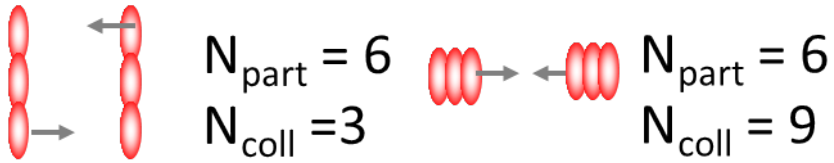

Figure 1.7. The number of participating nucleons and number of collisions for two different geometries.

To further analyze heavy-ion collisions, the geometry can be studied via the eccentricity, which is a measurement of the deviation of a conic section from the shape of a circle. For example, a circle has an eccentricity of 0, a parabola has an eccentricity of 1, and an ellipse has an eccentricity somewhere between 0 and 1 [10]. There are two different kinds of eccentricity that can be calculated for heavy-ion collisions: the reaction-plane eccentricity ϵ_{RP} and the participant eccentricity ϵ_{part}, which are defined in Eq. 1.11 and 1.12, where σ_x^2 and σ_y^2 are the variances of the nuclear distribution in the x- and y-directions, respectively, and σ_{xy}^2 is the covariance [11],

$$\epsilon_{RP} = \frac{\sigma_y^2 - \sigma_x^2}{\sigma_y^2 + \sigma_x^2} \ , \tag{1.11}$$

$$\epsilon_{part} = \frac{\sqrt{(\sigma_y^2 - \sigma_x^2)^2 + 4\sigma_{xy}^2}}{\sigma_y^2 + \sigma_x^2}\ , \tag{1.12}$$

ϵ_{RP} is the eccentricity calculated with respect to the reaction-plane, which means that it strongly depends on the initial geometry of the collision [12]. ϵ_{part} is the eccentricity of the ellipse drawn by the participants, so it can change on an event-by-event basis due to fluctuations in the position of the nucleons [12].

Using the PHOBOS Glauber Monde Carlo code from Ref. [13], half a million events were generated with varying impact parameters for each of the three heavy-ion collision systems that occurred in PHENIX in 2012: Au+Au at 200 GeV, Cu+Au at 200 GeV, and U+U at 193 GeV. The code was updated for U+U collisions, which are unique in that the uranium ion is both asymmetric and capable of rotation. The asymmetry of the U nucleus was accounted for by replacing R in Eq. 9 with R' as defined in Eq. 1.13 below, where $\beta_2$and β_4 are deformation constants and $Y_2^0(\theta)$ and $Y_4^0(\theta)$ are the spherical harmonics,

$$R' = R[1 + \beta_2 Y_2^0(\theta) + \beta_4 Y_4^0(\theta)]\,. \tag{1.13}$$

To include the rotation of the U nucleus, Eugler angles were introduced into the PHOBOS code. The input parameters used in this study are taken from Refs. [12] and [13] and are summarized in Table 1.3 below, where *A* is the total number of nucleons and *Z* is the number of protons.

Table 1.3. Characteristics of Copper, Gold and Uranium nuclei.

Parameter	Cu	Au	U
A	63	197	238
Z	29	79	92
R	4.2 fm	6.38 fm	6.81 fm
a	0.596 fm	0.535 fm	0.6 fm
w	0 fm	0 fm	0 fm
β_2	--	--	0.28
β_4	--	--	0.093

It is important to note that this measurement only used the Cu+Au dataset. However, the results of this simulation allow for a comparison of all three systems, providing some insight into what can be expected when this analysis is repeated in the Au+Au and U+U datasets. A typical Glauber event for Cu+Au collisions with b = 5.0 fm is shown in Fig. 1.8. In panel (a) on the left, the event is shown in the xy-plane, and in panel (b) it is shown in the xz-plane. The smaller Cu nucleus is shown in red, while the larger Au nucleus is plotted in blue. The closed circles represent the participants, while the open circles represent the spectators.

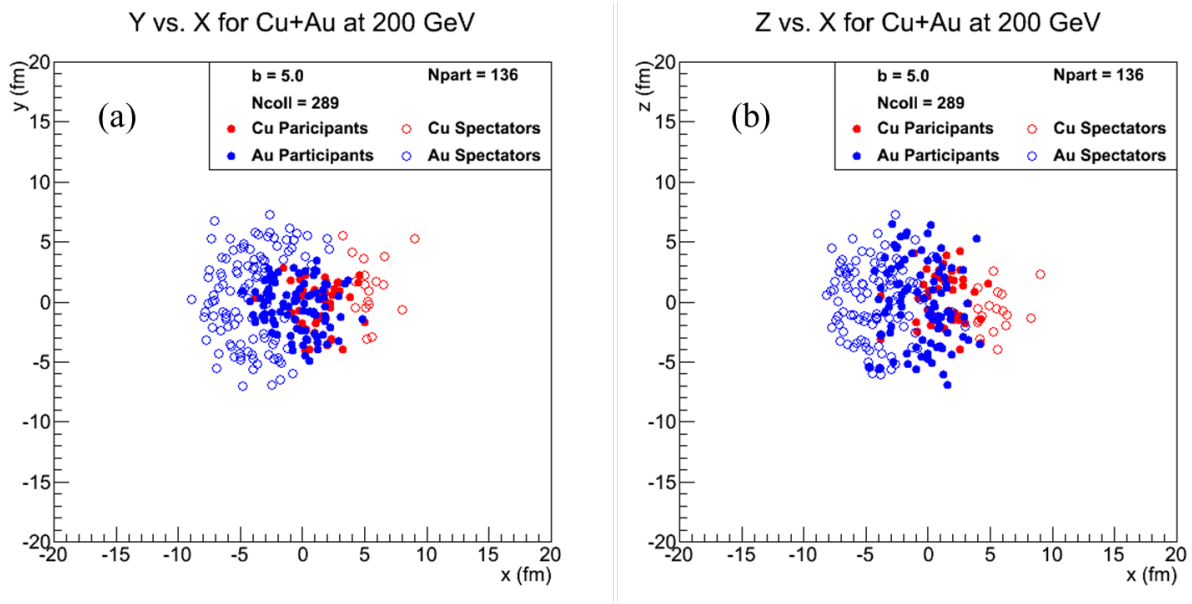

Figure 1.8. A typical Glauber event for Cu+Au collisions with b = 5.0 fm in (a) the xy-plane and (b) the xz-plane.

Figures 1.9 and 1.10 show the average number of collisions vs. impact parameter and average number of participants vs. impact parameter, respectively, for the three collision systems. The error bars in these plots are smaller than the data points themselves since the simulation was not statistically limited. As can be seen in the figures, N_{part} and N_{coll} have the largest values in U+U collisions (in blue) and smallest values in Cu+Au collisions (in black), while the values in Au+Au collisions (in red) fall in the middle just as one would expect. Furthermore, N_{part} and N_{coll} decrease as a function of impact parameter. This is because the most central collisions, which occur at the smallest values of b, have the largest number of collisions and participating nucleons, whereas these values are much smaller for peripheral collisions, which are defined at the largest possible values of b. Also, N_{part} is typically smaller than N_{coll}, indicating that participating nucleons often participate in more than one collision.

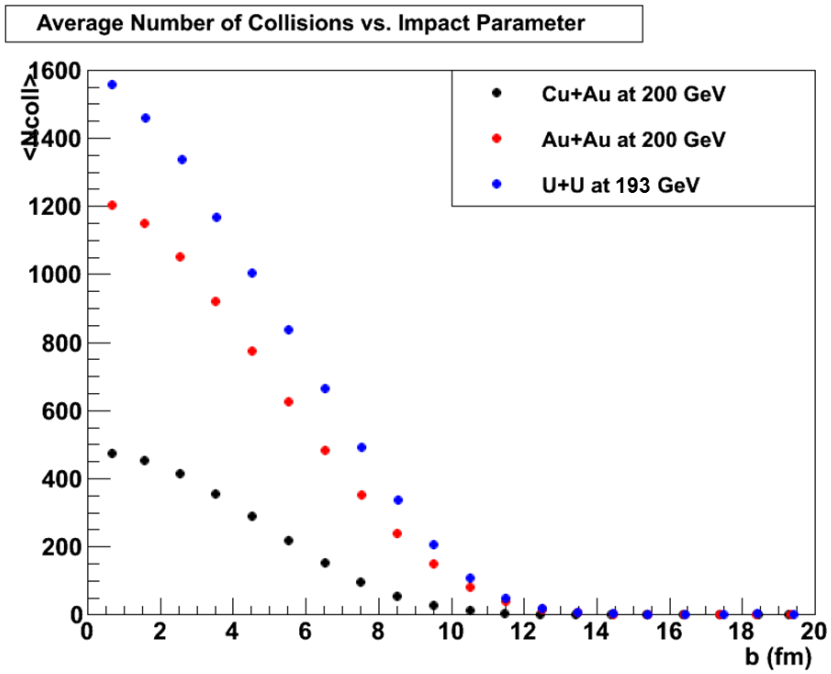

Figure 1.9. Average number of binary collisions as a function of impact parameter.

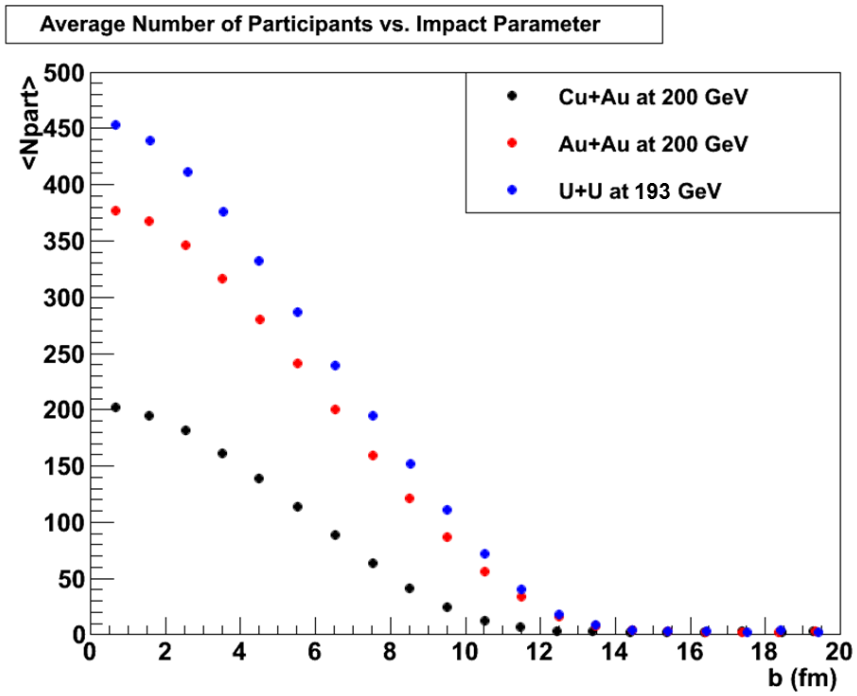

Figure 1.10. Average number of participating nucleons as a function of impact parameter.

The geometry of heavy-ion collisions, which can be studied via Monte Carlo simulations using the Glauber Model, provides important information that can help to extract physics from collision data. The details described in this section will be helpful in understanding the analysis techniques and results in later chapters.

1.2.3 Hot Nuclear Matter

Now that the basics of collision kinematics and geometry have been covered, it is time to explore the more exciting physics processes that occur in heavy-ion collisions, most notably, the formation of the hot nuclear matter (HNM), or QGP. As briefly discussed at the beginning of this chapter, experimental evidence suggests that at sufficiently high temperature and density, a phase transition occurs such that quarks and gluons become deconfined. It is theorized that this strongly-interacting matter may have existed in the early universe. The time evolution of the universe is shown in Fig. 1.11, which was provided by the PDG at Lawrence Berkeley National Laboratory [14]. Figure 1.11 details the chronology of the universe, starting with the Big Bang and inflation, continuing to the formation of nucleons at 10^{-4} seconds and nuclei at 10^{2} seconds, and ending at present day, which lies at 13.8×10^{9} years. At just a few microseconds after the Big Bang, before quarks and gluons became confined in hadrons, the QGP may have existed. In Fig. 1.11, there is a mark for heavy-ion collisions at RHIC around this approximate time because it is possible to reproduce this unique state of matter in a laboratory setting via high-energy collisions in particle accelerators.

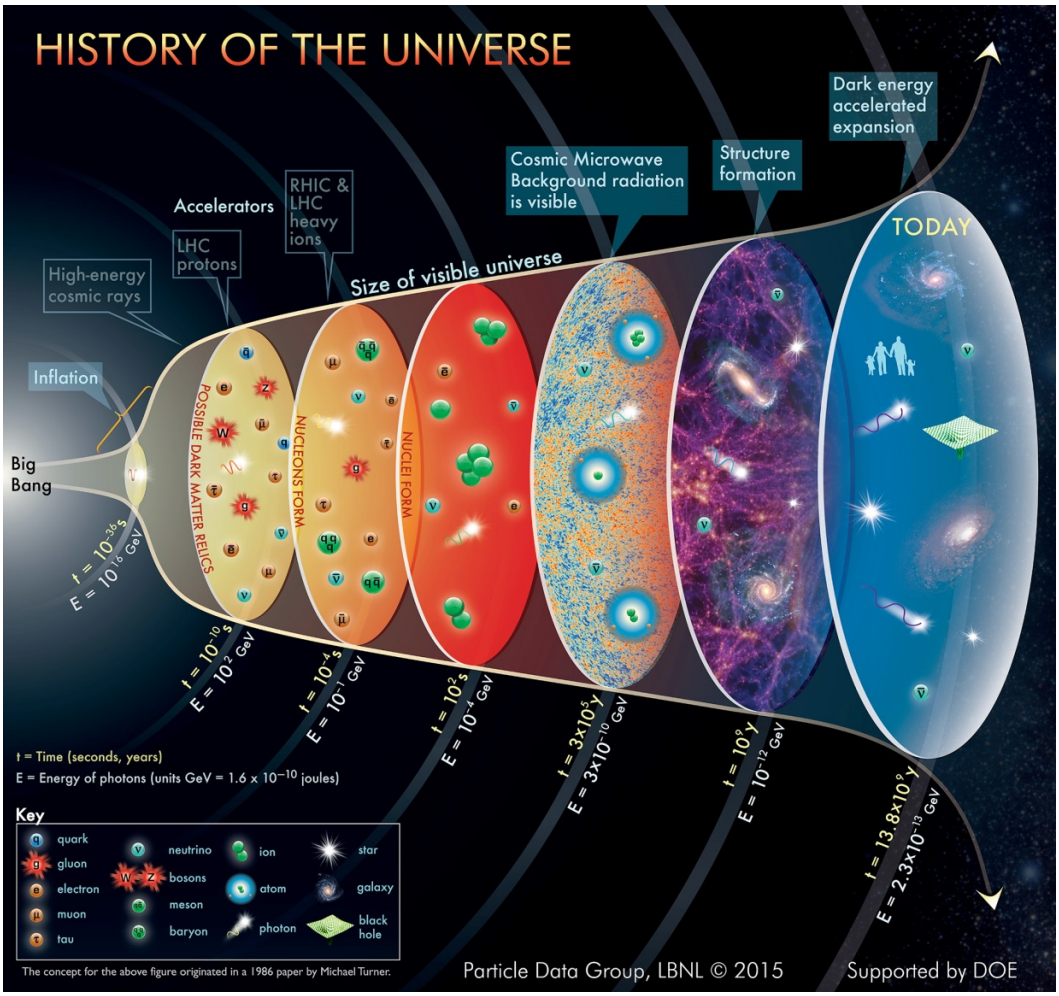

Figure 1.11. The time evolution of the universe from the Big Bang to present day.

The phase transition from normal nuclear matter into HNM occurs when the energy density of matter reaches about 1 GeV/fm^3, corresponding to a critical temperature of approximately 10^{12} K or 170 MeV [1,2]. For comparison, the necessary energy density required for QGP to form is about an order of magnitude larger than the energy density of a normal atomic nucleus. To better understand the conditions for this phase transition, the QCD phase diagram is shown in Fig. 1.12, which was provided by BNL. At low temperature and density, normal atomic nuclei are able to exist. Moving along the x-axis, neutron stars lie at very high density but low temperature. At extremely high temperature and density, the QGP is formed.

Fig. 1.12 shows where the matter created by the LHC (green) and RHIC (blue) particle accelerators exist on the phase diagram.

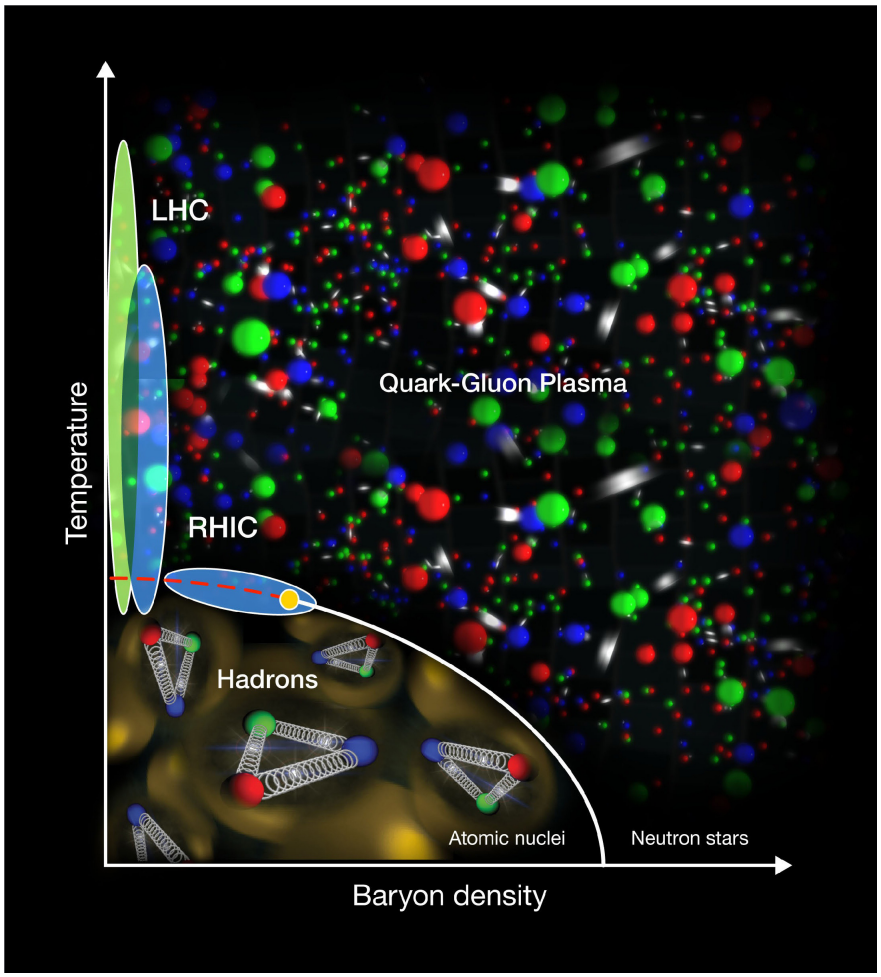

Figure 1.12. The QCD phase diagram.

Analogous to the different stages of the early universe shown in Fig. 1.11, the time-development of heavy-ion collisions can also be broken down into several steps as seen in Fig. 1.13, which was taken from Ref. [14]. The steps are as follows [15]:

1. Thermalization: Within 1 fm/c, corresponding to 3×10^{-24} s, the quarks and gluons reach thermal equilibrium, and a locally thermalized QGP is formed.

2. Hydrodynamic expansion: The evolution of the system at this stage can be described by relativistic hydrodynamics equations, including the usual conservation laws.

3. Freeze-out: This is the last step of a heavy-ion collision. The system cools and the momentum distributions of the hadrons "freeze." After this point, the particles no longer change in time as they move toward the detectors. Thus, measurements made by the detectors can provide information on the hadrons immediately before the freeze-out.

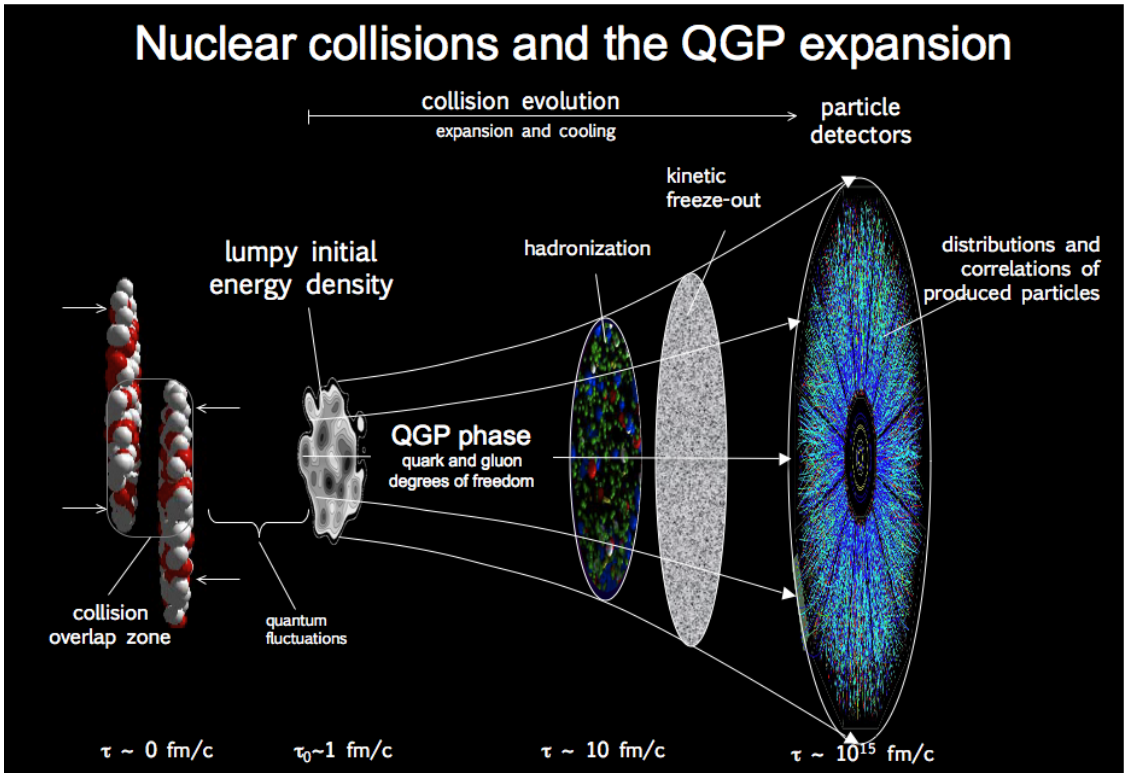

Figure 1.13. The time-evolution of a heavy-ion collision.

1.2.4 The Nuclear Modification Factor

As discussed in the previous section, physicists believe that heavy-ion collisions provide a means to "look back in time" and study the early universe by measuring the signature of the QGP. This is typically accomplished by comparing different observables measured in A+B collisions to those measured in p+p collisions, where QGP is not formed, at the same center-of-mass energy $\sqrt{s_{NN}}$. Modifications in A+B collisions compared to the p+p baseline, scaled by the number of binary nucleon-nucleon collisions N_{coll}, may be due to QGP production in heavy-ion collisions. One way to quantify the nuclear matter effects on particle production in heavy-ion collisions is by calculating the ratio of the particle yields in heavy-ion collisions to that in p+p collisions. This ratio, called the nuclear modification factor R_{AB}, is defined as:

$$R_{\text{AB}} = \frac{\frac{\mathrm{d}^2 N_{\text{AB}}}{\mathrm{d}y\mathrm{d}p_T}}{N_{\text{coll}} \times \frac{\mathrm{d}^2 N_{pp}}{\mathrm{d}y\mathrm{d}p_T}}, \tag{1.14}$$

where N_{AB} and N_{pp} are the number of particles produced in the A+B and p+p collisions, respectively, and dy and dp_T are the rapidity and transverse momentum bins. N_{coll} is determined from a Glauber Model Monte Carlo simulation as described in Sec. 1.2.2.

In this paper, the yields and nuclear modification factors for ϕ meson production in Cu+Au collisions at 200 GeV are calculated using Eq. 1.14 and presented as a function of rapidity, transverse momentum, and number of participating nucleons. More details on this calculation, as well as the measurement of the yields, can be found in Chapter 3.

1.2.5 Cold Nuclear Matter

Although the nuclear-modification factor introduced in the previous section is intended to provide insight into the HNM effects, there are also cold nuclear matter (CNM) effects that exist regardless of whether the QGP is formed. These effects are due to normal nuclear matter and must be explored and accounted for before any claims about QGP can be made. The CNM effects may include nuclear shadowing, gluon saturation, radiative energy loss, and the Cronin effect, which are all briefly described in this section.

Nuclear shadowing is the name given to the modification of parton distribution functions (PDFs) within a nucleus. This effect can be quantified by comparing PDFs to nuclear parton distribution functions (nPDFs). PDFs and nPDFs describe the probability density of quarks and gluons in free nucleons and in nucleons confined to nuclei, respectively. Nuclear shadowing raises from the fact that nPDFs are not a simple superposition of the PDFs of the constituent nucleons. Therefore, the parton-modification factor is defined as the ratio of the nPDF to PDF, scaled by the total number of nucleons. The parton-modification factor can provide insight into CNM effects in manner that is very similar to the nuclear-modification factor and HNM effects. This factor is defined in Eq. 1.15,

$$R_i^A = \frac{f_i^A(x,Q^2)}{A \times f_i(x,Q^2)} \ , \tag{1.15}$$

where R_i^A is the parton-modification factor for parton i in atomic nucleus with atomic number A, f_i^A is the nPDF for a nucleon confined to nucleus A, f_i is the PDF for a free nucleon, x is the momentum fraction carried by the parton, and Q^2 is the momentum transfer.

Gluon saturation refers to the saturation of the PDF for gluons. For small *x*, the number of gluons inside protons and neutrons quickly begins to dominate compared to quarks and antiquarks. As *x* becomes smaller and smaller, the gluon density becomes so large that individual gluons begin to overlap, leading to a saturation of the gluon PDF.

Radiative energy loss is simply energy loss due to radiation within the QGP. This is when a particle radiates energy in the form of an exchange of gluons as it traverses the HNM, causing the *x* to decrease, and thus affecting the PDF.

The Cronin effect is the last CNM effect that will be discussed in this paper. It is the observation that p_T distributions of particles in *p*+A collisions differ from those in *p*+*p* collisions. It is often attributed to multiple scattering of the incoming parton inside the target nucleus [16,17].

1.3 Previous Measurements & Motivation

The PHENIX collaboration has previously measured ϕ meson production in the forward region ($1.2 < |y| < 2.2$) via the dimuon decay channel in both *d*+Au and *p*+*p* collisions at 200 GeV [18,19] as well as at midrapidity ($|y| < 0.35$) via dielectrons in *p*+*p*, *d*+Au, Cu+Cu, and Au+Au collisions [20-22]. In *d*+Au collisions, a suppression was observed in the forward (*d*-going) direction, and an enhancement was seen at backward (Au-going) rapidity. This same behavior was also observed for open heavy flavor and inclusive charged hadrons in *d*+Au collisions at PHENIX [23,24]. This might indicate similar CNM effects on ϕ meson, open heavy flavor, and inclusive charged hadron production mechanisms. In Cu+Cu and Au+Au collisions at midrapidity [21], the results were found to be consistent with HNM rather than CNM predictions, indicating that QGP had the greatest effect on ϕ meson production.

ϕ meson production has also been measured by the STAR collaboration at midrapidity in Cu+Cu and Au+Au collisions [25,26] and by the ALICE collaboration at a higher center-of-mass energy at large rapidity in p+p and p+Pb collisions [27] and at midrapidity in Pb+Pb collisions [28].

Prior to this study, the ϕ meson signal had never been extracted in heavy-ion collisions in the forward or backward rapidity regions at RHIC due to the overwhelming background contribution in the low-mass region. In this analysis, a technique for modeling backgrounds and extracting the resonance in the ϕ meson mass region is developed and applied in order to measure ϕ meson production and nuclear modification in Cu+Au collisions at forward and backward rapidities at RHIC. The rapidity dependence of ϕ meson production in asymmetric Cu+Au collisions provides a unique way to investigate the entanglement of HNM and CNM effects and accessing different initial- and final-state effects. Comparison to previous measurements may shed light on the physics processes that affect ϕ meson production in Cu+Au collisions. The results of this analysis have been published in Ref. [29] and will be detailed in the remainder of this paper.

1.4 Dissertation Outline

In this dissertation, the first measurement of ϕ meson production and nuclear modification at forward and backward rapidities in heavy-ion collisions at RHIC is reported. Chapter 2 is an introduction to the PHENIX experiment on the RHIC particle accelerator. In Chapter 3, the data analysis is discussed in detail and, a technique for modeling backgrounds and extracting the ϕ meson signal is reported. Chapter 4 provides all results of this analysis. In

Chapter 5, the results are concluded and there is a discussion about future theoretical models and experimental measurements that are needed.

2 EXPERIMENT

2.1 The Relativistic Heavy-Ion Collider (RHIC)

RHIC is a high-energy particle accelerator located at BNL that collides various species, including p+p, Au+Au, Cu+Cu, Cu+Au, U+U, d+Au, ^{3}He+Au, and more, at energies ranging from $\sqrt{s_{NN}} = 7 - 200$ GeV for the goal of studying HNM and CNM effects. In addition, RHIC collides polarized protons at energies up to 510 GeV for the purpose of studying the proton spin. RHIC is the first machine in the world capable of colliding heavy ions, and it is the last remaining collider in the United States of America. At RHIC, two beams of ions are accelerated in opposite directions around a 2.4-mile ring at 99.995% the speed of light and allowed to collide at six different interaction regions. Four of these six points contain the RHIC experiments: PHOBOS, BRAHMS, STAR, and PHENIX, which all became operational in 2000. RHIC and its four experiments have provided extensive experimental evidence to confirm the formation of QGP in high-energy heavy-ion collisions [30-33]. In 2006, PHOBOS and BRAHMS were decommissioned, with PHENIX and STAR expected to follow about one decade later.

A schematic of RHIC can be seen in Fig. 2.1, which was provided by BNL. First, the Electron Beam Ion Source (EBIS) creates highly charged ion beams and accelerates them via linear accelerators into the Booster. Here, a circular Booster accelerates the ions to higher and higher energies before directing them into the Alternating Gradient Synchrotron (AGS). When they enter the AGS, the ions are traveling at about 37% the speed of light, but by the time they leave this accelerator, they are traveling at 99.7% the speed of light. At this point, the ions enter RHIC, where they receive one final boost of energy from radio waves to reach 99.995% the speed of light. Figure 2.1 shows each of these steps, as well as the location of the two currently

operating experiments at RHIC: PHENIX and STAR. PHENIX, the experiment used in this analysis, is discussed in more detail in the following section.

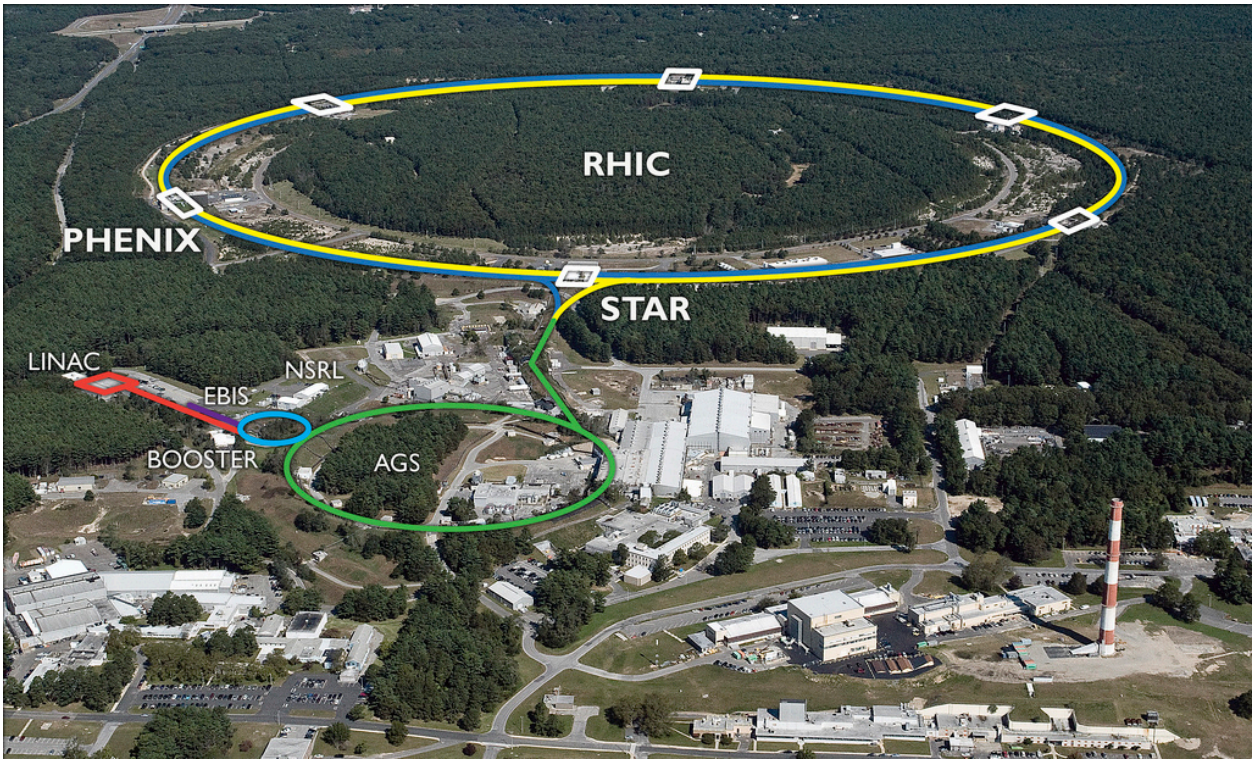

Figure 2.1. A diagram of the RHIC accelerator complex.

2.2 The Pioneering High Energy Nuclear Interaction Experiment (PHENIX)

The PHENIX detector was designed and optimized for the measurement of rare probes of the HNM produced in heavy-ion collisions at RHIC. In addition to studying the properties of the QGP, the PHENIX experiment is also dedicated to measurements of proton-spin asymmetries, which is outside of the scope of this paper. The PHENIX detector is described in Ref. [24], and a schematic of the 2012 setup is shown in Fig. 2.2 below. It consists of four separate spectrometers, referred to as "arms." The central arms, shown in Fig 2.2(a) below, were not used

in this analysis; thus, they will only be described briefly. The forward and backward muon arms, shown in Fig. 2.2(b), will be introduced here and then described in more detail in Sec. 2.2.1.1.

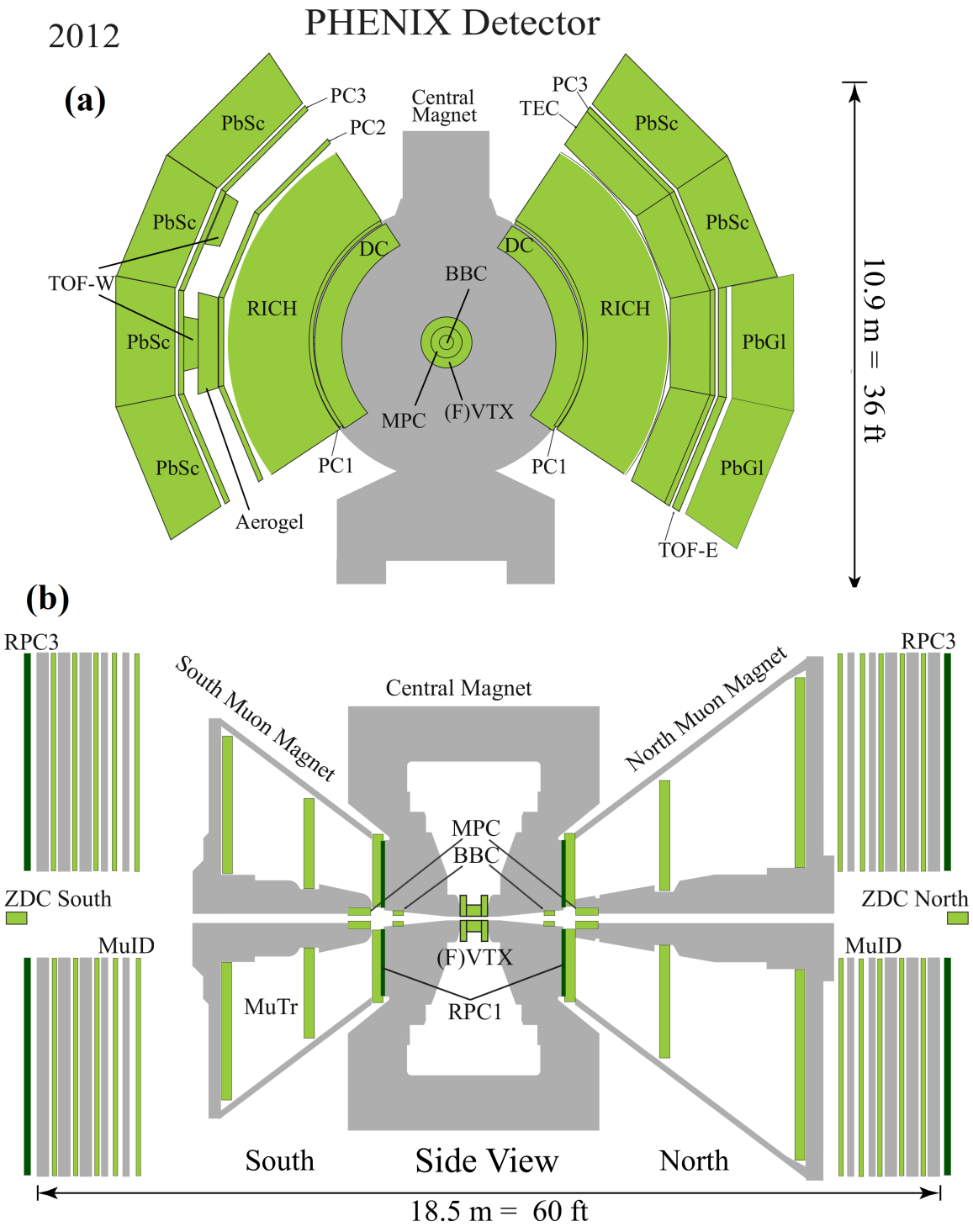

Figure 2.2. A schematic of the PHENIX detector, including the (a) central arms and (b) forward and backward muon arms during 2012.

The central arms cover the pseudorapidity range $|\eta| < 0.35$. They are separated into the east and west arms, each covering $\Delta\varphi = \frac{\pi}{2}$ for a full azimuthal coverage of π radians. This part of the detector is optimized for measuring hadrons, photons, and electrons by use of drift chambers (DC) and pad chambers (PC) for tracking and momenta determination, ring imaging Čerenkov (RICH) detectors for electron identification, and an electromagnetic calorimeter (EMCal) for the measurement of particle energy and spatial position.

The forward and backward arms shown in Fig. 2.2(b) cover a range in pseudorapidity of $1.2 < |\eta| < 2.2$ with full azimuthal coverage, $\Delta\varphi = 2\pi$ radians. The muon arms consist of absorbers to enhance the muon-to-hadron acceptance, a muon tracker (MuTr) to measure the muon momenta, and a muon identifier (MuID) to identify muons. In 2012, a forward silicon vertex detector (FVTX) was added to the existing muon arm for precise muon tracking and vertexing; however, due to low statistics during the RHIC 2012 Cu+Au runs, the FVTX tracks were not used. Instead, a precise vertex was provided by the FVTX and the silicon vertex tracker (VTX). The following section provides a more detailed look at muon detection in PHENIX as it relates to this analysis.

2.2.1 Muon Detection in PHENIX

The absence of strong interactions between muons and surrounding HNM indicates that the analysis of muons is an excellent probe into the properties of the QGP formed in high-energy heavy-ion collisions. This paper presents the measurement of $\phi \to \mu^+\mu^-$ in Cu+Au collisions, and the relevant detectors for this measurement are the MuID and MuTr [35], which were briefly introduced above, the two beam-beam counters (BBCs) [36], the VTX [37], and the FVTX [38]. Each of these subsystems can be seen in Fig. 2.2(b) as well as Fig. 2.3, which shows a cross-

section of the PHENIX detector next to two humans for scale. In the remainder of this chapter, each of the detectors relevant to this analysis is described.

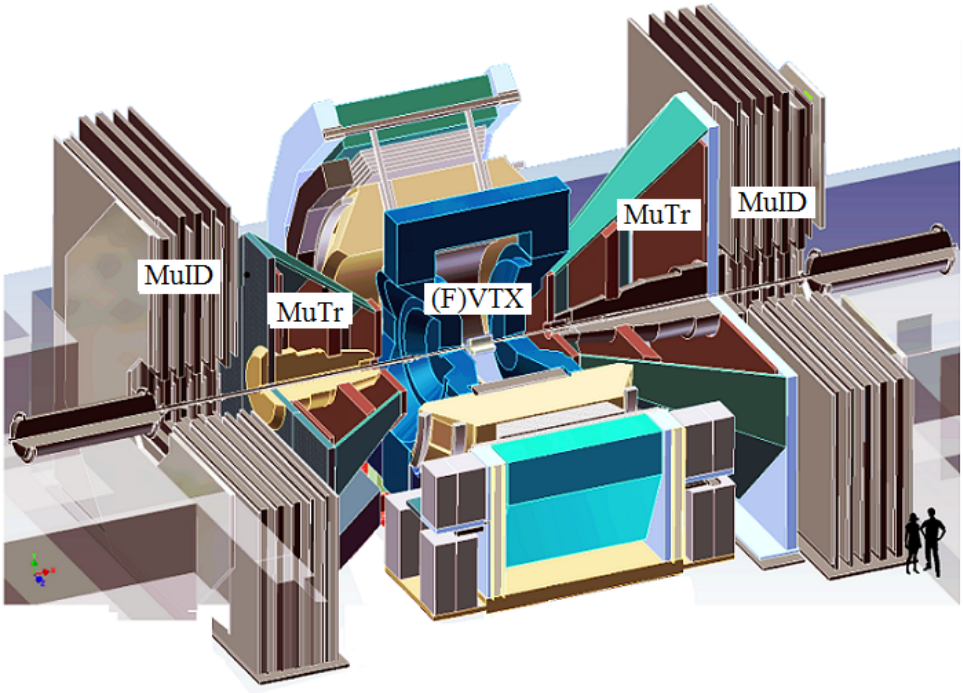

Figure 2.3. A cross-section of the PHENIX detector.

2.2.1.1 Muon Arms

The muon system in PHENIX is separated into the north (forward rapidity) and south (backward rapidity) muon arms. Each muon arm is made up of four subcomponents: the absorber, the magnet, the MuTr, and the MuID. Prior to 2010, the absorbers consisted of 19 cm of copper and 60 cm of iron. An additional steel absorber material of 36.2 cm was added in 2010 for the purpose of enhancing the muon yield relative to the hadronic background.

Following the absorbers, the next component in each muon arm is the MuTr. Designed for precision tracking of muons, the MuTr has a mass resolution of $\sigma(m)/m \approx \frac{6\%}{\sqrt{m}}$, allowing for the separation of the ρ+ω peaks from the ϕ meson peak, which is crucial for this analysis. The MuTr, shown in Fig. 2.4 below, consists of three stations containing a mixture of straight and stereo cathode chambers in a radial magnetic field with an integrated bending power of 0.8 T·m. The first station, closest to the collision point, is divided into quadrants, while the remaining two stations are divided into octants. Within each station are gaps – three for the first two stations and two for the station farthest from the collision region – that contain an anode plane, a gas gap, and a cathode plane.

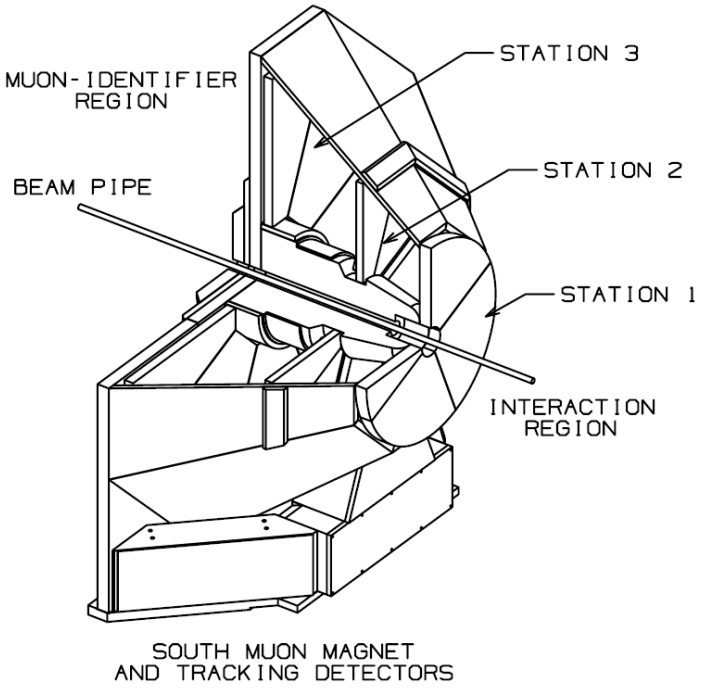

Figure 2.4. A schematic of the south muon magnet and MuTr detector showing the location of the three stations with respect to the beam pipe, MuID, and interaction region.

When a charged particle moves through the MuTr, cathode hit information is recorded in each station. Groups of cathode hits are combined together to form clusters, and clusters are fit by line segments to form coordinates. These coordinates then come together to form a muon candidate track. Using basic physics for the motion of a charged particle moving through a magnetic field, the momentum of the muon candidate is determined from the bend of the track within the magnetic field. Figure 2.5 shows a schematic of the muon arms magnetic polarity during the Cu+Au run from 2012.

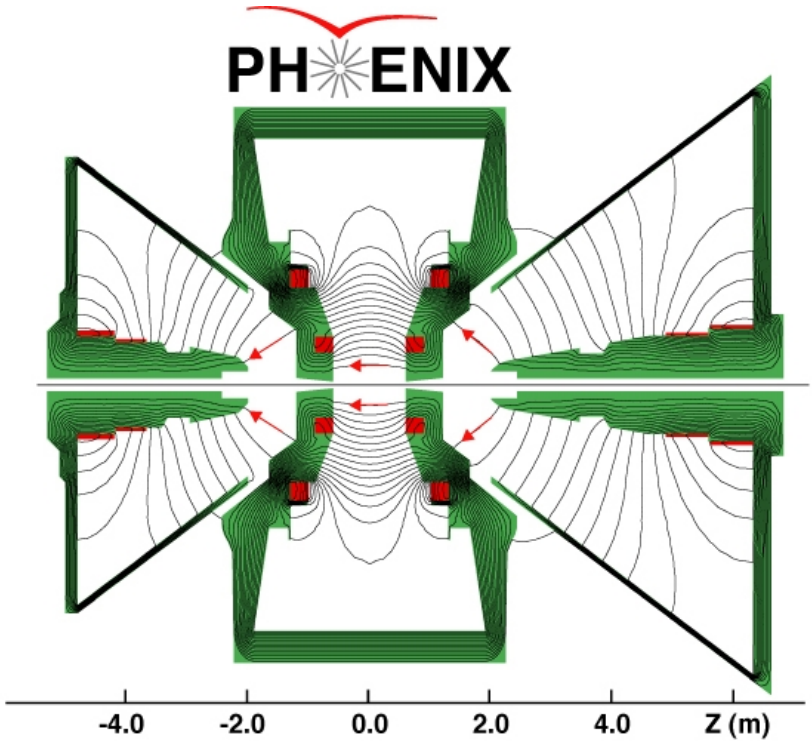

Figure 2.5. Magnetic field lines for the coils in combined (++) mode. This was the polarity used for taking data during the 2012 Cu+Au run at 200 GeV.

Finally, the last component in each muon arm is the MuID. This sub-detector consists of five alternating steel absorbers and Iarocci tubes to further reduce the number of hadrons that can

be mistakenly identified as muons. Each of the five layers has a total of six panels of Iarocci tubes oriented horizontally and vertically to constrain the hit position as a charged particle traverses the MuID. Similar to the track reconstruction described above for the MuTr, adjacent MuID hits in the Iarocci tubes are combined into clusters. Since the MuID lies outside of the magnetic field, MuID clusters are combined with a straight line to form MuID tracks.

Together, the MuTr and MuID form the muon spectrometers and cover a pseudorapidity range of $1.2 < |\eta| < 2.2$ with full azimuthal coverage, $\Delta\varphi = 2\pi$, as shown in Fig. 2.6. A muon candidate is identified by reconstructed tracks in the MuTr matched to MuID tracks. In this analysis, at least one of the tracks from a pair of muon candidates within the same event was required to penetrate through to the last MuID plane. This was done to further increase the signal-to-background ratio. The minimum momentum needed for a muon to reach the last MuID plane is $p_\mu \sim 3$ GeV/c.

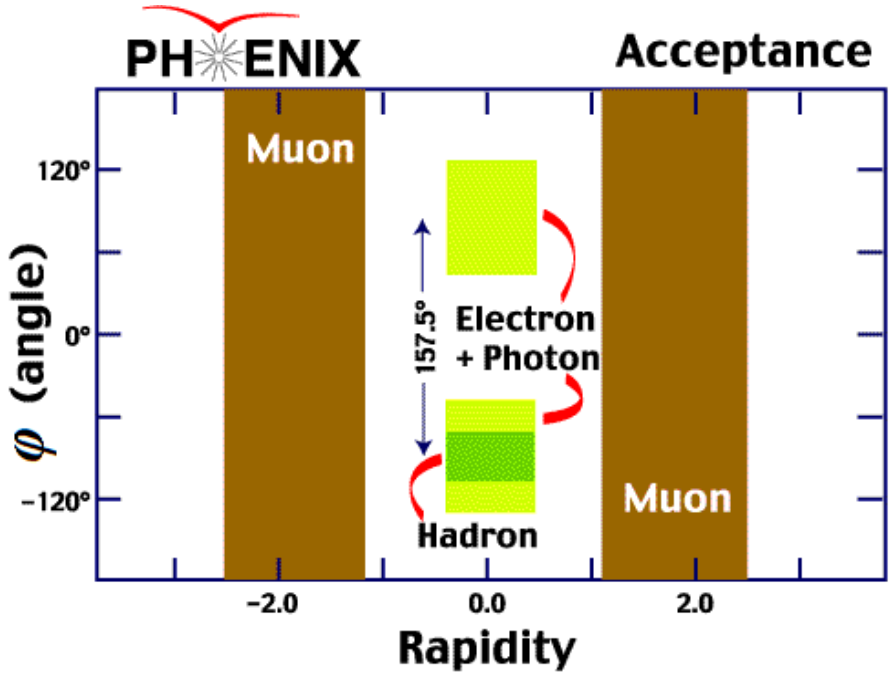

Figure 2.6. The acceptance of the PHENIX muon and central arms in φ vs. y.

2.2.1.2 Beam-Beam Counters (BBCs)

The two BBCs are global detectors used for event characterization in PHENIX. They are positioned on either side of the collision region and cover a pseudorapidity range of $3.1 < |\eta| < 3.9$ with full azimuthal coverage. The BBCs are able to determine the collision vertex, time of collision, and centrality, as well as to trigger minimum bias (MB) events. The MB trigger used in this analysis requires two or more counters firing on each side as well as a *z*-vertex selection of ± 10 cm. It fired on $93\% \pm 3\%$ of the 5.23 ± 0.15 barns total inelastic Cu+Au cross-section. The *z*-vertex is measured by the BBCs with a resolution of $\sigma_z \approx 0.5$ cm for the most central collisions and $\sigma_z \approx 2.0$ cm for the most peripheral collisions. It is important to note there that the *z*-vertex as measured by the BBCs is only used for the trigger, and the better vertex provided by the VTX+FVTX detectors as described in Sec. 2.2.1.4 below is used in the mass calculation. The events are sorted into centrality classes using the combined charge from both BBCs as described in Eq. 2.1 below

$$C = \varepsilon_{BBC}(1 - frac(Q_{BBC})) \,, \tag{2.1}$$

where *C* is the centrality expressed as a percentage, $\varepsilon_{BBC} = 93\%$ is the BBC efficiency described above, and $frac(Q_{BBC})$ is the fraction of the total BBC charge distribution integrated from zero to Q_{BBC}. The centrality is then compared to a Glauber model Monte Carlo simulation, as described in Sec. 1.2.2, to assign N_{part} and N_{coll} for each centrality bin.

2.2.1.3 Silicon Vertex Detectors (VTX+FVTX)

The VTX and FVTX detectors were installed in PHENIX in 2011 and 2012, respectively, to provide precise particle tracking and vertexing in the central (VTX) and forward and backward (FVTX) rapidities. The VTX, shown in the middle of Fig. 2.7, surrounds the collision point in PHENIX and consists of four layers of silicon sensors: two inner layers composed of 30 pixel ladders and two outer layers composed of 44 strip-pixel ladders arranged in a concentric pattern. The inner pixel detector layers are well-suited for the high multiplicity environment seen in heavy-ion collisions, while the two outer strip-pixel detector layers are used to minimize the number of readout channels. The VTX has full azimuthal coverage with pseudorapidity coverage of $|\eta| \leq 1.2$.

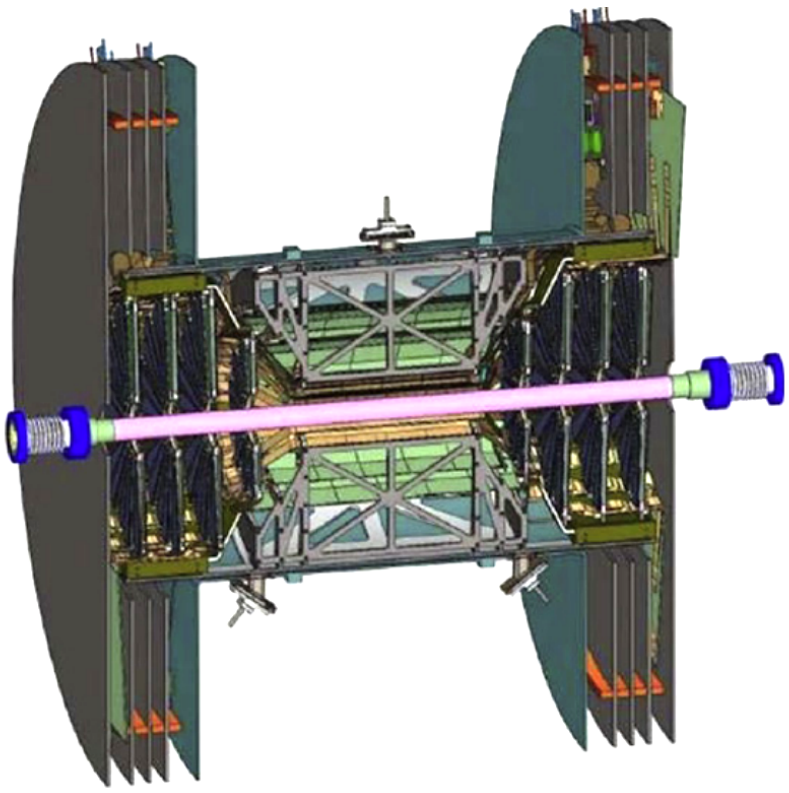

Figure 2.7. The view of the PHENIX silicon vertex detectors on the $z\varphi$-plane.

The FVTX covers approximately the same rapidity range as the existing forward and backward muon arms in PHENIX. It is comprised of two endcaps, one in the north arm and one in the south arm, each with four stations that sit perpendicular to the beamline as shown in Fig. 2.7. The stations are composed of silicon mini-strip sensors with a 75-μm pitch in the radial direction and lengths in the φ-direction varying from 3.4 mm to 11.5 mm. A total of approximately 1.08 million strips make up the FVTX detector.

A cross-section of the combined VTX+FVTX is shown in Fig. 2.8, with the VTX in the center and the FVTX endcaps on each end. The total length of this combined detector system is 80 cm. Prior to the installation of both silicon vertex detectors, the z-vertex was determined by the BBCs as described in the previous section and there was no determination of the x- or y-vertex. Since the installation of the silicon detectors, the collision point is now determined in PHENIX in x, y, and z. The combined FVTX+VTX vertex has a resolution that varies depending on both multiplicity and number of tracks but is better than 100 microns for the 2012 Cu+Au dataset. It is speculated that this better vertex resolution, and thus more precise mass calculation, may have contributed to the pioneering first measurement of ϕ meson production in heavy-ion collisions at forward and backward rapidity at RHIC that is presented in this paper. However, this has not been verified.

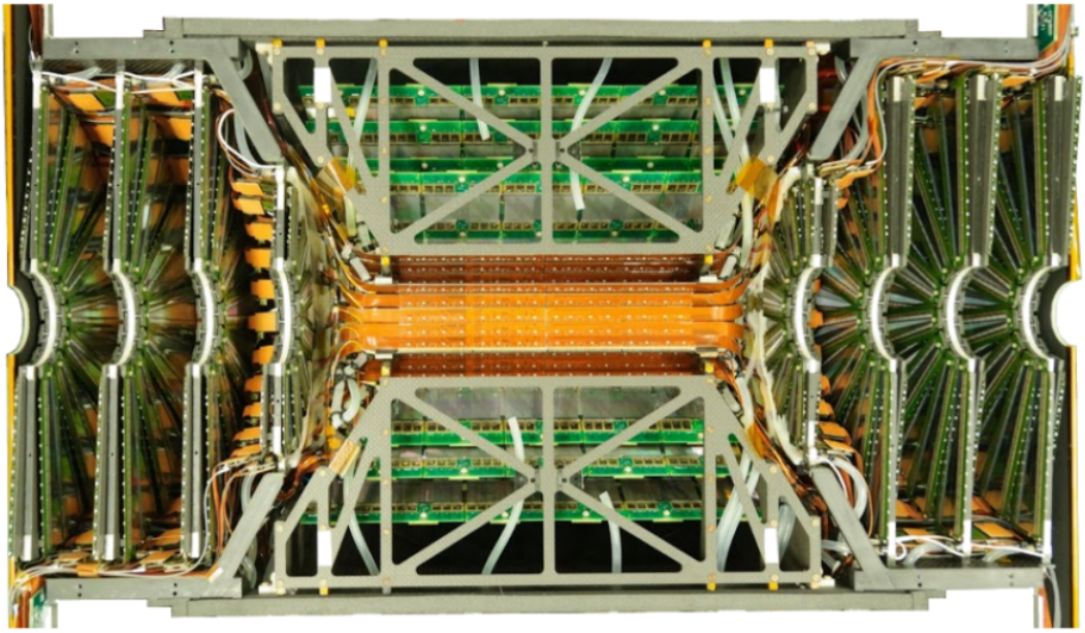

Figure 2.8. A photo of one-half of the combined VTX+FVTX detector system.

3 DATA ANALYSIS

3.1 Dataset

In this analysis, ϕ mesons are reconstructed from their decay muons in the RHIC Cu+Au dataset, which was taken over a 5.4-week period during the summer of 2012. After quality-assurance testing on each of the data segments, a total of 4.73 billion sampled MB events were used within a ±10 cm z-vertex selection and a centrality varying between 0% and 93%. This corresponds to an integrated luminosity of $\mathcal{L} = 0.97\ \text{nb}^{-1}$. A Glauber simulation, similar to what was described in Sec. 1.2.2, was used to estimate the total inelastic cross-section for Cu+Au collisions at 200 GeV to be 5.23 ± 0.15 b.

It is important to note here that the nuclear-modification factor defined in Eq. 1.14 uses ϕ meson yields from both heavy-ion (in this case, Cu+Au) collisions and a p+p baseline at the same center-of-mass energy. The p+p collision data was taken in 2009 and the measurement is described in detail in Ref. [19]. The y and p_T binning in the p+p analysis differs from what is presented here in the Cu+Au analysis; therefore, the p+p invariant yields were re-measured using the same methods described in Ref. [19] with the same binning as the Cu+Au analysis. The sampled luminosity of the p+p data corresponds to $\mathcal{L} = 14.1\ \text{pb}^{-1}$.

3.2 Quality Cuts

In order to optimize the signal-to-background ratio, a set of quality cuts is applied to the data to select good muon candidates from which ϕ mesons are reconstructed. An extensive study on these cuts is done in both simulation and data. Given that the backward rapidity arm (Au-

going direction) has a higher multiplicity than the forward rapidity arm (Cu-going direction), the backward rapidity arm also has more combinatorial background as discussed in the next section. Therefore, the backward rapidity arm requires tighter cuts than the forward rapidity arm. The finalized cuts are summarized in Table 3.1 below, followed by a detailed description of how each of these cuts is determined.

Table 3.1. Quality cuts for ϕ meson signal extraction in Cu+Au collisions at 200 GeV in PHENIX.

Variable	Au-going Cut	Cu-going Cut	Meaning
$\|BBC_Z\|$ (cm)	< 10	< 10	Collision vertex along the beam direction as measured by the BBCs
pDGO (GeV/c · cm)	< 90	< 50	Track momentum times the spatial difference between the MuTr track and MuID track at the first MuID layer
pDDG0 (GeV/c · radian)	< 30	< 45	Track momentum times the slope difference between the MuTr track and MuID track at the first MuID layer
χ^2_{tr}	< 5	< 10	χ^2/NDF of the muon track

lastgap	One track ≥ 2, other track ≥ 4	One track ≥ 2, other track ≥ 4	Last MuID plane penetrated by the muon track
nidhits	>(2·lastgap-1)	>(2·lastgap-1)	Number of hits in the MuID, out of the maximum 10
ntrhits	> 11	> 10	Number of hits in the MuTr, out of the maximum 16
$\boldsymbol{\chi^2_{vtx}}$	< 4	< 7	χ^2/NDF of the dimuon track with the vertex
Dimuon p_T (GeV/c)	1 – 5	1 – 5	Transverse momentum of the dimuon pair
$\lvert p_z \rvert$ (GeV/c)	> 2.4	> 2.5	Momentum of the muon along the beam axis

The collision *z*-vertex as measured by the BBCs is required to be within ±10 cm along the beam axis from the center of the collision region. The MuTr tracks and MuID tracks are matched at the first MuID layer in both position and angle. This matching is described with the variables *DG0* and *DDG0* as shown in Fig. 3.1.

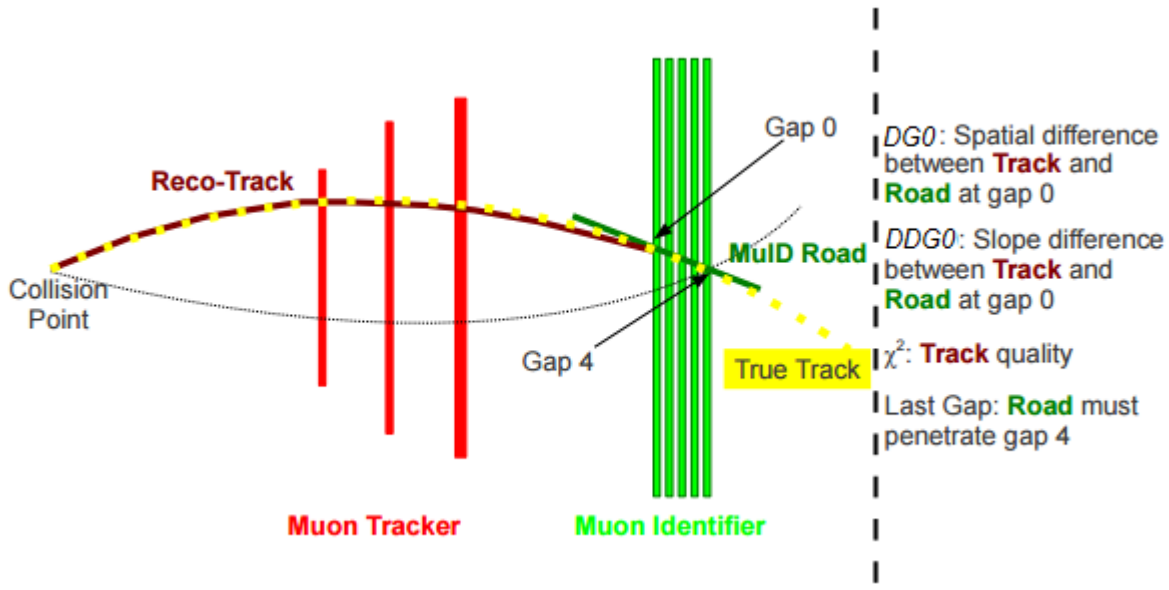

Figure 3.1. Schematic of the *DG0*, *DDG0*, and χ^2_{tr} in the PHENIX muon arms

As seen in Fig. 3.1, *DG0* is the spatial difference between the MuTr track and MuID track, while *DDG0* is the slope difference between the two. For this analysis, it is apparent that the momentum-independent *DG0* and *DDG0* cuts throw out a portion of the ϕ meson signal and are thus inefficient. Accordingly, the momentum-dependent variables *pDG0* and *pDDG0* are introduced and used instead. Fig. 3.2 shows the distributions for *DG0* vs. *p* (a and b) and *DDG0* vs. *p* (c and d) for the backward arm (a and c) and forward arm (b and d) in simulated ϕ meson events. Details on the simulation are described in detail in Sec. 3.5. In Fig. 3.2, the simulated distribution is shown in black, the portion that survives the momentum-independent cut is represented by anything that falls below the blue line, and the portion that survives the momentum-dependent cut is shown in red. It is evident that the momentum-dependent cut keeps more signal and is thus a more sophisticated quality cut.

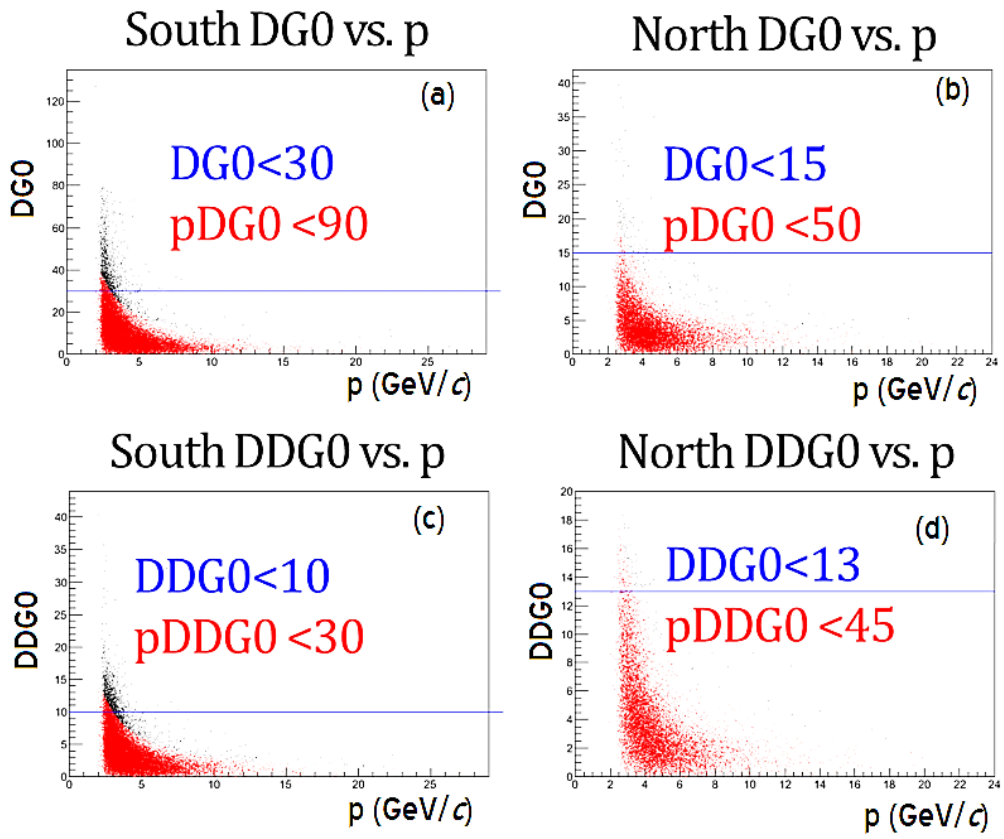

Figure 3.2. The momentum-dependent and momentum-independent cuts for *DG0* and *DDG0*.

To decrease the number of punch-through hadrons that can be misidentified as muons, the dimuon pair is required to have one track reach through to the last MuID gap, while the other track needs to make it to at least gap 2. Additionally, the track must have greater than a minimum number of possible hits in the MuTr and MuID. Furthermore, a maximum allowed χ^2/NDF is applied to both the vertex and track determination.

In the following figures, the distributions of variables that are cut on are plotted in blue for the ϕ meson signal, which comes from simulation, and in red for the background, which comes from real data as described in the following section. In most cases, the cuts keep 95% of

the ϕ meson signal in the backward arm and 99% of the ϕ meson signal in the forward arm in the simulation, as indicated on each figure. The single muon momentum along the beam axis, p_z, is reconstructed and energy-loss corrected at the collision vertex. There is a minimum value required for p_z. Finally, this analysis has a limitation in transverse momentum due to the large background and small acceptance at low dimuon p_T and small statistics at high dimuon p_T. Accordingly, the measurement is restricted to the dimuon transverse momentum range $1 < p_T < 5\ \mathrm{GeV}/c$.

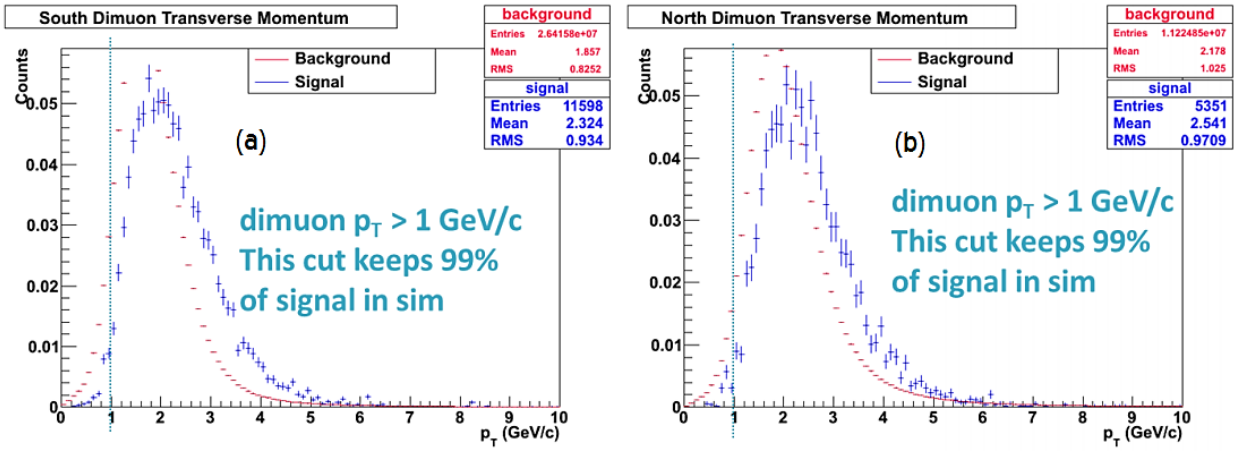

Figure 3.3. Dimuon transverse momentum and quality cut for the backward arm (a) and forward arm (b). The distributions are plotted in blue for the ϕ meson signal, which comes from simulation, and in red for the background, which comes from real data.

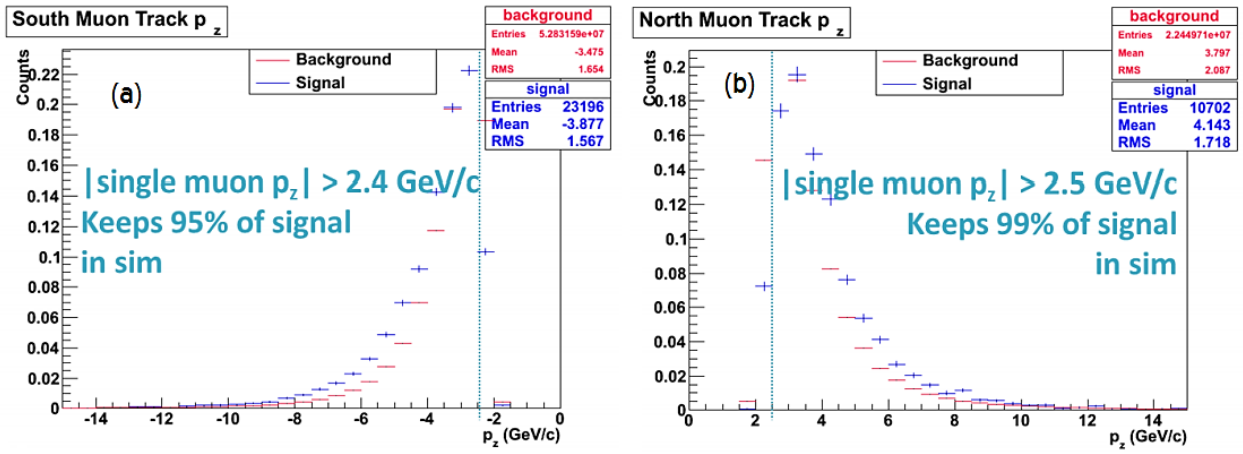

Figure 3.4. Single muon momentum along the *z*-axis for the backward arm (a) and forward arm (b) as well as the associated quality cut. The distributions are plotted in blue for the ϕ meson signal, which comes from simulation, and in red for the background, which comes from real data.

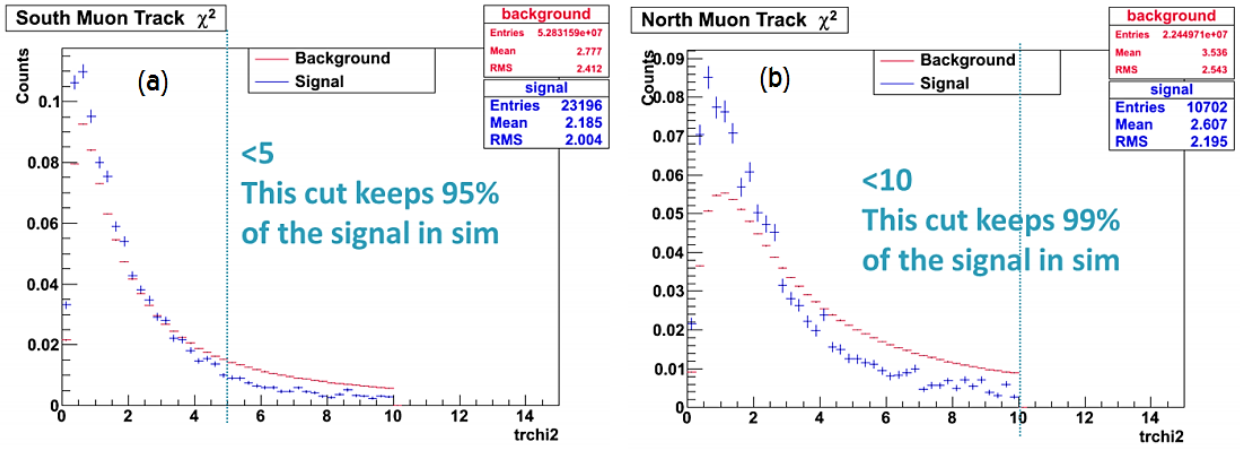

Figure 3.5. Track χ^2distributions for the backward arm (a) and forward arm (b) and the associated quality cut. The distributions are plotted in blue for the ϕ meson signal, which comes from simulation, and in red for the background, which comes from real data.

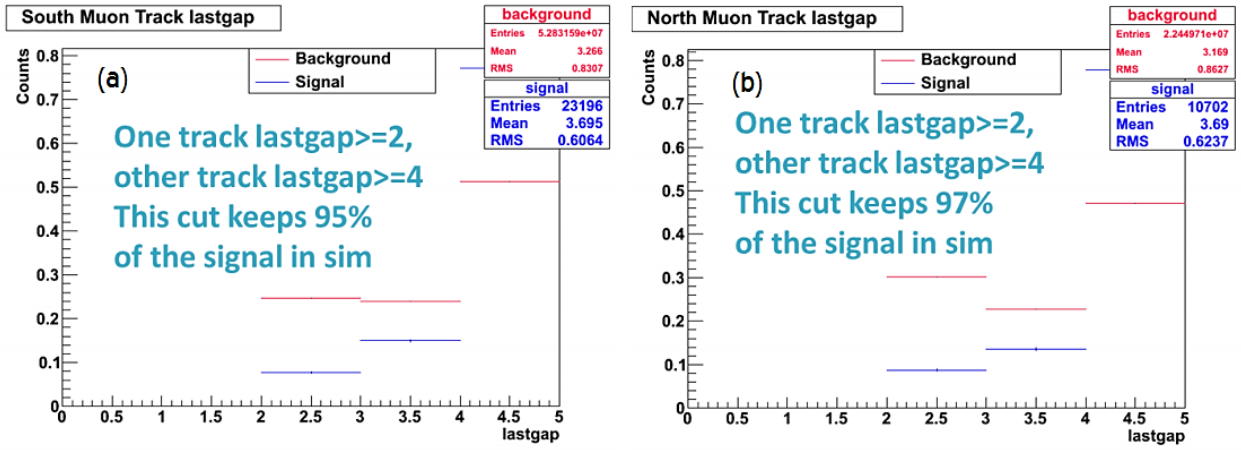

Figure 3.6. Single muon lastgap distribution for the backward arm (a) and forward arm (b) along with the associated quality cut. The distributions are plotted in blue for the ϕ meson signal, which comes from simulation, and in red for the background, which comes from real data.

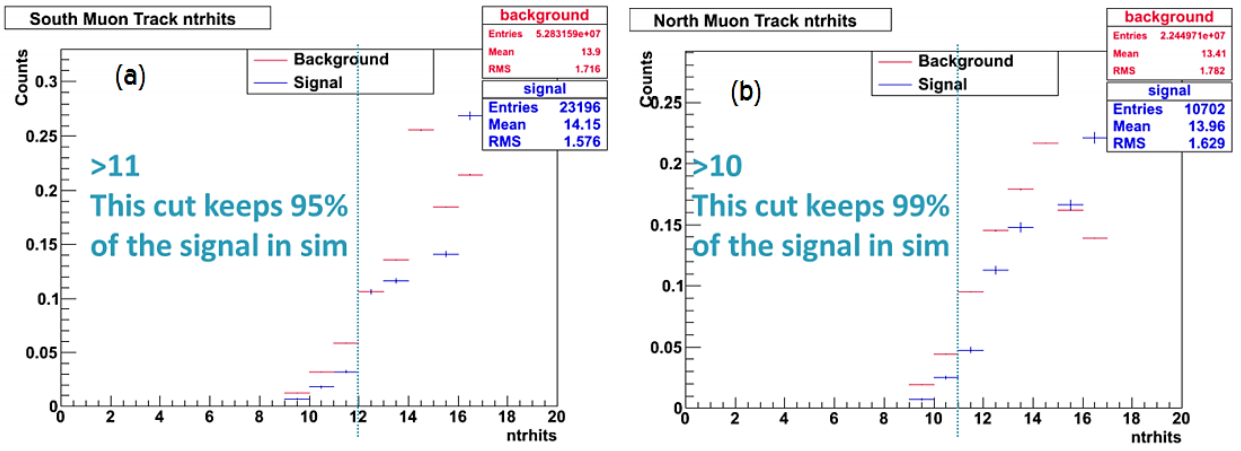

Figure 3.7. Single muon ntrhits distribution for the backward arm (a) and forward arm (b) and the associated quality cut. The distributions are plotted in blue for the ϕ meson signal, which comes from simulation, and in red for the background, which comes from real data.

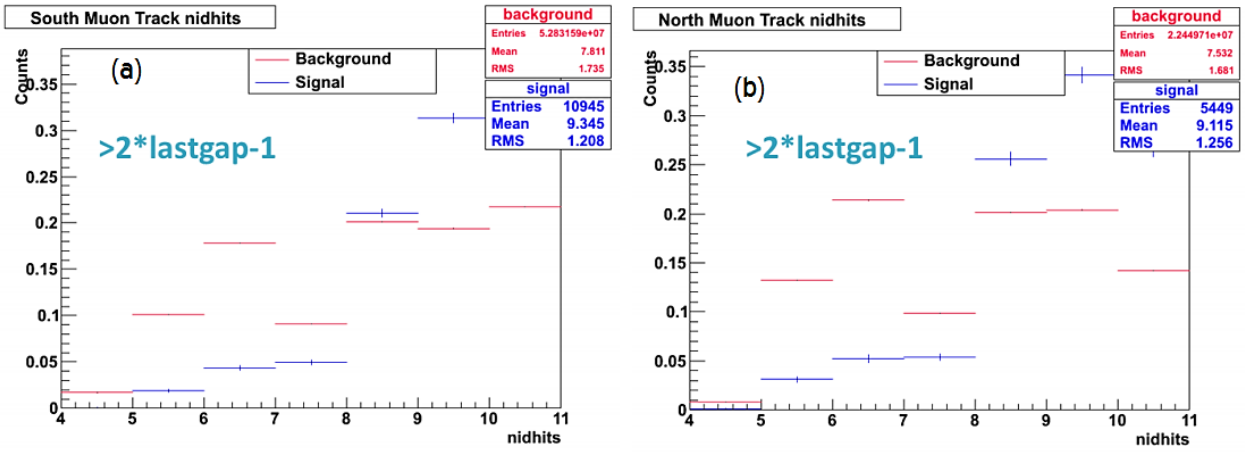

Figure 3.8. Single muon nidhits distribution for the backward arm (a) and forward arm (b) and the associated quality cut. The distributions are plotted in blue for the ϕ meson signal, which comes from simulation, and in red for the background, which comes from real data.

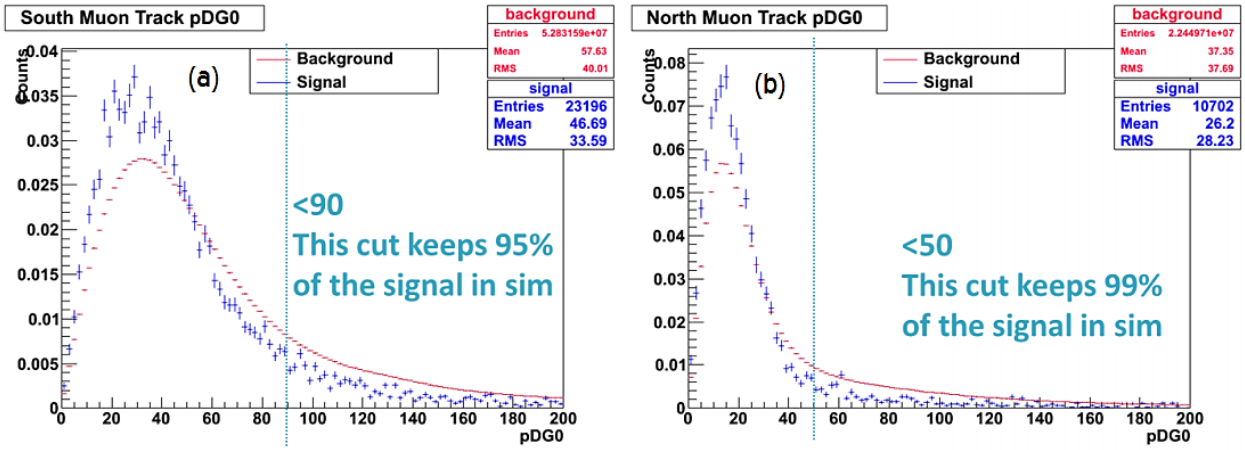

Figure 3.9. Single muon *pDG0* distribution for the backward arm (a) and forward arm (b) and the associated quality cut. The distributions are plotted in blue for the ϕ meson signal, which comes from simulation, and in red for the background, which comes from real data.

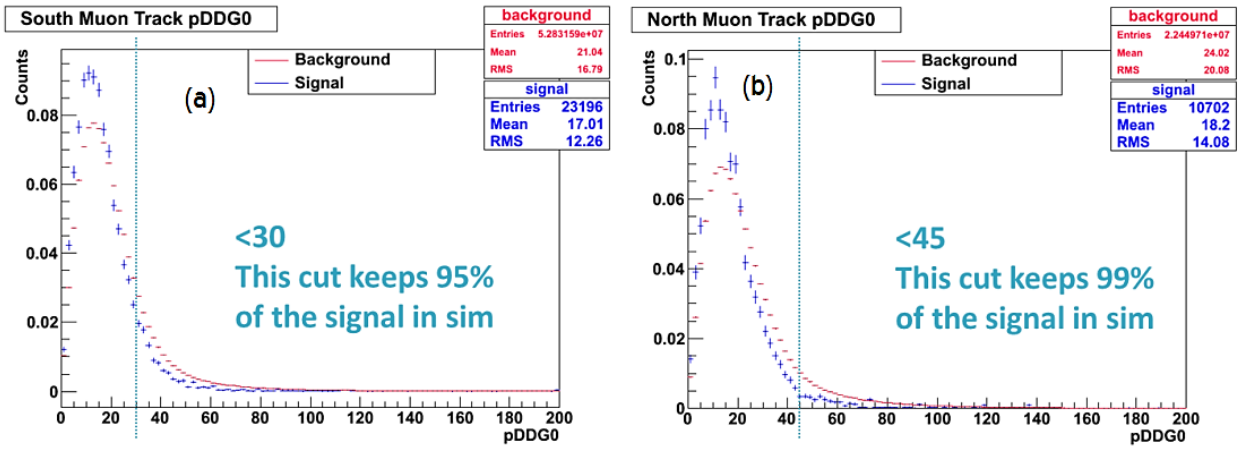

Figure 3.10. Single muon *pDDG0* distribution for the backward arm (a) and forward arm (b) and the associated quality cut. The distributions are plotted in blue for the ϕ meson signal, which comes from simulation, and in red for the background, which comes from real data.

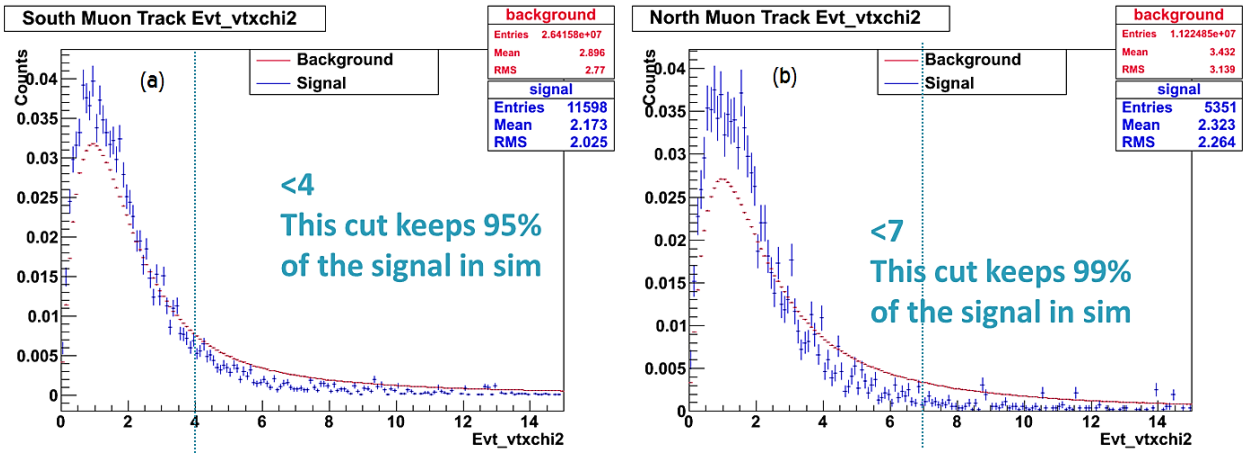

Figure 3.11. Vertex χ^2 distributions for the backward arm (a) and forward arm (b) and the associated quality cut. The distributions are plotted in blue for the ϕ meson signal, which comes from simulation, and in red for the background, which comes from real data.

3.3 Background Subtraction

There is an extremely low signal-to-background ratio in the ϕ meson mass region in the PHENIX muon arms, which have a small acceptance for ϕ mesons. In the most peripheral centrality bin, 40% – 93%, the signal-to-background is 28% in the Cu-going direction (1.2 <

$y < 2.2$) and 37% in the Au-going direction ($-2.2 < y < -1.2$). These values decrease dramatically in the most central centrality bin, $0\% - 20\%$, where the signal-to-background is only 6.7% in the Cu-going direction ($1.2 < y < 2.2$) and 9% in the Au-going direction ($-2.2 < y < -1.2$). Since the ϕ meson signal is located near a detector acceptance edge, it is important to have a clear understanding of the backgrounds. Additionally, this is the first time in both RHIC and PHENIX that the ϕ meson signal has been extracted in heavy-ion collisions at forward and backward rapidities. Accordingly, the backgrounds were studied in detail and multiple background subtraction methods were explored and compared.

The first step for any of these methods is to form the invariant mass distribution. The invariant mass is defined in Eq. 1.8. In this case, it is formed by combining two muon candidates of opposite charge, called an unlike-sign pair. The unlike-sign invariant mass spectrum contains the resonances, in this case the ϕ, ρ, ω, and J/ψ mesons, as well as both correlated and uncorrelated backgrounds. The correlated backgrounds come from the Drell-Yan process, open beauty decays, open charm decays, and ω meson and η meson Dalitz decays. These backgrounds will be discussed in Sec. 3.4. The uncorrelated backgrounds arise from random combinatorial associations of muon candidates, which are thus called combinatorial background. The remainder of this section discusses the three different methods that were explored for subtracting backgrounds in this analysis: the χ^2_{vtx} method, the like-sign method, and finally, the event mixing method, which was the method applied for the final result.

3.3.1 The χ^2_{vtx} Method

In previous PHENIX analyses, the ϕ meson was measured at forward and backward rapidities in *d*+Au and *p*+*p* collisions using a data-driven technique named the χ^2_{vtx} method [18,

19]. This method depends on the fact that the backgrounds in *p*+*p* and *d*+Au collisions are dominated by at least one pion or kaon decaying to muons. Therefore, it is possible to estimate the backgrounds by looking at events with large χ^2_{vtx}. This method was successful for ϕ meson signal extraction in the low multiplicity events produced in *d*+Au and *p*+*p* collisions. However, in heavy-ion collisions, such as Cu+Au, this method is not effective, especially for more central collisions. This is because the combinatorial background goes as the number of tracks squared, so while the *p*+*p* and *d*+Au backgrounds were dominated by correlated muons from hadronic decays, the Cu+Au backgrounds in this analysis are dominated by random combinatorial associations. Both the like-sign method and the event mixing method are able to estimate combinatorial background. The results of using these two methods to extract the ϕ meson signal in Cu+Au collisions at forward and backward rapidities at 200 GeV in PHENIX are discussed in more detail later in this chapter.

3.3.2 The Like-Sign Method

In the like-sign background subtraction technique, it is assumed that the like-sign dimuon pairs come purely from combinatorial background. It follows that the like-sign distribution is subtracted from the unlike-sign distribution to extract the signal as described in Eq. 3.1 below,

$$N_{+-} = FG_{+-} - FG_{\pm\pm} \,. \tag{3.1}$$

In the above equation, N_{+-} is the uncorrelated background-subtracted signal and FG stands for the foreground dimuon pairs, corresponding to pairs formed within the same event. FG_{+-} is unlike-sign foreground pairs, and $FG_{\pm\pm}$ is the like-sign foreground pairs, either plus-plus or

minus-minus. Prior to subtracting the uncorrelated background via this technique, the like-sign distribution $FG_{\pm\pm}$ is normalized to the unlike-sign distribution. This background normalization is very straight-forward and described in Eq. 3.2 [39]

$$FG_{\pm\pm} = (FG_{++} + FG_{--}) \frac{2\sqrt{\int FG_{++}\mathrm{d}m \int FG_{--}\mathrm{d}m}}{\int (FG_{++}+FG_{--})\mathrm{d}m}, \tag{3.2}$$

where m is the dimuon invariant mass, FG_{++} and FG_{--} are the plus-plus and minus-minus like-sign foreground dimuon pairs, respectively, and the integration is carried out in the range $0.2 < m < 5.0$ GeV/c^2.

It is important to note here that not all like-sign pairs are combinatorics. This is because combinatorial background is made up of uncorrelated pairs, but decay products of Dalitz, charm, and beauty contain like-sign pairs that are correlated. A study of the correlated background is found in Sec. 3.4.

It is also important to note that the like-sign method is not used to make the measurement presented in this paper due the statistical limitations of the like-sign technique. The like-sign method provides a way to cross-check results from the event mixing method, which is described in the next subsection. After subtracting the combinatorial background and fitting the resonances as well as the remaining correlated background, the results from like-sign background subtraction are consistent with those from mixed-event background subtraction within statistical uncertainties, which helps to confirm the validity of the results. Any differences between the like-sign and event mixing methods are included as a systematic error, which is detailed at the end of this chapter in Sec. 3.7.

3.3.3 The Event Mixing Method

In parallel to applying the like-sign technique, the uncorrelated background is also estimated via the event mixing method. A pool of four events is stored at a time, and each pool contains events within a 2%-centrality and 1-cm z-vertex bin to ensure that particle multiplicity and position are roughly the same between mixed events in order to minimize the resultant systematic uncertainty. In this method, a muon from one event will become randomly associated with a muon from a different event with identical centrality and vertex bins, producing an uncorrelated dimuon pair. These two-track random combinations are then used to describe the combinatorial background, with the mixed-event background distributions generated at about eight times higher statistics than the actual background. Hence, it is necessary to introduce a normalization factor to scale the mixed-event background, BG, to the same-event foreground, FG. This normalization factor also accounts for slightly different multiplicities from mixing different events within the centrality bins described above.

Although a mass-dependent normalization technique was developed for this analysis, the standard event mixing technique will be described first. In the standard event mixing method, which was applied in many previous high-energy physics analyses, the normalization factor α is calculated as described in Eq. 3.3

$$\alpha = \sqrt{\frac{\int FG_{++}\mathrm{d}m \int FG_{--}\mathrm{d}m}{\int BG_{++}\mathrm{d}m \int BG_{--}\mathrm{d}m}}, \tag{3.3}$$

where FG_{++} and FG_{--} are the like-sign same-event foreground pairs and BG_{++} and BG_{--} are the like-sign mixed-event background pairs. In Eq. 3.3, each term in the square-root is integrated over the mass range, introducing a mass-independent normalization factor [40, 41].

Since this was the first time mixed-event dimuons were used in PHENIX to describe the backgrounds in the low-mass region, event mixing in the ϕ meson mass region was thoroughly studied. As a test, the standard PHENIX event mixing software was temporarily modified so that only single muons that make a dimuon pair in a specific low-mass bin were kept, then they were mixed as usual and the resultant like-sign mixed-event background was studied. In addition to this test, several other tests were done. It was observed that same-event dimuons are less likely to be reconstructed close to each other than mixed-event dimuons. Therefore, mixed-event dimuons will be generated in larger numbers in the low-mass region, where the dimuon pair opening angle is smaller. The normalization factor described in Eq. 3.3 shows that α is simply a ratio of like-sign same-event dimuons to like-sign mixed-event dimuons, which means that α will have smaller values in the low-mass region, where there is an excess of mixed events compared to same events. Therefore, α is not constant over all mass.

Since it was found that the normalization factor depends on mass, particularly in the low-mass region, it became necessary to introduce a mass-dependent normalization factor as described in Eq. 3.4 rather than using the more common mass-integrated normalization described in Eq. 3.3,

$$\alpha(m) = \sqrt{\frac{FG_{++}(m)FG_{--}(m)}{BG_{++}(m)BG_{--}(m)}}. \tag{3.4}$$

The mass-dependent normalization is accomplished by fitting the normalization factor from Eq. 3.4 and then multiplying the fit, rather than the integrated value, to the unlike-sign mixed-event background to get the normalized background spectrum, BG_{+-}^{norm},

$$BG_{+-}^{norm} = \alpha \times BG_{+-} \, . \tag{3.5}$$

Multiple fitting functions were tested, including a polynomial, a constant minus exponential, and an error function. The error function, described in Eq. 3.6, was used in the final analysis, and the different tested fits were used to help calculate the systematics as described in Sec. 3.7 at the end of this chapter,

$$g(m) = p_0 \times \mathrm{Erf}(\tfrac{m-p_1}{p_2}) \, . \tag{3.6}$$

In Eq. 3.6, $g(m)$ is the error function and p_0, p_1, and p_2 are simply the three free parameters of the fit. Fig. 3.12 below shows a plot of the normalization factor vs. mass, including the error function fit from Eq. 3.6, for forward rapidity (a) and backward rapidity (b).

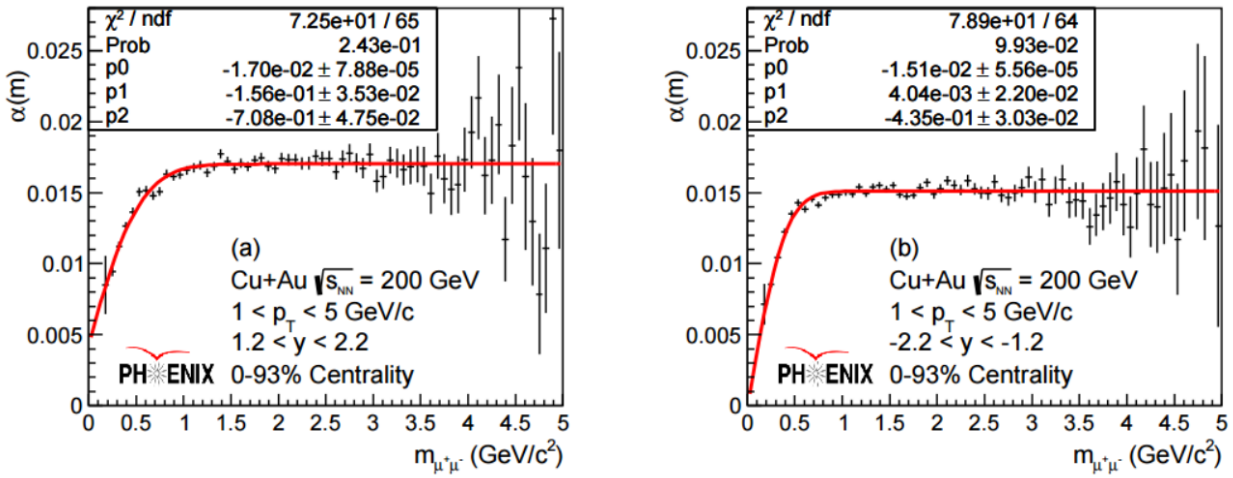

Figure 3.12. The normalization factor as a function of mass. The mass dependence of α is clearly visible in the low-mass region where the ϕ meson lies. The data is shown in black and the fit function is shown in red.

The event mixing technique was chosen for this analysis due to the statistical limitations of the like-sign technique. The application of this technique to describe the backgrounds in the range $0 < m < 5.0$ GeV/c^2 is shown in Fig. 3.13 for both forward rapidity (a) and backward rapidity (b). The open squares are the mixed-event background distribution and the closed circles are the unlike-sign spectrum. The $\rho+\omega$, ϕ, and J/ψ peaks are all clearly visible in Fig. 3.13 prior to background subtraction. The signal extraction and description of the remaining correlated background are described in detail in the following section.

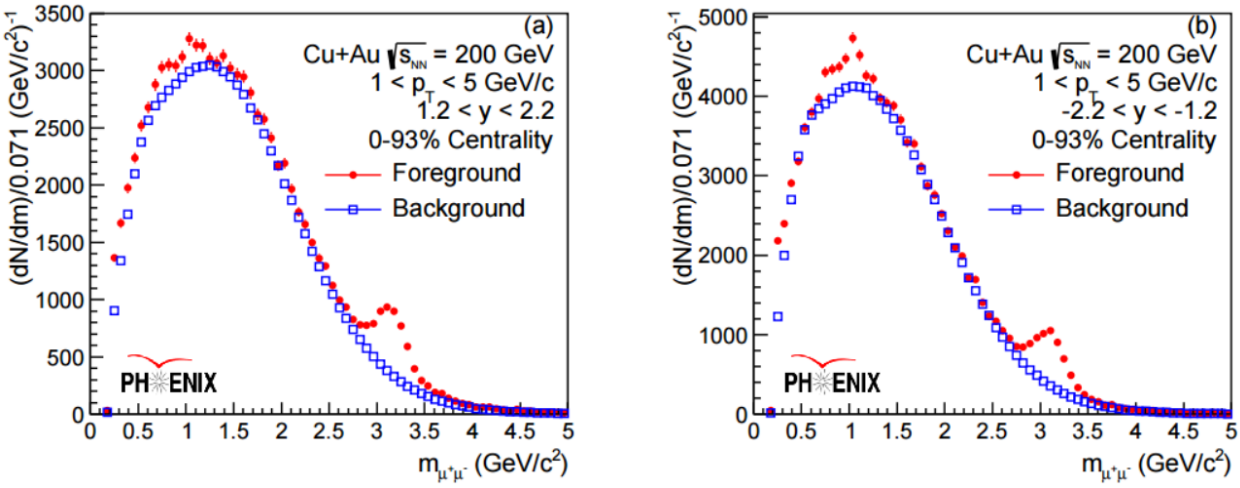

Figure 3.13. The mass distribution at forward rapidity (a) and backward rapidity (b) prior to background subtraction. The foreground is represented by red, closed circles, while the background is blue, open squares.

3.4 Signal Extraction and Correlated Background

Fig. 3.14 shows the mixed-event background-subtracted mass distribution at forward rapidity (a) and backward rapidity (b). The data is represented by black, closed circles, with the correlated background represented by a purple dashed-dotted line, the $\rho+\omega$ peak shown as a red

dotted line, the ϕ meson peak represented by a dashed green line, and the total fit shown as a solid blue line.

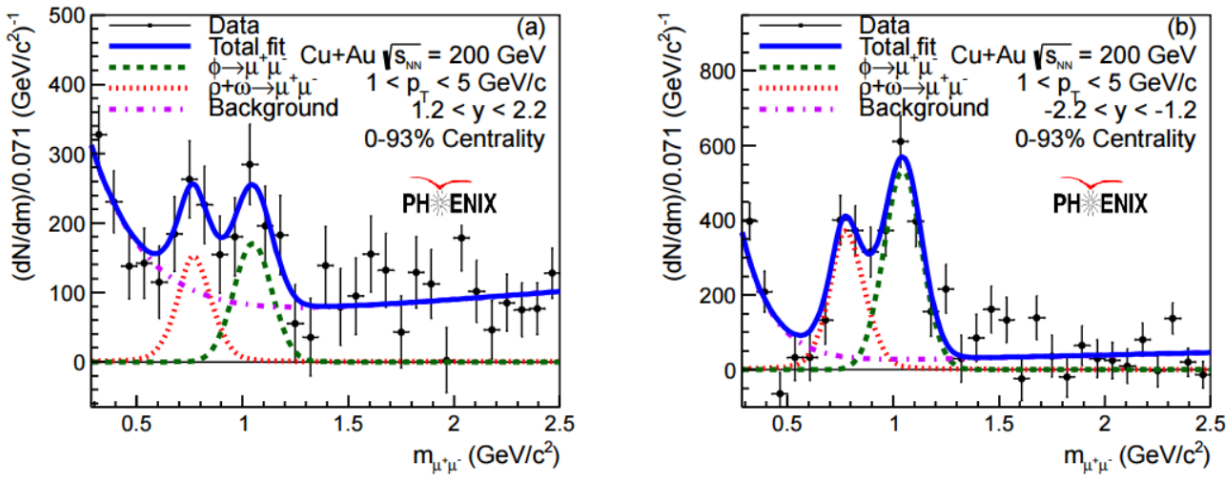

Figure 3.14. The dimuon mass spectra after mixed-event background subtraction for forward rapidity (a) and backward rapidity (b).

As described in the previous section, the event mixing and like-sign background subtraction techniques only account for the uncorrelated background that comes from random associations of muons. Accordingly, some correlated background remains. This background comes from real physics processes, but is considered background in this case. It was previously shown that heavy flavor, specifically charm and beauty, contributions were negligible in the ϕ meson mass region at PHENIX in d+Au and p+p collisions at 200 GeV [18, 19]. Accordingly, these contributions were initially ignored in studying the correlated background. A simulation study revealed that ω meson and η meson Dalitz decays may be one possible contributor to the correlated background, which is well-described by an exponential plus a first-order polynomial as described in Eq. 3.7

$$f(m) = e^{am} + b + cm, \tag{3.7}$$

where $f(m)$ is the fit function and a, b, and c are the free parameters of the fit. This fit function was successfully used to describe the correlated background in both simulation and real data. Several other fit functions and fit ranges were also tested and used to estimate one component of the systematic uncertainty as described in Sec. 3.7.

Although the ϕ meson is the only particle of interest in this analysis, the ρ and ω mesons overlap with the ϕ meson signal, requiring all three particles to be described. Because the PHENIX muon arms are unable to resolve the ρ and ω mesons separately, the total ρ+ω signal is fit and the yields are extracted based on the expected ratio between the two, which is a constant based on their branching ratios and cross-sections. This is similar to what was done in p+p and d+Au collisions [18,19]. The ϕ and ω signals are each well-described by a Gaussian distribution, while the ρ meson is fit with a Breit-Wigner distribution. Each of the fit parameters for the resonances are constrained but allowed to vary, except for the constant value for the ratio of the ρ to ρ+ω mesons.

3.5 Detector Acceptance and Efficiency

Because particle detectors do not have full geometrical acceptance or 100% efficiency, the raw yields extracted in the previous section must be corrected to account for the product of detector acceptance and reconstruction efficiency, $A\varepsilon_{\mathrm{rec}}$, of dimuon decays of ϕ mesons. In this way, the detector bias is removed so that physical quantities for ϕ meson production and nuclear modification can be reported. This is accomplished by the full-event reconstruction of a ϕ meson signal generated in PYTHIA 6.42 [42] and run through a full GEANT3 [43] simulation of the

PHENIX detector with the MB real-data background embedded in the simulation. In the following subsections, the simulation chain and $A\varepsilon_{rec}$ correction are detailed.

3.5.1 Event Generation (PYTHIA 6.42)

Event generators are commonly used to generate high-energy particle-physics events in simulation based on the expected physics processes, including production cross-sections and decay branching ratios, at a variety of energies. For this study, PYTHIA 6.42, which is described in Ref. [42], is used to generate p+p events at 200 GeV. It is important to note here that PYTHIA is only able to simulate p+p collisions and not heavy-ion collisions due to the complex collective behavior of such systems. However, these p+p simulations still prove extremely useful in studying heavy-ion collisions at the same center-of-mass energy. In this analysis, PYTHIA 6.42 is used to generate the ϕ meson signal, and the underlying heavy-ion event information is taken from real data as described in more detail in the next section.

PYTHIA 6.42 is a series of software libraries written in FORTRAN used to randomly generate high-energy particle-physics events. PYTHIA simulations provide insight into various physics processes in high-energy collisions, including initial- and final-state parton showers, parton distributions, hard and soft interactions, fragmentation, decays, and more. However, production of the ϕ meson in heavy-ion collisions is not well-understood at this time, so PYTHIA does have its limitations.

The low-mass vector mesons, ϕ, ρ, and ω, are generated based on the following meson parameters [7,42]:

Table 3.2. The low-mass vector-meson parameters used in PYTHIA 6.42. The ϕ and ρ mesons are generated using the default PYTHIA 6.42 values, while the ω meson is manually added to the simulation based on the PDG values.

Meson	Mass (GeV/c^2)	Width (GeV/c^2)	Reference
ϕ	1.01940	0.00443	PYTHIA 6.42
ρ	0.76850	0.15100	PYTHIA 6.42
ω	0.78265	0.00849	PDG

Each of these particles is generated separately in PYTHIA, with the vertex and centrality distributions based on that of 2012 Cu+Au real-data MB events. The PYTHIA configuration codes used to generate each of the particles are given in Appendix A. Triggers and particle selection modules are developed for each particle to decrease both computation time and size of the output. First, a trigger is written and applied such that only low-mass vector mesons decaying within the muon arm acceptance are saved. In order to avoid any possible detector edge effects, the rapidity range is slightly greater than the actual muon-arm acceptance and a muon-arm rapidity cut is applied later. The particle selection then selects only on low-mass vector mesons that have decayed to a dimuon pair. With these triggers and particle selections, only low-mass vector mesons that decay to a dimuon pair within the muon arm acceptance are included in the PYTHIA output. Fig. 3.15 below shows the mass distributions of the low-mass vector mesons and the J/ψ meson at the PYTHIA-level. The mass peaks are much sharper at this

stage than in real-data because the detector effects have not yet been accounted for, which leads to the next step in the simulation chain: a GEANT3 simulation of the PHENIX detector.

Before moving on, it is important to note that the J/ψ meson was included in the simulation and real-data analysis solely for the purpose of reproducing the measurement published in Ref. [41] in order to verify the validity of the methods presented in this paper. This was done completely independent of the ϕ meson analysis. In addition, the ρ and ω mesons were only included for informational purposes, and they did not affect the actual $A\varepsilon_{rec}$ calculation.

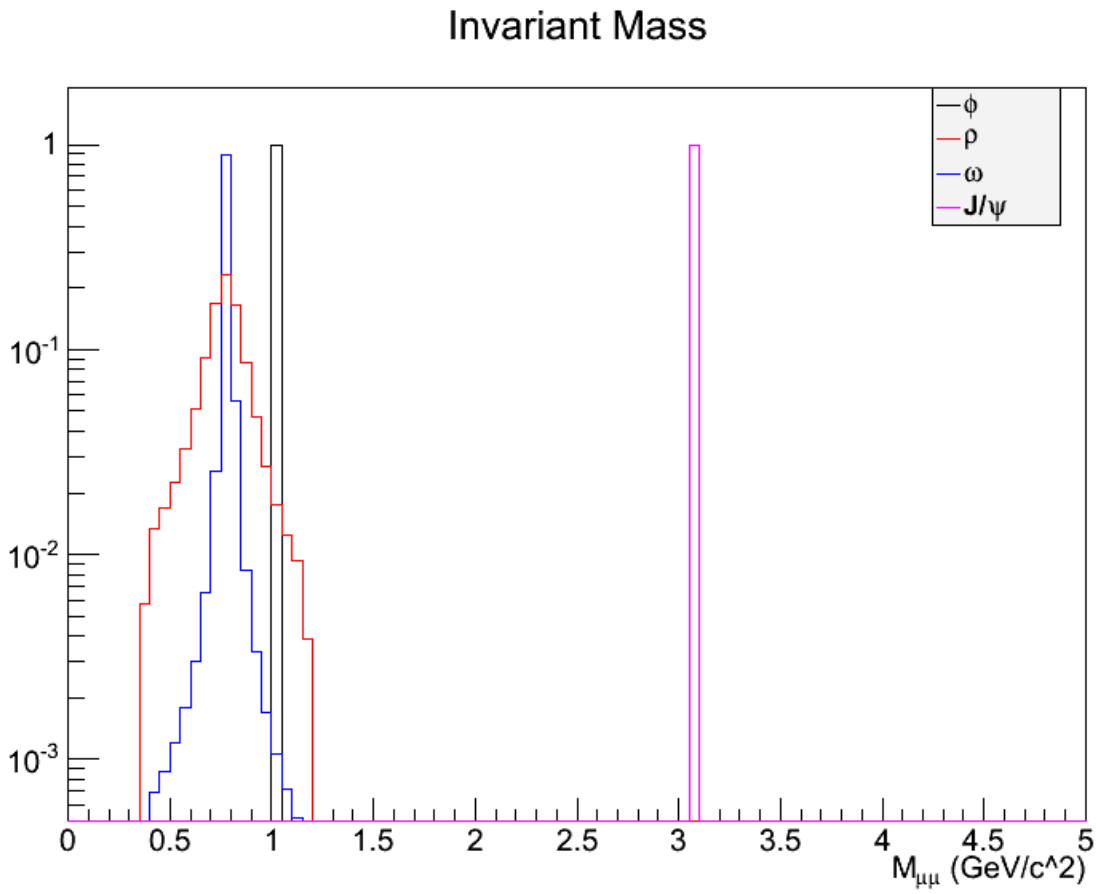

Figure 3.15. The mass distributions of the low-mass vector mesons, ϕ (black), ρ (red), and ω (blue), and the J/ψ meson (pink) at the PYTHIA-level.

3.5.2 GEANT3 Simulation

To be consistent with the real-data analysis, the generated PYTHIA events are run through a full GEANT3 simulation of the PHENIX detector and then reconstructed with the standard PHENIX software and analyzed with the dimuon analysis code developed for this measurement. In this way, the simulation is treated in the exact same manner as the real data, including the mixed-event background subtraction and signal extraction described earlier in this chapter. In this subsection, the GEANT3 framework is introduced and the PHENIX simulation chain is further detailed.

GEANT3, which is described in detail in Ref. [43], is simulation software written in FORTRAN to study the "GEometry ANd Tracking" of particles as they pass through matter. Using Monte Carlo methods, the GEANT3 software is capable of tracking the particles produced by PYTHIA and other event generators. The PHENIX Integrated Simulation Application (PISA) is a standard PHENIX detector setup in GEANT3 used throughout the collaboration. For this analysis, PISA was modified for the PHENIX 2012 detector setup, with the appropriate magnetic field polarity and necessary detectors installed and turned on. Fig. 3.16 shows an example event display in PISA for muons with a momentum of 3.5 GeV/*c* as they travel through the PHENIX detector in simulation.

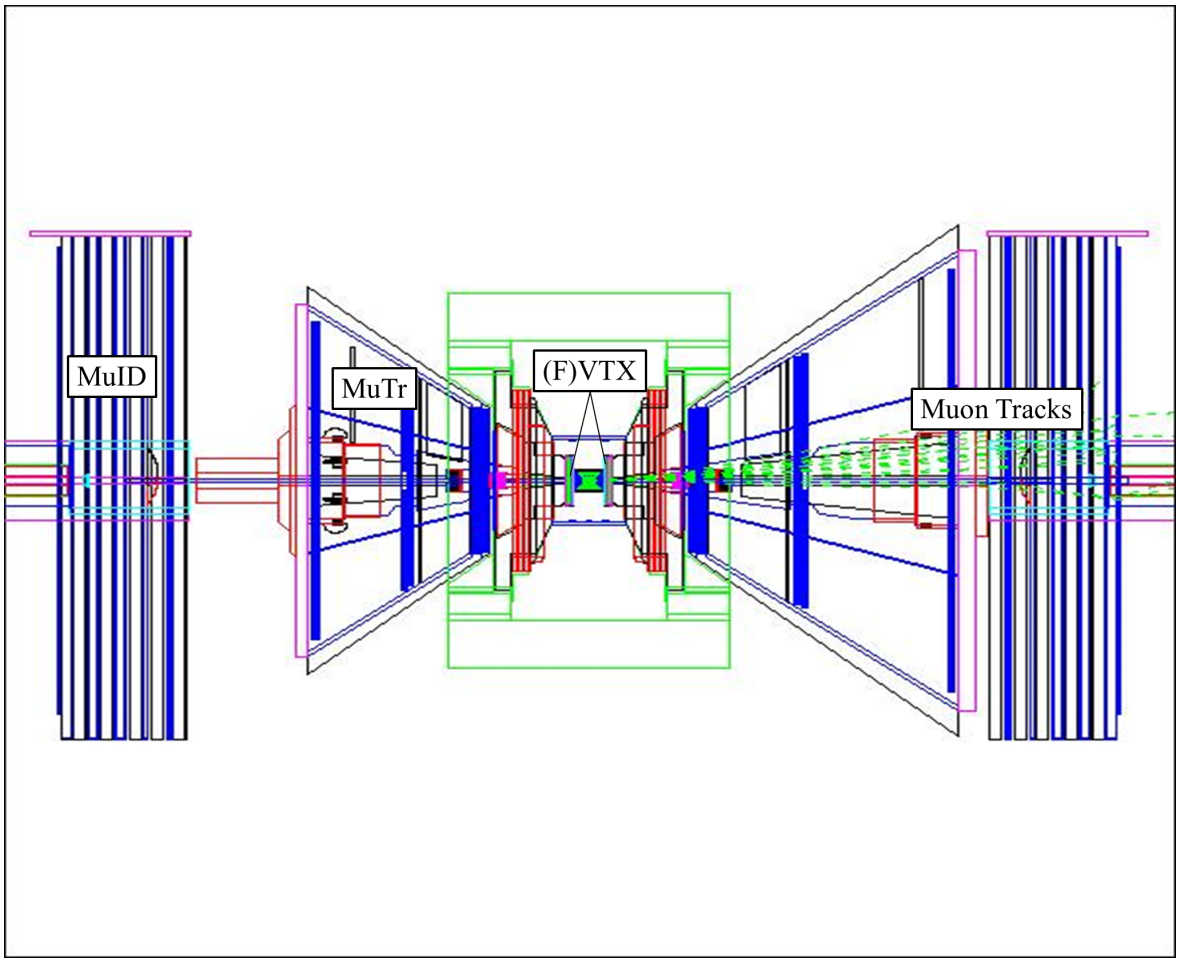

Figure 3.16. A PISA event display for muons of momentum 3.5 GeV/*c* as they traverse the PHENIX detector in simulation. Muons generated in PHENIX collisions need at least $p \sim 3$ GeV/*c* to make it to the back of the MuID.

After inputting the appropriate parameters and running the PYTHIA output through PISA, a ROOT-formatted PISA hits file is produced. This file is then run through the standard PHENIX reconstruction code followed by the analysis module developed specifically for this study, including the background subtraction and fitting techniques described earlier in this chapter. During reconstruction, MB real-data background is embedded into the simulation, making it more like real Cu+Au events in PHENIX. In addition, MuTr and MuID efficiency files are read into the simulation, allowing for simulated effects of both detector acceptance and reconstruction efficiency. At this point, the $A\varepsilon_{\mathrm{rec}}$ of dimuon decays of ϕ mesons in Cu+Au

collisions at 200 GeV in the PHENIX muon arms is evaluated as described in the following section.

3.5.3 Centrality-Weighted Acceptance and Efficiency

The detector acceptance and reconstruction efficiency is defined in Eq. 3.8

$$A\varepsilon_{\mathrm{rec}}(y, p_T) = \frac{N_\phi^{reco}(y,p_T)}{N_\phi^{gen}(y,p_T)}, \tag{3.8}$$

where N_ϕ^{reco} is the number of reconstructed ϕ mesons and N_ϕ^{gen} is the number of ϕ mesons generated in PYTHIA. This is calculated separately for each transverse momentum and rapidity bin. Because the sampled events from real data are MB-triggered with a $|BBC_Z| < 10$ cm cut (see Table 3.1), the same trigger and z-vertex cut was applied when producing the input ϕ mesons in PYTHIA. In both simulation and data, the ϕ mesons are reconstructed using the same codes for mixed-event background subtraction with the mass-dependent normalization technique and the same fit functions as described earlier in this chapter.

Eq. 3.8 describes a centrality-independent value for $A\varepsilon_{\mathrm{rec}}$ of dimuon decays of ϕ mesons. It was mentioned in Sec. 3.5.1 that the centrality distribution at which ϕ mesons are thrown in simulation comes from the real-data centrality distribution. However, this distribution is representative of MB events and does not give the true centrality of ϕ mesons produced in Cu+Au collisions in PHENIX. This effect can be seen in Fig. 3.17, which shows the ϕ meson centrality distribution in real data in red and in simulation, which comes from real-data MB events, in black.

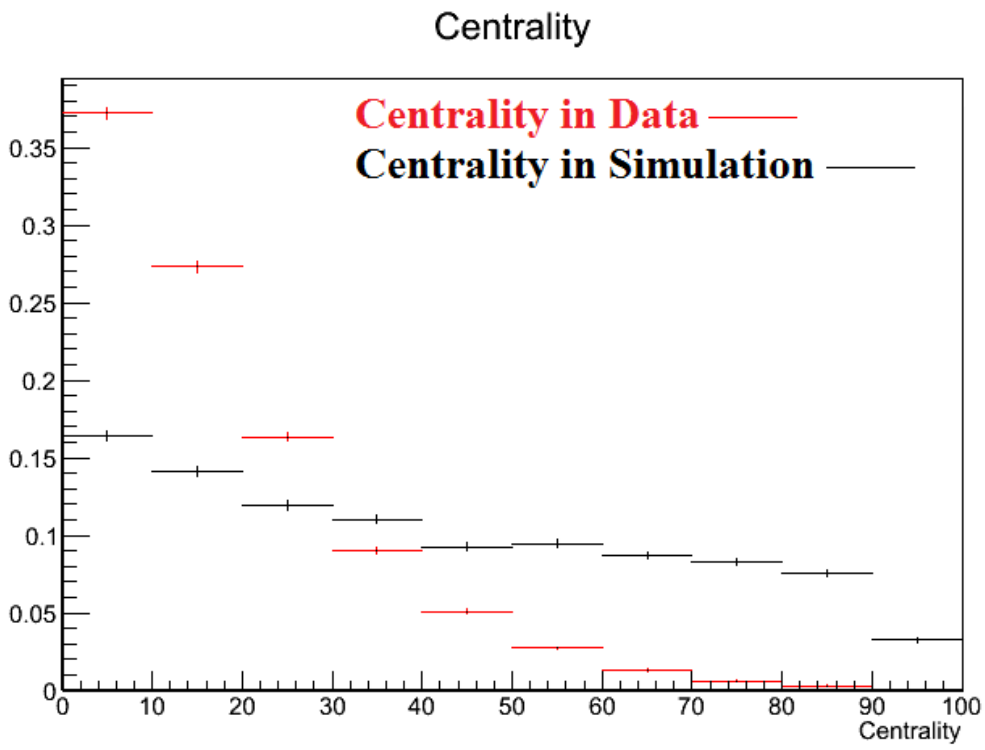

Figure 3.17. The centrality distributions of ϕ mesons in simulation (black) and in real data (red). This is for unlike-sign same-event dimuons in the resonance region with all cuts applied.

In Fig. 3.17, it is clear that the simulated centrality is not representative of the true centrality, so it becomes necessary to introduce a centrality-weighted $A\varepsilon_{\text{rec.}}$ The acceptance and efficiency is corrected for the centrality differences by calculating $A\varepsilon_{\text{rec}}$ in 10% centrality bins and then re-weighting based on the real-data distribution. This correction is described in Eq. 3.9 below,

$$A\varepsilon_{\text{rec}}(y, p_T, C) = \sum_{i=1}^{n}[(A\varepsilon_{\text{rec}}(y, p_T, C))_i \times N_{\phi,i}] \div \sum_{i=1}^{n} N_{\phi,i} \,. \tag{3.9}$$

In Eq. 3.9, C is centrality, n is the total number of centrality bins ($n = 10$ in this case), $(A\varepsilon_{\text{rec}}(y, p_T, C))_i$ is the acceptance and efficiency for centrality bin i, and $N_{\phi,i}$ is the number of ϕ mesons produced in real Cu+Au collisions in centrality bin i. The last term in Eq. 3.9 is solely

for normalization purposes. $N_{\phi,i}$ is calculated by reconstructing ϕ mesons in real data and correcting by the acceptance and efficiency as follows:

$$N_{\phi,i} = \frac{N_{\phi,i}^{reco}}{(A\varepsilon_{\mathrm{rec}}(y,p_T,C))_i}. \tag{3.10}$$

In Eq. 3.10, $N_{\phi,i}^{reco}$ comes from plotting the centrality distribution in real data in the ϕ meson resonance region with all quality cuts applied after background subtraction. Due to statistical limitations, the centrality distribution is fit with a polynomial and the fit function is used as seen in Fig. 3.18.

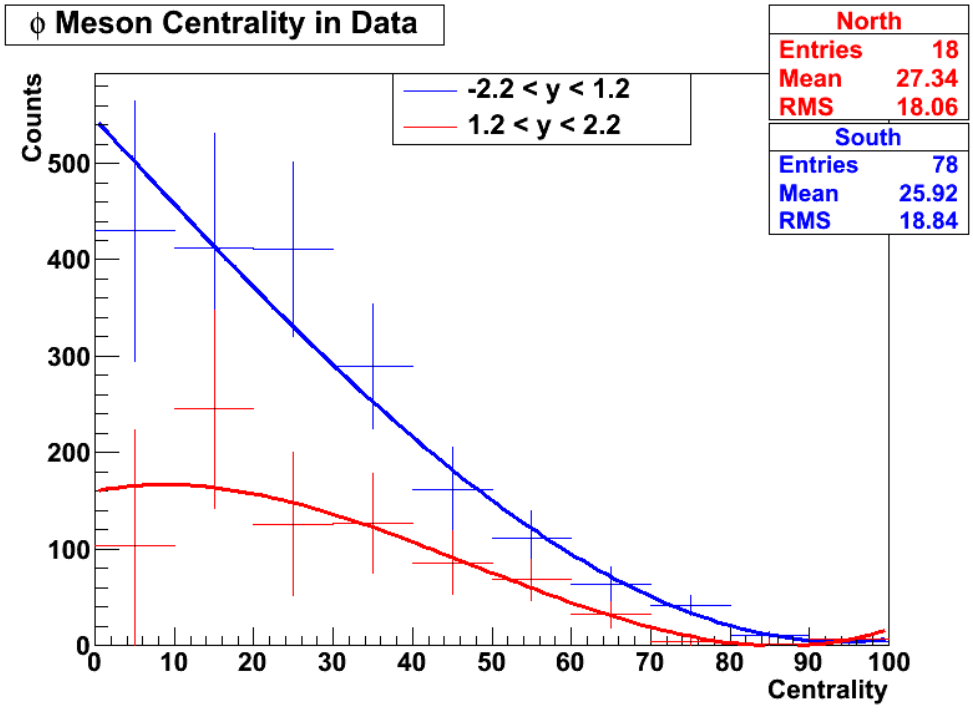

Figure 3.18. The centrality distribution for ϕ meson candidates in real data for the north (forward rapidity) arm in red and the south (backward rapidity) arm in blue. Due to limited statistics, these distributions are fit with a polynomial.

As a cross-check, the centrality-weighted acceptance and efficiency is also calculated from the actual values in Fig. 3.18 instead of the fit. The results were consistent within statistical uncertainties. Using this method, the centrality-weighted acceptance and efficiency is calculated for each kinematic bin. It is important to note that in analyses where the centrality bins are small enough, i.e. 10% centrality bin width, it is not necessary to use a centrality-weighted acceptance and efficiency calculation. However, this analysis uses three large centrality bins ($0\% - 20\%$, $20\% - 40\%$, and $40\% - 93\%$) and also includes centrality-integrated measurements, so it is necessary to implement the centrality weighting. The acceptance and efficiency values for each kinematic bin are summarized in Table 3.3. The rather strong p_T dependence is readily apparent, with the acceptance and efficiency going from $A\varepsilon_{rec} = 1.21 \times 10^{-3}$ in the Cu-going direction and $A\varepsilon_{rec} = 1.86 \times 10^{-3}$ in the Au-going direction at low p_T ($1 - 2.5$ GeV/c) to $A\varepsilon_{rec} = 1.69 \times 10^{-2}$ in the Cu-going direction and $A\varepsilon_{rec} = 1.81 \times 10^{-2}$ in the Au-going direction at high p_T ($2.5 - 5$ GeV/c). There also appears to be a dependence on centrality, although it is not nearly as strong. The acceptance and efficiency changes from $A\varepsilon_{rec} = 2.23 \times 10^{-3}$ in the Cu-going direction and $A\varepsilon_{rec} = 2.37 \times 10^{-3}$ in the Au-going direction in central events ($0\% - 20\%$ centrality) to $A\varepsilon_{rec} = 2.41 \times 10^{-3}$ in the Cu-going direction and $A\varepsilon_{rec} = 3.83 \times 10^{-3}$ in the Au-going direction in peripheral events ($40\% - 93\%$).

Table 3.3. Centrality-weighted acceptance and efficiency values for each kinematic bin used in this analysis.

Rapidity Bin	Centrality Bin	Transverse Momentum Bin (GeV/*c*)	Centrality-Weighted $A\varepsilon_{\mathrm{rec}}$
1.2< y < 2.2	0%-93%	$1 < p_T < 5$	2.23×10^{-3}
1.2< y < 2.2	0%-20%	$1 < p_T < 5$	2.23×10^{-3}
1.2< y < 2.2	20%-40%	$1 < p_T < 5$	2.10×10^{-3}
1.2< y < 2.2	40%-93%	$1 < p_T < 5$	2.41×10^{-3}
-2.2 < y < -1.2	0%-93%	$1 < p_T < 5$	2.90×10^{-3}
-2.2 < y < -1.2	0%-20%	$1 < p_T < 5$	2.37×10^{-3}
-2.2 < y < -1.2	20%-40%	$1 < p_T < 5$	3.34×10^{-3}
-2.2 < y < -1.2	40%-93%	$1 < p_T < 5$	3.83×10^{-3}
1.2 < y < 1.8	0%-93%	$1 < p_T < 5$	1.71×10^{-3}
1.8 < y < 2.2	0%-93%	$1 < p_T < 5$	2.98×10^{-3}
-2.2 < y < -1.8	0%-93%	$1 < p_T < 5$	4.27×10^{-3}
-1.8 < y < -1.2	0%-93%	$1 < p_T < 5$	2.13×10^{-3}

1.2 < y < 2.2	0%-93%	$1 < p_T \leq 2.5$	1.21×10^{-3}
-2.2 < y < -1.2	0%-93%	$1 < p_T \leq 2.5$	1.86×10^{-3}
1.2 < y < 2.2	0%-93%	$2.5 < p_T < 5$	1.69×10^{-2}
-2.2 < y < -1.2	0%-93%	$2.5 < p_T < 5$	1.81×10^{-2}

3.6 Invariant Yield and Nuclear-Modification Factor Calculations

As indicated by Table 3.3, the data are binned as a function of transverse momentum, rapidity, and centrality over the range $1 < p_T < 5$ GeV$/c$, $1.2 < |y| < 2.2$, and $0\% - 93\%$ centrality before calculating the final physics quantities: the invariant yield and nuclear-modification factor.

First, the invariant yield is calculated in each kinematic bin as described in Eq. 3.11,

$$BR\frac{\mathrm{d}^2N_\phi}{\mathrm{d}y\mathrm{d}p_T} = \frac{1}{\Delta y \Delta p_T}\frac{N_\phi}{A\varepsilon_{rec}N_{evt}} \ , \tag{3.11}$$

where the branching ratio to dimuons from Table 1.2 is $BR(\phi \to \mu^+\mu^-) = (2.87 \pm 0.19) \times 10^{-4}$ [7], N_{evt} is the number of sampled MB events within the centrality bin selection ($N_{evt} =$ 4.73 billion for $0\% - 93\%$ centrality), N_ϕ is the number of ϕ mesons reconstructed with the muon arms, $A\varepsilon_{\mathrm{rec}}$ is the appropriate detector acceptance and reconstruction efficiency from Table 3.3, and Δy and Δp_T are the bins in rapidity and transverse momentum, respectively. After calculating the invariant yield in each kinematic bin, the values are plotted as function of

number of participating nucleons (centrality), transverse momentum, and rapidity. Although the invariant yield results provide important physics conclusions on their own, the nuclear-modification factors must be calculated to evaluate the nuclear matter effects on ϕ meson production in Cu+Au collisions relative to *p*+*p* collisions.

In Eq. 1.14 from Sec. 1.2.4, the nuclear-modification factor was introduced and defined as the ratio of the invariant yield in A+B collisions to that in *p*+*p* collisions at the same center-of-mass energy, scaled by the number of nucleon-nucleon collisions. In the case of Cu+Au collisions, this can be written as

$$R_{\mathrm{CuAu}} = \frac{\frac{\mathrm{d}^2 N_{\mathrm{CuAu}}}{\mathrm{d}y\mathrm{d}p_T}}{N_{\mathrm{coll}} \times \frac{\mathrm{d}^2 N_{pp}}{\mathrm{d}y\mathrm{d}p_T}}, \tag{3.12}$$

where R_{CuAu} is the nuclear modification in Cu+Au collisions, $\frac{\mathrm{d}^2 N_{\mathrm{CuAu}}}{\mathrm{d}y\mathrm{d}p_T}$ is the invariant yield in Cu+Au collisions as described by Eq. 3.11, $\frac{\mathrm{d}^2 N_{pp}}{\mathrm{d}y\mathrm{d}p_T}$ is the invariant yield in *p*+*p* collisions at 200 GeV from Ref. [19], and N_{coll} is the number of binary nucleon-nucleon collisions. As with the invariant yield, the nuclear-modification factor is calculated and plotted as a function of number of participating nucleons N_{part}, rapidity, and transverse momentum. The values for N_{coll} and N_{part} are taken from a Glauber simulation using similar methods as described in Sec. 1.2.4. They are summarized in Table 3.4 below. The results of this analysis are presented in Chapter 4.

Table 3.4. The official PHENIX values for the number of binary collisions and number of participating nucleons from a Glauber simulation.

Centrality Bin	N_{coll}	N_{part}
0%-93%	108.9 ± 5.0	62.3 ± 0.7
0%-20%	313.8 ± 28.4	154.8 ± 4.1
20%-40%	129.3 ± 12.4	80.4 ± 3.3
40%-93%	21.6 ± 1.0	19.5 ± 0.5

3.7 Systematic Uncertainty Estimation

The last remaining step in this analysis is an estimation of the systematic uncertainties. In addition to the statistical errors that arise from the number of events analyzed, this measurement is also subject to systematic uncertainties. Systematic uncertainties are generally associated with detector inefficiencies or errors on the data analysis techniques. In order to identify the systematic uncertainties, a thorough study is done on the performance of each detector involved and every step of the data analysis. Next, a method is developed to estimate each of the systematic errors, and these errors are included as an uncertainty on the reported values.

In this paper, the systematic uncertainties can be broken into three different types:

1. Type-A: point-to-point uncorrelated systematic uncertainties. For Type-A systematics, the measured points vary independently with one another within the error limit.

2. Type-B: point-to-point correlated systematic uncertainties. In this case, the measured points vary in a manner that depends on the other data points. The data points change in a correlated fashion within error limits.

3. Type-C: global systematic errors. Type-C systematics are also point-to-point correlated, but they affect all of the points in a coherent manner. For example, the data points can either scale up or down together within the error limit by a fixed percentage of their central values.

In the remainder of this subsection, each of the systematic uncertainties affecting this measurement are presented, as well as a summary of how they were estimated. The systematics are summarized in Tables 3.5 and 3.6.

Table 3.5. Systematic uncertainties included in the invariant yield calculation.

Type	Origin	Value
A	Signal extraction	2%-31%
B	MuID efficiency	2%
B	MuTr efficiency	2%
B	$A\varepsilon_{\mathrm{rec}}$	13%
B	ϕ candidate selection	3%
B	Like-sign background subtraction	5%
C	MB trigger	3%

Table 3.6. Systematic uncertainties included in the nuclear-modification factor calculations.

Type	Origin	Value
A	Signal extraction	2%-31%
A	p+p reference (integrated centrality only)	5%-13%
B	MuID efficiency	4%
B	MuTr efficiency	2%
B	$A\varepsilon_{\mathrm{rec}}$	13%
B	ϕ candidate selection	3%
B	Like-sign background subtraction	5%
B	N_{coll} (centrality bins only)	5%-10%
C	MB trigger	10%
C	N_{coll} (integrated centrality only)	5%
C	p+p reference (centrality bins only)	11%

3.7.1 Type-A Systematics

There are several contributors to the Type-A systematic uncertainties, which are the point-to-point uncorrelated systematics. First, the signal extraction uncertainty is assigned $2\% - 31\%$, depending on the kinematic bin. These values come from the largest uncertainty when changing the parameters and fits for signal extraction (α fit, correlated background fit, ρ and ω fit, and ϕ fit) as described in Sec. 3.4. In addition, the α fit is allowed to range over the errors in the fit parameters. This systematic uncertainty is dominated by fluctuations in the backgrounds, for which many fits and fit ranges are tested, including an exponential plus a third-order polynomial, a power plus a first-order polynomial, a power plus a constant, and a third-order polynomial. The largest systematic uncertainty on signal extraction is associated with the forward rapidity (Cu-going direction) central events ($0\% - 20\%$ centrality) with $1 < p_T < 5$ GeV/c, which is a bin with low statistics and high background. The smallest signal extraction systematic uncertainty comes from the backward rapidity (Au-going direction) peripheral events ($0\% - 93\%$ centrality) with $2.5 < p_T < 5$ GeV/c, which is a bin with relatively high statistics and low background. This systematic uncertainty is included in both the invariant yield and nuclear-modification factor calculations.

For the integrated centrality ($0\% - 93\%$), the p+p reference uncertainty is also included as a Type-A systematic on the nuclear-modification factor calculations. This systematic uncertainty component varies from $5\% - 13\%$ and arises from the uncertainty on the ϕ yields in the p+p reference [19].

Each component of the Type-A systematic uncertainty is added in quadrature with the statistical uncertainty. The resultant uncertainty is included on the plots as an error bar.

3.7.2 Type-B Systematics

Type-B systematic uncertainties are the correlated point-to-point systematics. For the nuclear-modification values, there is a 4% systematic uncertainty on the MuID efficiency and a 2% systematic uncertainty on the MuTr efficiency, which comes from the values in the *p*+*p* reference data [19]. For the invariant yields, the MuTr efficiency uncertainty remains at 2%, while the MuID efficiency uncertainty decreases to 2% in Cu+Au collisions [41]. Another Type-B systematic uncertainty that only affects the nuclear-modification factors is the N_{coll} uncertainty of $5\% - 10\%$, which comes from the fact that N_{coll} carries a statistical uncertainty itself, as shown in Table 3.4. For Type-B systematics, the N_{coll} uncertainty only affects nuclear-modification factors calculated in centrality bins. The remaining components of the Type-B systematic uncertainty affect both the nuclear-modification factors and the invariant yields. These include the acceptance and efficiency uncertainty (13%), the ϕ meson candidate selection uncertainty (3%), and the like-sign background uncertainty (5%), which will each be described in detail in the remainder of this subsection.

For the acceptance and efficiency uncertainty, the effect of changing the p_T and y distributions in simulation to match real data is quantified, taking into account the error bars, which are the statistical uncertainties and Type-A systematic uncertainties added in quadrature. This is accomplisehd by employing the bowtie method, in which the bottom of one error bar is fit with the top of the other error bar, and vice versa. This is a very conservative estimation of the acceptance and efficiency systematic uncertainty; however, since this analysis is limited by extremely low statistics, the systematic uncertainty is still within the statistical error bar. Figures 3.19 and 3.20 show plots of the transverse momentum and rapidity distributions, respectively, in the PYTHIA simulation (dashed lines) and in real data (solid lines) for both

forward rapidity (red) and backward rapidity (blue). The data are plotted at the average transverse momentum or rapidity in the bin, and PYTHIA is plotted in the same kinematic bins as real data for consistency.

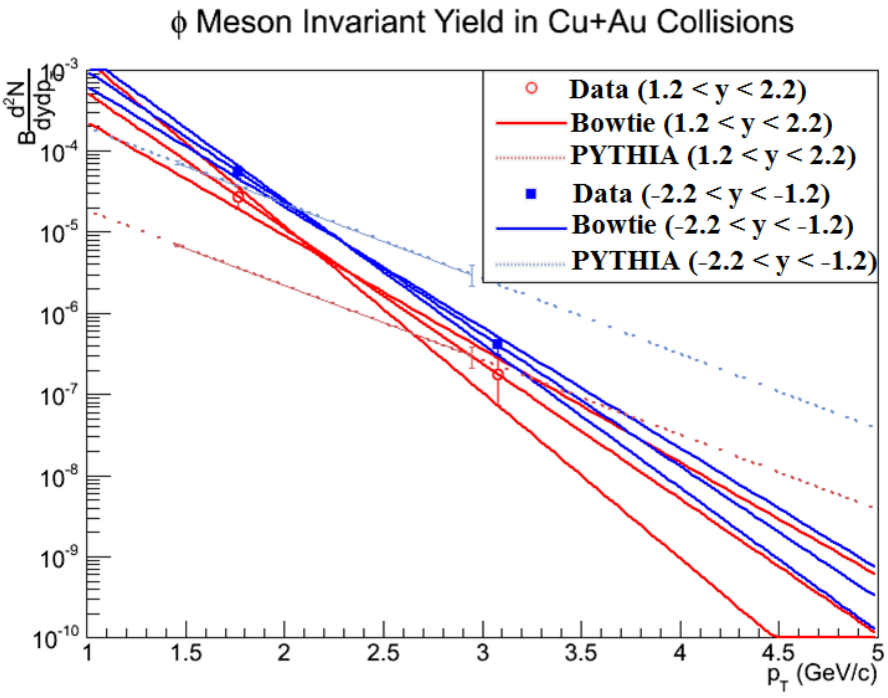

Figure 3.19. The transverse momentum distributions in real data (solid) and the PYTHIA simulation (dashed) for both forward rapidity (red) and backward rapidity (blue). The PYTHIA distributions are altered to match real data over the error bars.

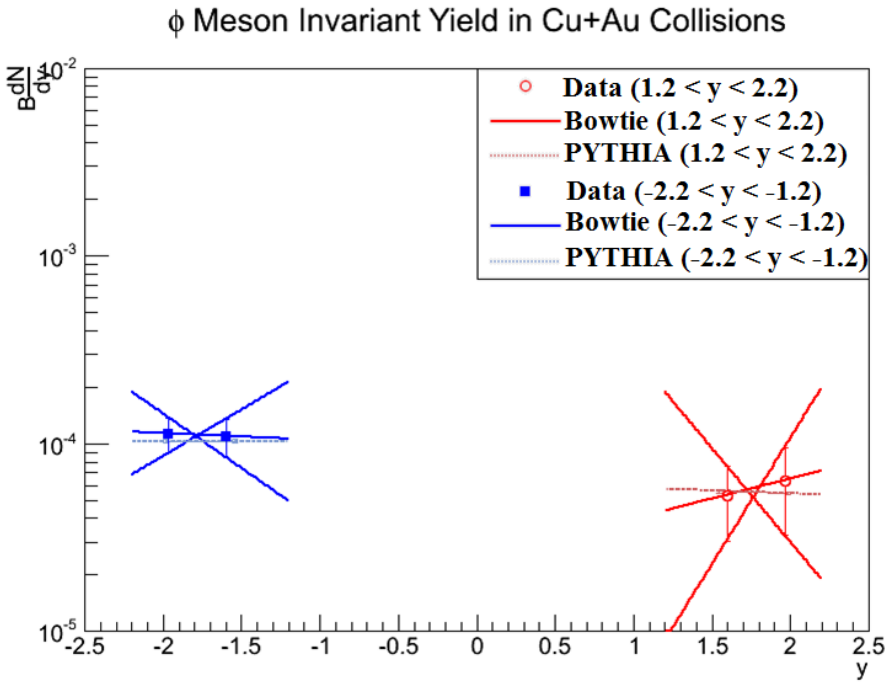

Figure 3.20. The rapidity distributions in real data (solid) and the PYTHIA simulation (dashed) for both forward rapidity (red) and backward rapidity (blue). The PYTHIA distributions are altered to match real data over the error bars.

For the ϕ candidate selection uncertainty, each of the quality cuts summarized in Table 3.1 is compared for reconstructed ϕ mesons in real data (black) and in the PISA simulation (red), as shown in Fig. 3.21-3.29 below, where the dotted line in each figure represents the applied cut. In each case, the data and simulation distributions are consistent, except for the lastgap, nidhits, and ntrhits variables. Accordingly, the cut value for each of these variables is changed in both simulation and in data and the invariant yield is recalculated. In each case, the invariant yield is consistent within statistical errors, and a 3% systematic uncertainty is applied due to the largest variation, which came from changing the lastgap cut.

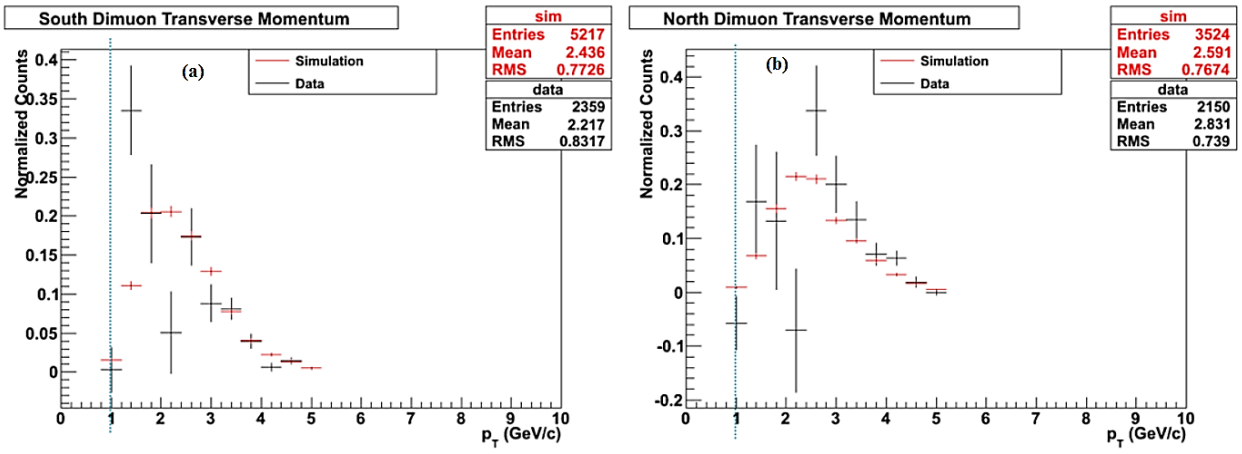

Figure 3.21. Transverse momentum distributions for reconstructed ϕ mesons in real data (black) and in the PISA simulation (red). The quality cut is represented by the dotted line.

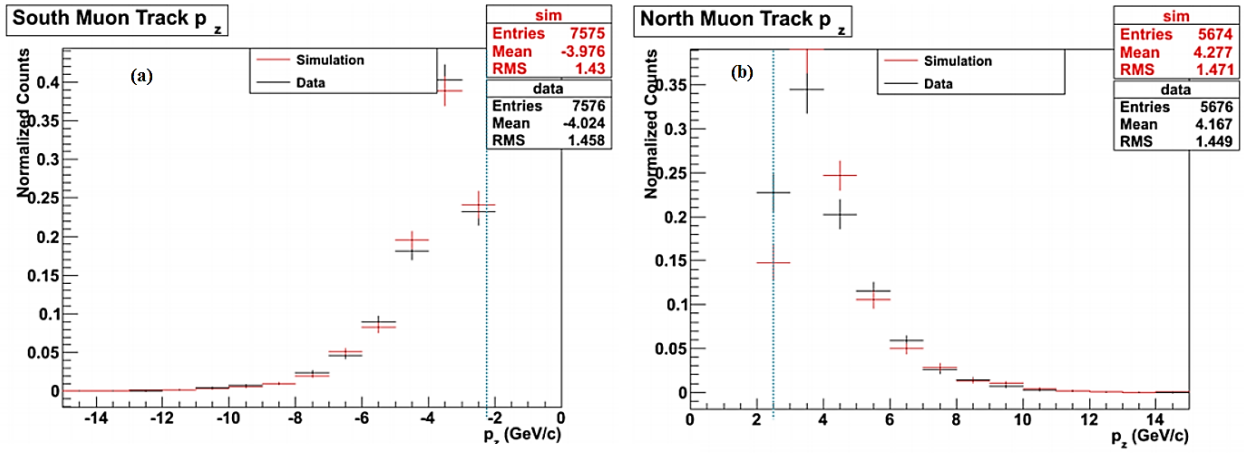

Figure 3.22. Momentum distributions along the beam axis for reconstructed ϕ mesons in real data (black) and in the PISA simulation (red). The quality cut is represented by the dotted line.

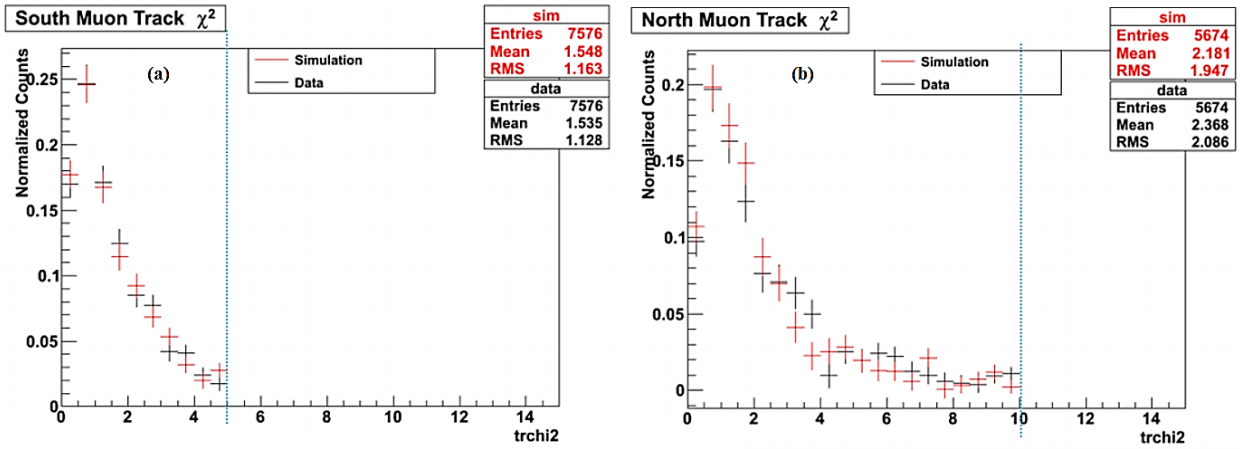

Figure 3.23. Track χ^2 distributions for reconstructed ϕ mesons in real data (black) and in the PISA simulation (red). The quality cut is represented by the dotted line.

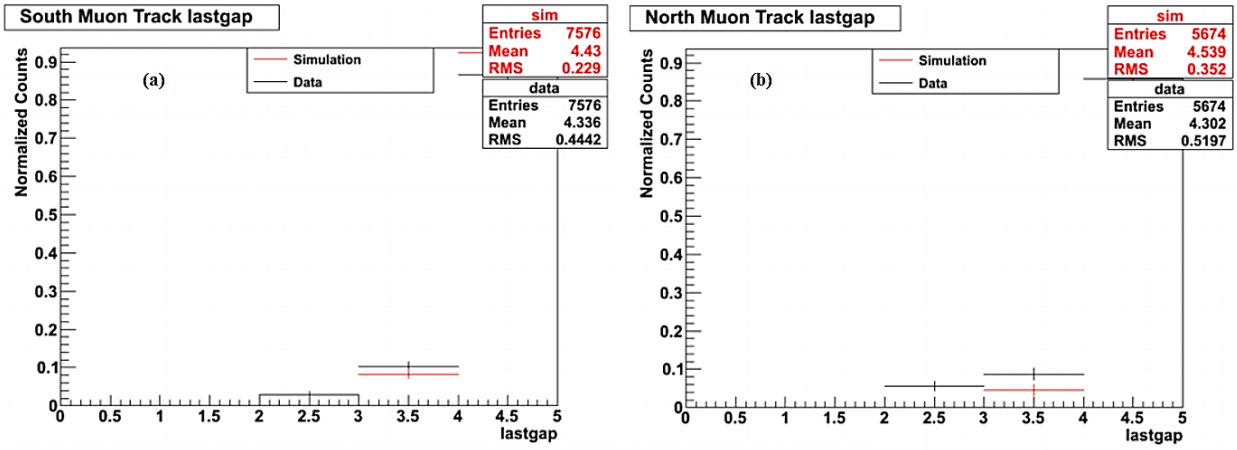

Figure 3.24. Lastgap distributions for reconstructed ϕ mesons in real data (black) and in the PISA simulation (red).

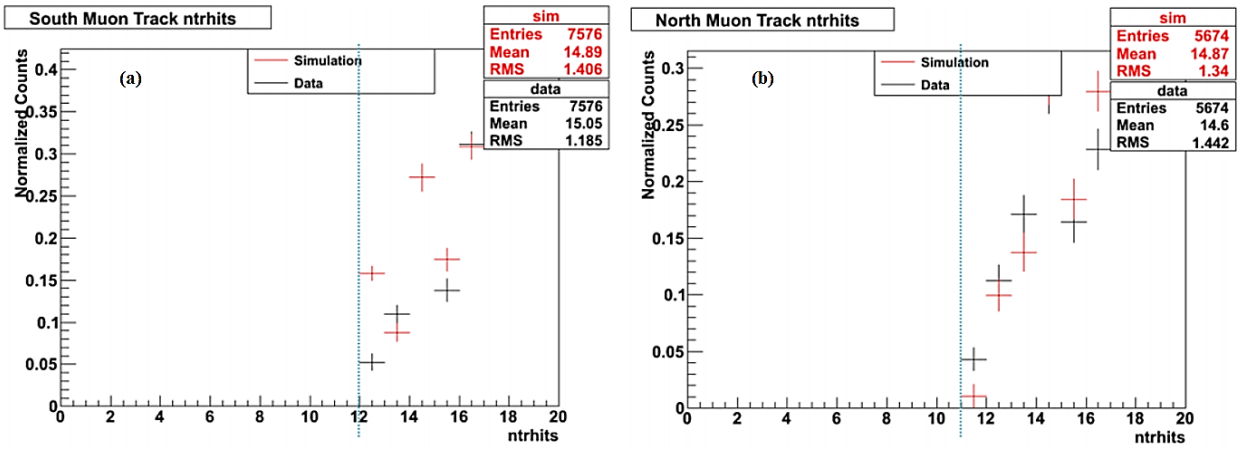

Figure 3.25. ntrhits distributions for reconstructed ϕ mesons in real data (black) and in the PISA simulation (red). The quality cut is represented by the dotted line.

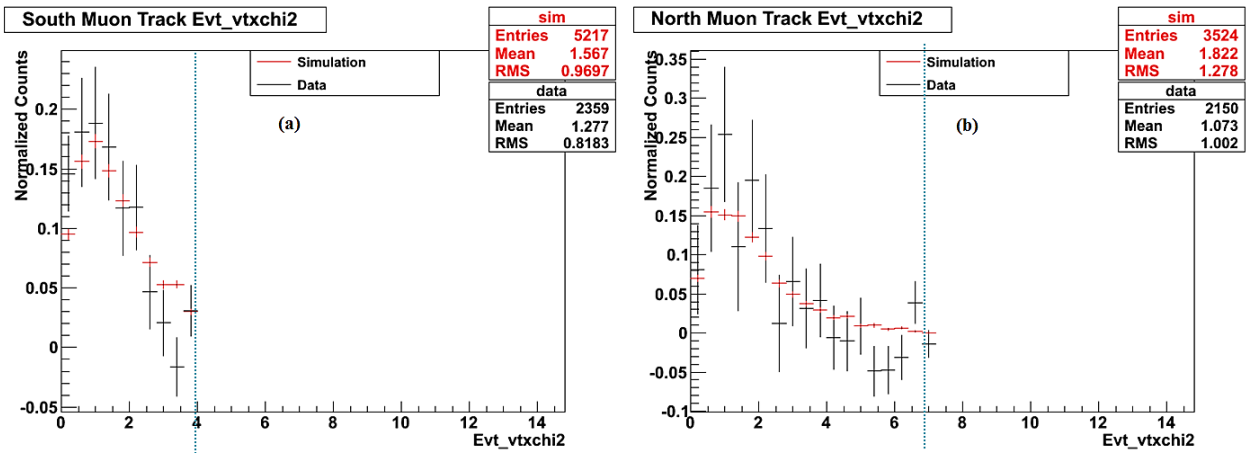

Figure 3.26. Vertex χ^2 distributions for reconstructed ϕ mesons in real data (black) and in the PISA simulation (red). The quality cut is represented by the dotted line.

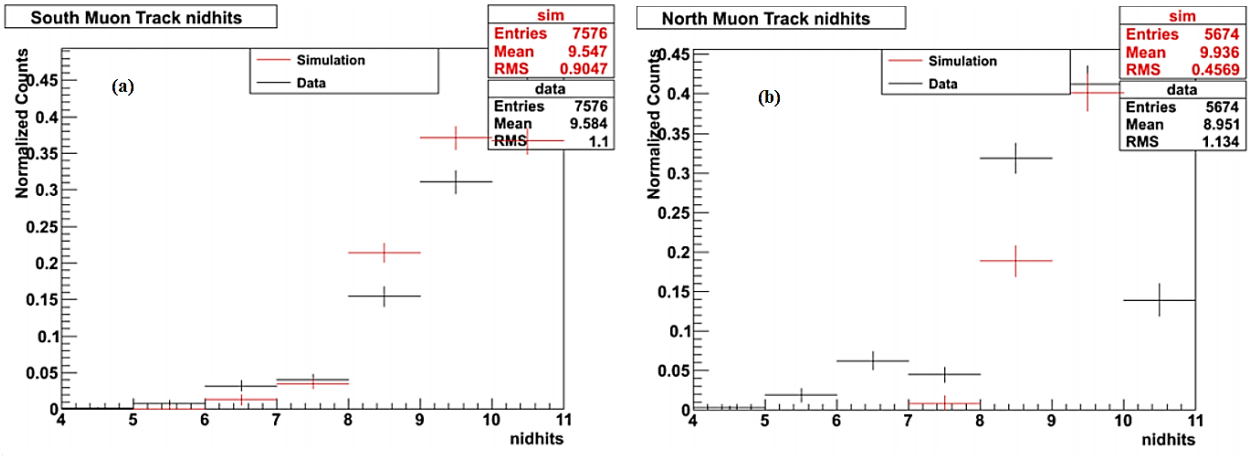

Figure 3.27. nidhits distributions for reconstructed ϕ mesons in real data (black) and in the PISA simulation (red).

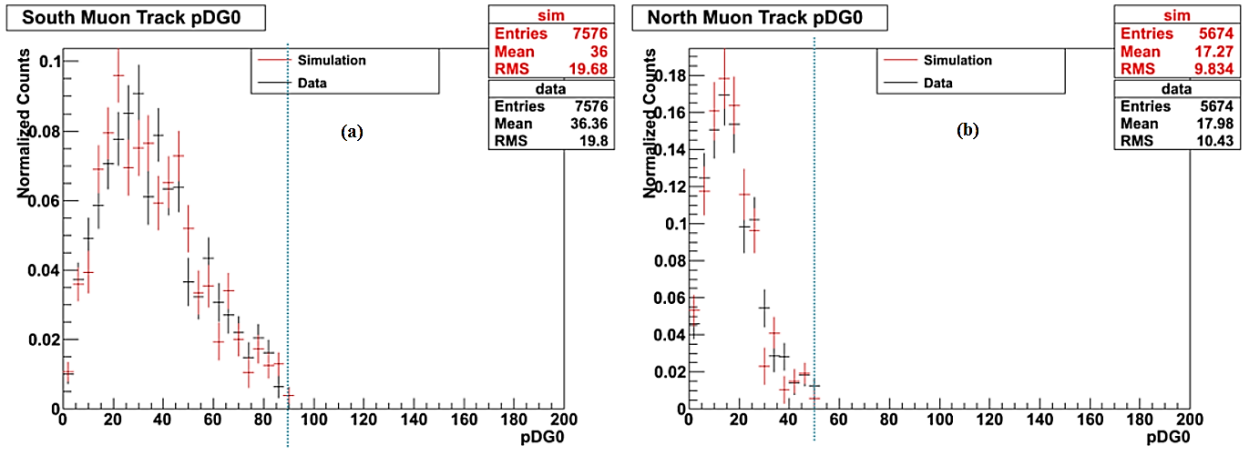

Figure 3.28. *pDG0* distributions for reconstructed ϕ mesons in real data (black) and in the PISA simulation (red). The quality cut is represented by the dotted line.

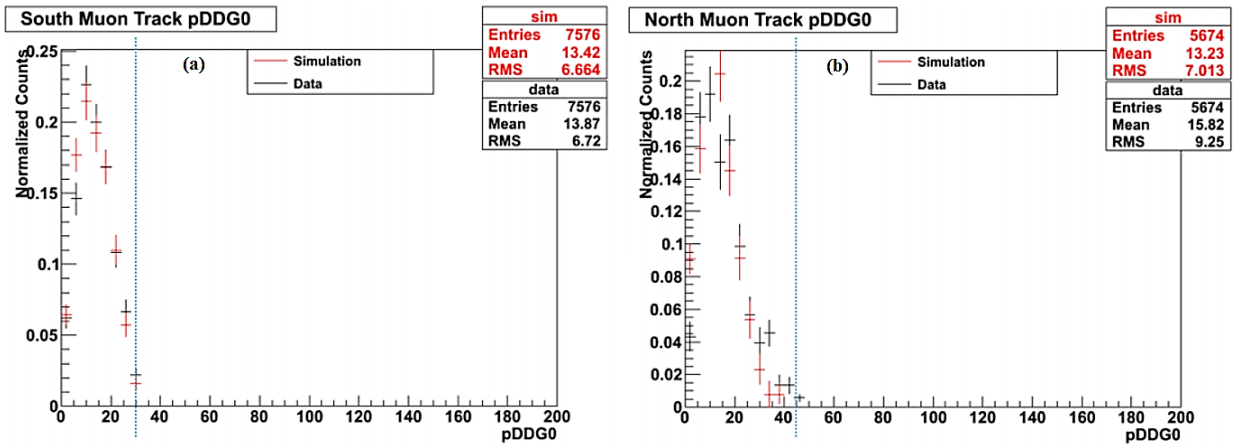

Figure 3.29. *pDDG0* distributions for reconstructed ϕ mesons in real data (black) and in the PISA simulation (red). The quality cut is represented by the dotted line.

Finally, for the like-sign uncertainty, the invariant yields calculated with the like-sign method are compared to those measured from the event mixing method. Once again, they were consistent within error bars, but a 5% systematic was assigned due to variations between the two methods.

The sources of the Type-B systematic uncertainty are added in quadrature with each other. This is displayed as boxes around the data points in the plots.

3.7.3 Type-C Systematics

Like the Type-B systematics, the Type-C systematic uncertainties are point-to-point correlated. In this case, the data points scale either up or down together. The MB trigger efficiency uncertainty of 3% in Cu+Au collisions [41] is used for the invariant yield calculations, while this value changes to 10% for nuclear-modification factor calculations, resulting from adding the efficiency uncertainties in *p*+*p* [19] and Cu+Au in quadrature.

A *p*+*p* reference uncertainty of 11%, which comes from the uncertainty on the ϕ yields in the *p*+*p* reference [19], is included as a Type-C systematic only for nuclear-modification calculations done in centrality bins. The final contributor to the Type-C systematics is the N_{coll} uncertainty of 5%, which arises from the fact that N_{coll} carries a statistical uncertainty itself, as shown in Table 3.4. For Type-C systematic uncertainties, the N_{coll} uncertainty only affects nuclear-modification factors calculated for integrated centrality ($0\% - 93\%$).

The appropriate Type-C systematics are added in quadrature with each other. The result is included on the plots as a global systematic stated in the legend.

4 RESULTS

The results of this analysis are published in Ref. [29] and also described in detail in this chapter.

4.1 Invariant Yields

The invariant yields are calculated as described by Eq. 3.11 in centrality, transverse momentum, and rapidity bins for ϕ mesons with $1 < p_T < 5$ GeV/c, $1.2 < |y| < 2.2$, and $0\% - 93\%$ centrality. The results are summarized in Tables 4.1-4.3 and plotted in Fig. 4.1-4.3.

In Table 4.1, the invariant yield is given as a function of centrality for $1 < p_T < 5$ GeV/c and $1.2 < |y| < 2.2$. The first value is the central value, followed by the Type-A systematic and statistical uncertainties, and lastly the Type-B systematic uncertainty. A $\pm 3\%$ Type-C global systematic uncertainty also applies. The invariant yield as a function of transverse momentum is summarized in Table 4.2 for $0\% - 93\%$ centrality and $1.2 < |y| < 2.2$. As with the previous table, the first value is the central value, followed by the Type-A systematic and statistical uncertainties, and lastly the Type-B systematic uncertainty. An additional $\pm 5.8\%$ Type-C global systematic uncertainty also applies. Table 4.3 shows the invariant yield as a function of rapidity for $0 - 93\%$ centrality and $1 < p_T < 5$ GeV/c. The first value is the central value, followed by the Type-A systematic and statistical uncertainties, and lastly the Type-B systematic uncertainty. A $\pm 5.8\%$ Type-C global systematic uncertainty also applies.

Table 4.1. Invariant yield results as a function of centrality for $1 < p_T < 5$ GeV/c and $1.2 < |y| < 2.2$.

Centrality Bin	$BR\frac{dN}{dy}$ (Cu-going)	$BR\frac{dN}{dy}$ (Au-going)
0%-20%	$(7.3 \pm 7.5 \pm 1.1) \times 10^{-5}$	$(3.4 \pm 1.0 \pm 0.5) \times 10^{-4}$
20%-40%	$(1.2 \pm 0.3 \pm 0.2) \times 10^{-4}$	$(1.2 \pm 0.3 \pm 0.2) \times 10^{-4}$
40%-93%	$(1.5 \pm 0.6 \pm 0.2) \times 10^{-5}$	$(2.7 \pm 0.7 \pm 0.4) \times 10^{-5}$

Table 4.2. Invariant yield results as a function of transverse momentum for 0%-93% centrality and $1.2 < |y| < 2.2$. The

p_T bin (GeV/c)	$BR\frac{d^2N}{dydp_T}$ (Cu-going) (GeV/c)$^{-1}$	$BR\frac{d^2N}{dydp_T}$ (Au-going) (GeV/c)$^{-1}$
1.0 – 2.5	$(2.7 \pm 0.8 \pm 0.4) \times 10^{-5}$	$(5.5 \pm 0.9 \pm 0.8) \times 10^{-5}$
2.5 – 5.0	$(1.8 \pm 1.0 \pm 0.3) \times 10^{-7}$	$(4.1 \pm 1.0 \pm 0.6) \times 10^{-7}$

Table 4.3. Invariant yield results as a function of rapidity for $1 < p_T < 5$ GeV/c and 0%-93% centrality.

Rapidity Bin	$BR\frac{dN}{dy}$ (Cu-going)	$BR\frac{dN}{dy}$ (Au-going)
1.8 – 2.2	$(6.4 \pm 3.1 \pm 0.9) \times 10^{-5}$	$(1.1 \pm 0.2 \pm 0.2) \times 10^{-4}$
1.2 – 1.8	$(5.3 \pm 2.3 \pm 0.8) \times 10^{-5}$	$(1.1 \pm 0.3 \pm 0.2) \times 10^{-4}$

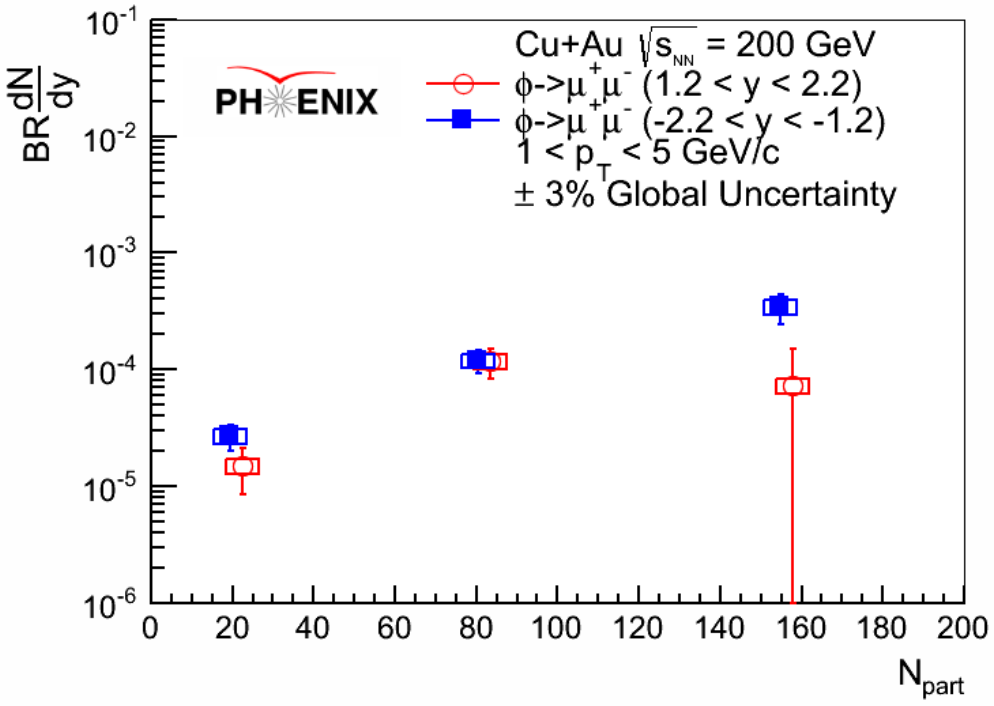

Figure 4.1. Invariant yield plotted as a function of the number of participating nucleons for $1.2 < |y| < 2.2$ and $1 < p_T < 5$ GeV/*c*.

In Fig. 4.1, the invariant yield plotted as a function of the number of participating nucleons, N_{part}, for $1.2 < |y| < 2.2$ and $1 < p_T < 5$ GeV/c. The data for this figure are summarized in Table 4.1. The data points for forward rapidity (Cu-going direction) are shifted along the x-axis to make the points visible. The data points for forward rapidity (Cu-going direction) are represented by open, red circles, while the data points for backward rapidity (Au-going direction) are represented by closed, blue squares. Recall from Sec. 1.2.2 that N_{part} is representative of centrality, with more central collisions having a larger value for N_{part}. The N_{part} and N_{coll} for each centrality bin are summarized in Table 3.4. With this knowledge, it appears that fewer ϕ mesons are produced in peripheral events than in central events; however, in such a low statistics environment, the error bar makes it difficult to make conclusions. For this reason, the forward/backward ratio is calculated and discussed in the following subsection.

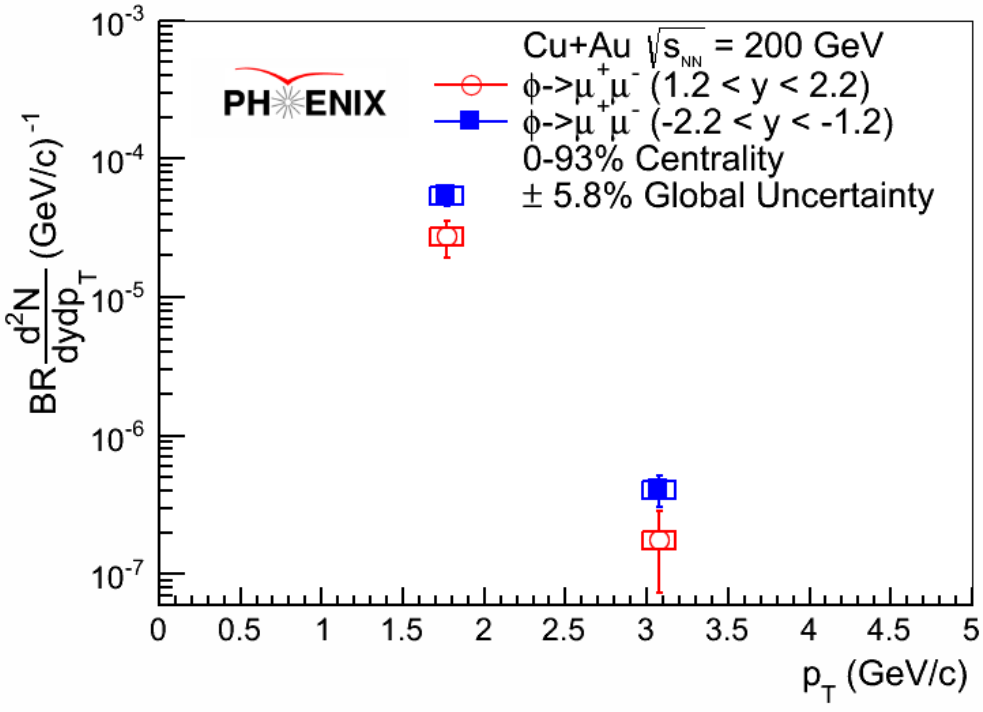

Figure 4.2. Invariant yield plotted as a function of transverse momentum for $1.2 < |y| < 2.2$ and 0%-93% centrality.

Figure 4.2 shows the invariant yield plotted as a function transverse momentum for $1.2 < |y| < 2.2$ and $0\% - 93\%$ centrality. The data for this figure are summarized in Table 4.2. The data points for forward rapidity (Cu-going direction) are represented by open, red circles, while the data points for backward rapidity (Au-going direction) are represented by closed, blue squares. The data points are placed at the mean transverse momentum of the bin. The invariant yield has an obvious dependence on transverse momentum, with a much higher production rate of ϕ mesons at low p_T, $1 - 2.5$ GeV/c, than at high p_T, $2.5 - 5$ GeV/c.

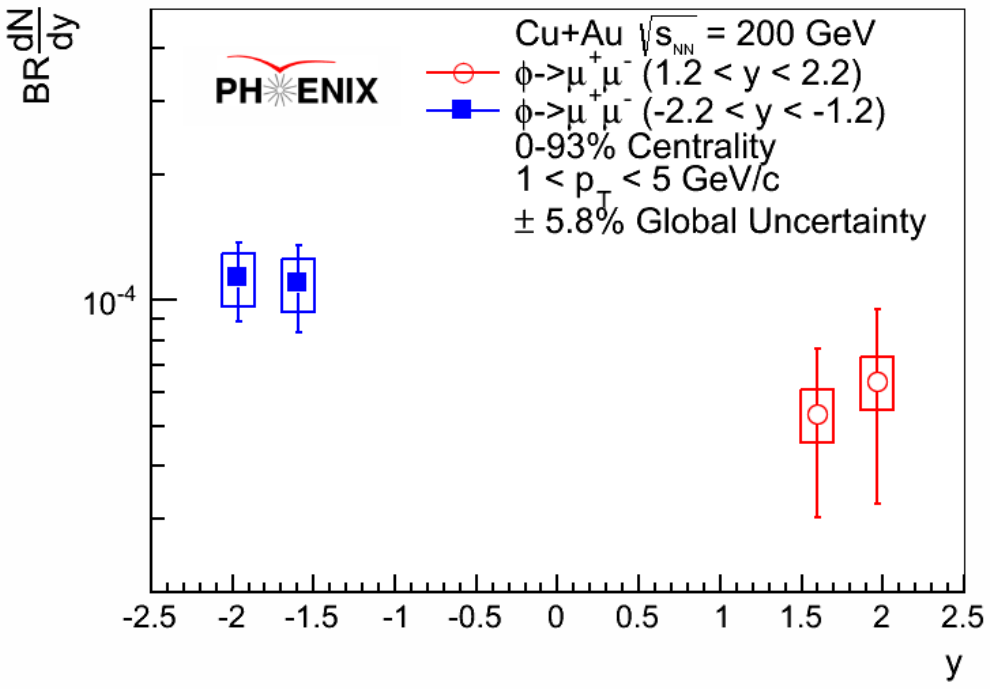

Figure 4.3. Invariant yield plotted as a function of rapidity for 0%-93% centrality and $1 < p_T < 5$ GeV/c.

In Fig. 4.3, the invariant yield is plotted as a function rapidity for $0\% - 93\%$ centrality and $1 < p_T < 5$ GeV/c, with the data points placed at the mean rapidity of the bin. The data for this figure are summarized in Table 4.3. The data points for forward rapidity (Cu-going direction) are represented by open, red circles, while the data points for backward rapidity (Au-going direction) are represented by closed, blue squares. It is apparent that more ϕ mesons are produced in the Au-going ($-2.2 < y < -1.2$) direction than in the Cu-going ($1.2 < y < 2.2$) direction. This observation may be explained by the larger multiplicity in the Au-going direction, or it could be due to the HNM and CNM effects on ϕ production in Cu+Au collisions at 200 GeV. These nuclear matter effects will be further assessed in Sec 4.2.

4.1.1 Forward/Backward Ratio

The differences in ϕ production at forward and backward rapidity for different centralities can be quantified by the ratio of the invariant yields measured at forward rapidity (Cu-going direction, $1.2 < y < 2.2$) to those at backward rapidity (Au-going direction, $-2.2 < y < -1.2$). This ratio, called the forward/backward ratio, is summarized in Table 4.4 and plotted in Fig. 4.4 alongside the *J/ψ* result published in Ref. [41]. One benefit of taking this ratio is that many of the systematic uncertainties cancel. In fact, the only remaining systematic uncertainties are the Type-A signal extraction uncertainty and the Type-B acceptance and efficiency uncertainty. In table 4.4, the first value is the central value, the following value is the statistical and Type-A systematic uncertainty, and the last value is the systematic uncertainty of Type-B. There is no Type-C global systematic uncertainty on this ratio because the global systematics cancel.

Table 4.4. The forward to backward ratio using the values from Table 4.1.

Centrality Bin	Forward/Backward Ratio
0%-20%	$0.2^{+0.3}_{-0.2} \pm < 0.1$
20%-40%	$1.0^{+0.4}_{-0.3} \pm 0.1$
40%-93%	$0.6^{+0.4}_{-0.3} \pm 0.1$

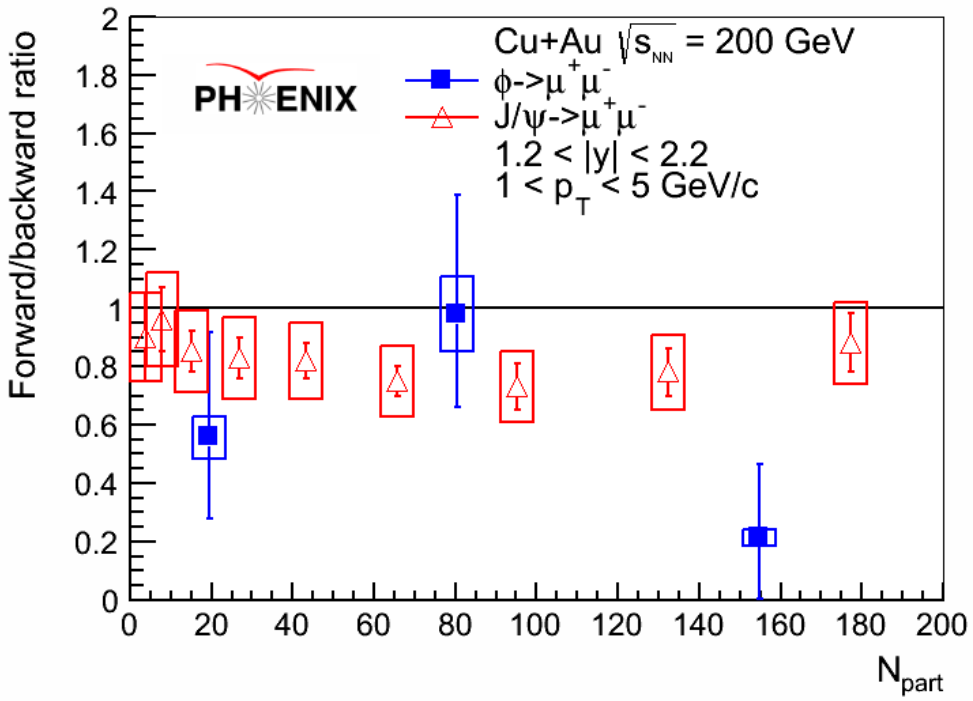

Figure 4.4. The forward/backward ratio as a function of the number of participating nucleons for $1.2 < |y| < 2.2$ and $1 < p_T < 5$ GeV/c.

Figure 4.4 gives the forward/backward ratio as a function of the number of participating nucleons for $1.2 < |y| < 2.2$ and $1 < p_T < 5$ GeV/c. The forward rapidity corresponds to the Cu-going direction, while backward rapidity is the Au-going direction. The forward/backward ratio for ϕ mesons is represented by blue, closed squares, while the *J/ψ* result is shown by red, open triangles. The forward/backward ratio in ϕ production in central collisions appears to be much smaller than that in *J/ψ* production at the same energy and in the same collision system [41]. In fact, it appears that the forward/backward ratio in ϕ production in Cu+Au collisions at 200 GeV is $\sim$0.2 in the most central events, compared to only $\sim$0.8 in *J/ψ* production. For ϕ production, the forward/backward ratio is furthest from unity in the most central events with $0\% - 20\%$ centrality. This can be further expressed by calculating the *p*-value, or probability of observing the ratio to be greater than or equal to unity. The *p*-value for this data point is 1.3%, corresponding to a statistical significance of 2.3σ. This means the forward/backward ratio of ϕ production in Cu+Au collisions at 200 GeV is below unity with a confidence-level of 99%. If this ratio depended solely on differences in the particle multiplicity in the Cu-going direction compared to the Au-going direction, the ratio would be much larger. This is because the particle multiplicity should only be about 20% higher in the Au-going direction compared to the Cu-going direction [44]. Therefore, this very small forward/backward ratio is likely due to nuclear matter effects, such as recombination or strangeness enhancement.

4.2 Nuclear-Modification Factors

Although the invariant yield results provide some interesting physics knowledge on their own, the nuclear-modification factor is evaluated to further study the effects of HNM and CNM at play in this asymmetric heavy-ion collision system. The nuclear-modification factors were

formed from the invariant yields as described by Eq. 3.12 in centrality, transverse momentum, and rapidity bins. The results are summarized in Tables 4.5-4.7 and plotted in Fig. 4.5-4.7.

In Table 4.5, the nuclear-modification factor is given as a function of centrality for $1 < p_T < 5$ GeV/c and $1.2 < |y| < 2.2$. The first value is the central value, followed by the Type-A systematic and statistical uncertainties, and lastly the Type-B systematic uncertainty. A $\pm 15\%$ Type-C global systematic uncertainty also applies. The nuclear-modification factor as a function of transverse momentum is summarized in Table 4.6 for $0\% - 93\%$ centrality and $1.2 < |y| < 2.2$. The first value is the central value, followed by the Type-A systematic and statistical uncertainties, and lastly the Type-B systematic uncertainty. An additional $\pm 11\%$ Type-C global systematic uncertainty also applies. In Table 4.6, the nuclear-modification factor is tabulated as a function of rapidity for $1 < p_T < 5$ GeV/c and $0\% - 93\%$ centrality. The first value is the central value, followed by the Type-A systematic and statistical uncertainties, and lastly the Type-B systematic uncertainty. An additional $\pm 11\%$ Type-C global systematic also applies.

Table 4.5. Nuclear-modification factor results as a function of centrality for $1 < p_T < 5$ GeV/c and $1.2 < |y| < 2.2$.

Centrality Bin	R_{CuAu} (Cu-going)	R_{CuAu} (Au-going)
0%-20%	$0.4 \pm 0.4 \pm 0.1$	$1.7 \pm 0.5 \pm 0.3$
20%-40%	$1.4 \pm 0.4 \pm 0.3$	$1.4 \pm 0.3 \pm 0.3$
40%-93%	$1.1 \pm 0.5 \pm 0.2$	$1.9 \pm 0.5 \pm 0.3$

Table 4.6. Nuclear-modification factor results as a function of transverse momentum for 0%-93% centrality and 1.2 < |y| < 2.2.

p_T bin (GeV/c)	R_{CuAu} (Cu-going)	R_{CuAu} (Au-going)
1.0 – 2.5	$1.1 \pm 0.4 \pm 0.2$	$2.3 \pm 0.4 \pm 0.4$
2.5 – 5.0	$0.6 \pm 0.4 \pm 0.1$	$1.4 \pm 0.3 \pm 0.2$

Table 4.7. Nuclear-modification factor results as a function of rapidity for 1 < p_T < 5 GeV/c and 0%-93% centrality.

Rapidity Bin	R_{CuAu} (Cu-going)	R_{CuAu} (Au-going)
1.8 – 2.2	$1.2 \pm 0.6 \pm 0.2$	$2.1 \pm 0.5 \pm 0.3$
1.2 – 1.8	$0.7 \pm 0.3 \pm 0.1$	$1.4 \pm 0.4 \pm 0.2$

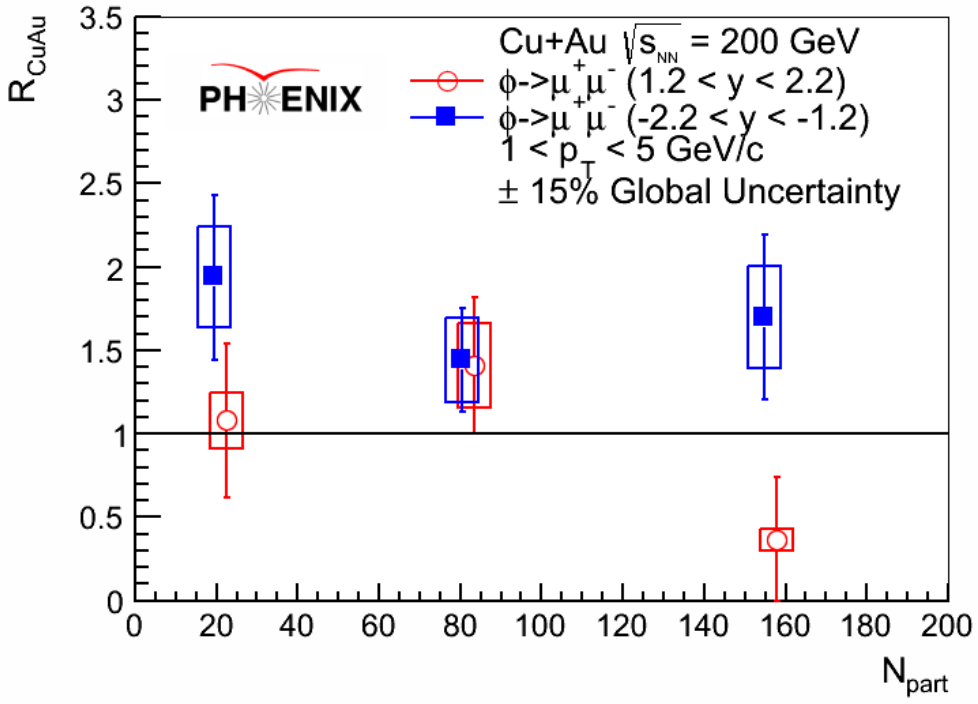

Figure 4.5. Nuclear-modification factor plotted as a function of the number of participating nucleons for $1.2 < |y| < 2.2$ and $1 < p_T < 5$ GeV/c.

Figure 4.5 shows the nuclear-modification factor plotted as a function of number of participating nucleons for $1.2 < |y| < 2.2$ and $1 < p_T < 5$ GeV/c. The data for this figure are summarized in Table 4.5. The data points for forward rapidity (Cu-going direction) are shifted along the x-axis to make the points visible. The data points for forward rapidity (Cu-going direction) are represented by open, red circles, while the data points for backward rapidity (Au-going direction) are represented by closed, blue squares. The nuclear-modification shows a dependence on both centrality and rapidity. For all centralities, the nuclear-modification in the Au-going direction ($-2.2 < y < -1.2$) is greater than unity, while the nuclear-modification in the Cu-going direction ($1.2 < y < 2.2$) appears to be consistent with unity except for in the case of the most central events, $0\% - 20\%$, where the value seems to drop below unity. The

rapidity dependence appears to be similar to the trend previously observed in PHENIX for ϕ mesons in *d*+Au collisions at the same rapidity and center-of-mass energy [18]. Furthermore, the ALICE Collaboration observed a similar trend at large rapidity ($-4.46 < y < -2.96$ and $2.03 < y < 3.53$) in *p*+Pb collisions at a higher energy of 5.02 TeV at the LHC [28]. In that paper, an enhancement was observed in the Pb-going direction while the *p*-going direction was either suppressed or consistent with unity, similar to what is observed for the Au-going and Cu-going directions here.

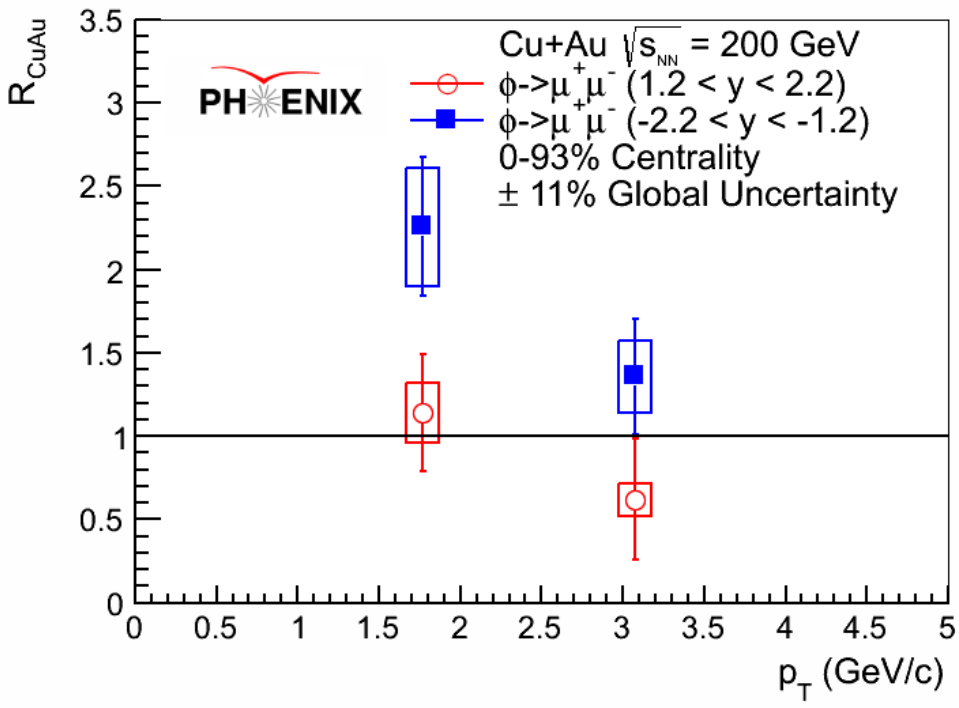

Figure 4.6. Nuclear-modification factor plotted as a function of transverse momentum for $1.2 < |y| < 2.2$ and 0%-93% centrality.

In Fig. 4.6, the nuclear-modification factor is plotted as a function of transverse momentum for $1.2 < |y| < 2.2$ and $0\% - 93\%$ centrality, with the data points placed at the

mean p_T of the bin. The data for this figure are summarized in Table 4.6. The data points for forward rapidity (Cu-going direction) are represented by open, red circles, while the data points for backward rapidity (Au-going direction) are represented by closed, blue squares. For this measurement, $0\% - 93\%$ centrality events were used, although Fig. 4.1 would suggest that the data are dominated by central events rather than peripheral events. In Fig. 4.6, the nuclear-modification at forward rapidity (Cu-going direction) appears to be consistent with unity for all transverse momentum ranges. However, at backward rapidity (Au-going direction), there appears to be an enhancement at low transverse momentum, similar in scale to what was observed in the Au-going direction in *d*+Au collisions [18]. This may indicate similar HNM and CNM effects in Cu+Au and *d*+Au collision systems.

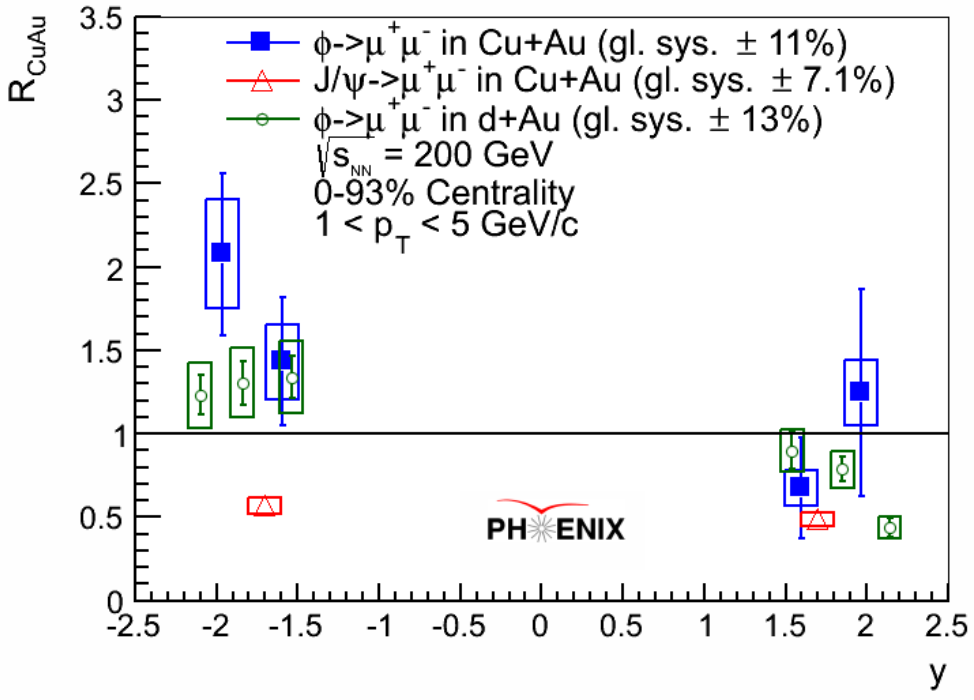

Figure 4.7. Nuclear-modification factor plotted as a function of rapidity for $1 < p_T < 5$ GeV/*c* and 0%-93% centrality.

Fig 4.7 shows the nuclear-modification factor plotted as a function of rapidity for $1 < p_T < 5$ GeV/c and $0\% - 93\%$ centrality. The data points are placed at the mean rapidity of the bin, and the data for this figure are summarized in Table 4.7. The data points for ϕ mesons in Cu+Au collisions are represented by closed, blue squares. The data points for ϕ mesons in *d*+Au collisions and *J/ψ* mesons in Cu+Au collisions are shown as open, green circles and open, red triangles, respectivelyAs mentioned when discussing Fig. 4.5 and 4.6, the rapidity dependence of the nuclear-modification factor in Cu+Au collisions is very similar to what was observed in previous ϕ measurements at forward and backward rapidity in *d*+A and *p*+A collisions [18, 28]. Given the statistical limitations of this measurement, it is impossible to conclude that any of the Cu-going direction points show a significant expression. However, it is apparent in Fig. 4.7 that ϕ meson production in Cu+Au collisions is enhanced in the Au-going direction. To compare with other collision systems, the PHENIX *d*+Au result [18] is also shown in Fig. 4.7, along with the *J/ψ* measurement in the same collision system [41]. The *J/ψ* consists of a closed charm pair ($c\bar{c}$), which appears suppressed at all rapidities in Fig. 4.7, while the ϕ meson consists of closed strangeness ($s\bar{s}$), which appears to be unaffected at forward rapidity and enhanced at backward rapidity. In comparing the two, one can speculate that this may indicate different nuclear matter effects on the production of ϕ and *J/ψ* mesons in Cu+Au collisions. These differences between the two mesons were also observed in *d*+Au collisions [18].

In summary, the ϕ meson yields and nuclear modification factors in Cu+Au collisions are observed to be generally smaller in the Cu-going direction than in the Au-going direction. This observation is most apparent in central collisions, $0\% - 20\%$. The physics trends observed in this collision system appear to be consistent with what was observed in previous *p*(*d*)+Au collisions. This may be due to CNM effects on ϕ production in Cu+Au collisions, although

previous PHENIX ϕ measurements at mid-rapidity in Cu+Cu and Au+Au collisions [21] would suggest that HNM effects should also be at play in Cu+Au collisions. A precise measurement with high statistics is needed to make further physics comparisons and conclusions.

5 CONCLUSIONS AND FUTURE WORK

ϕ meson production and its nuclear modification have been measured in asymmetric Cu+Au collisions at $\sqrt{s_{NN}} = 200$ GeV for both the Cu-going direction ($1.2 < y < 2.2$) and the Au-going direction ($-2.2 < y < -1.2$) in the transverse momentum range $1.0\ \mathrm{GeV}/c < p_T < 5.0\ \mathrm{GeV}/c$ via the dimuon decay channel. The results presented here extend measurements of ϕ meson production from smaller collision species, specifically *p*+*p* and *d*+Au, to a heavy-ion system for the first time at this rapidity region at RHIC.

It was shown that the particle multiplicity in heavy-ion collisions at these rapidities produces a very challenging environment for extracting the ϕ meson signal, explaining why previous measurements were thus limited to smaller collision systems. This paper presented a pioneering first measurement of ϕ meson production in heavy-ion collisions at forward and backward rapidities in 15 years of running the RHIC experiment. A procedure for modeling and removing the backgrounds was detailed, allowing for future measurements to be made in other heavy-ion systems.

The results of this analysis indicate an entanglement of HNM and CNM effects on ϕ meson production at forward and backward rapidities in heavy-ion collisions. Although ϕ meson production is an excellent probe for studying these effects, this particular study was statistically limited, making it difficult to draw strong conclusions. Therefore, these results await both theoretical predictions and more precise measurements with high statistics in order to make conclusions about whether HNM effects, such as recombination or strangeness enhancement, or CNM effects, such as the Cronin effect, may be at play here. Given the challenges to perform theoretical calculations at this mass and transverse momentum range, there are currently no theoretical predictions to compare with these results. However, the experimental results

themselves provide theorists with the opportunity to tune their models to real data. In addition, the techniques developed for this analysis are currently being employed by nuclear physicists at RHIC to repeat the ϕ meson measurement in the ^{3}He+Au dataset, which can be used to study CNM effects, and in the massive 2014 Au+Au dataset, in which QGP is formed. The measurement presented here, as well as these future planned measurements, help bring physicists one step closer to understanding the QGP formed in high-energy heavy-ion collisions.

REFERENCES

1 E. V. Shuryak. Phys. Rept. **61**, 71 (1980).

2 H. Satz, Nucl. Phys. A **418**, 4470 (1984).

3 J. J. Thomson. Philosophical Magazine **44**, 293 (1897).

4 S. Chatrchyan *et al*. (CMS Collaboration). Phys. Lett. B **716**, 30 (2012).

5 G. Aad *et al*. (ATLAS Collaboration). Phys. Lett. B **716**, 1 (2012).

6 P. L. Connolly *et al*. Phys. Rev. Lett. **10**, 371 (1963).

7 J. Beringer *et al*. (Particle Data Group Collaboration), Phys. Rev. D **86**, 010001 (2012).

8 M. Miller *et al*. Ann. Rev. Nucl. Part. Sci. **57**, 205 (2007).

9 R. A. Zaballa. PhD Dissertation, Georgia State University (2008).

10 A. B. Ayoub. The College Mathematics Journal **34**, 116 (2003).

11 R. S. Bhalero and J.-Y. Ollitrault. Phys. Lett. B **641**, 260 (2006).

12 B. Alver *et al*. Phys. Rev. C **77**, 014906 (2008).

13 B. Alver *et al*. arXiv:0805.4411 [nucl-ex].

14 P. Sorensen. arXiv:0905.0174 [nucl-ex].

15 W. Florkowski. *Phenomenology of Ultra-Relativistic Heavy-Ion Collisions*. World Scientific Publishing (2010).

16 J. W. Cronin *et al*. Phys. Rev. D **11**, 3105 (1975).

17 A. Accadri and M. Gyulassy. Phys. Lett B **586**, 244 (2004).

18 A. Adare *et al*. (PHENIX Collaboration). Phys. Rev. C **92**, 044909 (2015).

19 A. Adare *et al*. (PHENIX Collaboration). Phys. Rev. D **90**, 052002 (2014).

20 S. S. Adler *et al*. (PHENIX Collaboration). Phys. Rev. C **72**, 014903 (2005).

21 A. Adare *et al*. (PHENIX Collaboration). Phys. Rev. C **83**, 024909 (2011).

22 A. Adare *et al*. (PHENIX Collaboration) Phys. Rev. C **83**,052004 (2011).

23 S. S. Adler *et al*. (PHENIX Collaboration). Phys. Rev. Lett **94**, 082302 (2005).

24 A. Adare *et al*. (PHENIX Collaboration). Phys. Rev. C **90**, 034903 (2014).

25 B. I. Abelev *et al*. (STAR Collaboration). Phys. Rev. Lett **99**, 112301 (2007).

26 B. I. Abelev *et al*. (STAR Collaboration). Phys. Lett. B **673**, 183 (2009).

27 J. Adam *et al*. (ALICE Collaboration). arXiv:1506.09206 [nucl-ex].

28 B. B. Abelev *et al*. (ALICE Collaboration). Phys. Rev. C **91**, 024609 (2015).

29 A. Adare *et al*. (PHENIX Collaboration) arXiv:1509.06337 [nucl-ex].

30 I. Arsene *et al*. (BRAHMS Collaboration). Nucl. Phys. A **757**, 1 (2005).

31 B. B. Back *et al*. Nucl. Phys. A **757**, 28 (2005).

32 J. Adams *et al*. (STAR Collaboration). Nucl. Phys. A **757**, 102 (2005)

33 K. Adcox *et al*. (PHENIX Collaboration). Nucl. Phys. A **757**, 184 (2005).

34 K. Adcox *et al*. (PHENIX Collaboration). Nucl. Instrum. Methods Phys. Res., Sec. A **499**, 469 (2003).

35 H. Akikawa *et al*. (PHENIX Collaboration). Nucl. Instrum. Methods Phys. Res., Sec. A **499**, 537 (2003)

36 M. Allen *et al*. (PHENIX Collaboration). Nucl. Instrum. Methods Phys. Res., Sec. A **499**, 549 (2003)

37 A. Taketani *et al*. (PHENIX Collaboration). Nucl. Instrum. Methods Phys. Res., Sec. A **623**, 374 (2010).

38 C. Aidala *et al*. Nucl. Instrum. Methods Phys. Res., Sec. A **755**, 44 (2014).

39 C. Baglin *et al*. (NA38 Collaboration). Phys. Lett. B **220**, 471 (1989).

40 A. Adare *et al*. (PHENIX Collaboration). Phys. Rev. C **84**, 054912 (2011).

41 A. Adare *et al*. (PHENIX Collaboration). Phys. Rev. C **90**, 064908 (2014).

42 T. Sjostrand, P. Eden, C. Friberg, L. Lonnblad, G. Miu, S. Mrenna, and E. Norrbin. Comput. Phys. Commun. **135**, 238 (2001).

43 R. Brun, F. Carminati, and S. Giani. CERN-W5013 (1994).

44 L.-W. Chen and C. M. Ko. Phys. Rev. C **73**, 014906 (2006).

APPENDICES

Appendix A: PYTHIA 6.42 Configurations

Appendix A.1 ϕ Meson PYTHIA Configuration Code

```
roots   200
proj    p
targ    p
frame   cms
msel    1     // turn on QCD jets

mdme 579 1 0  // pi -> mu_nu turned off
mdme 630 1 0  // K -> mu_nu turned off
mdme 656 1 0  // phi -> K+K- turned off
mdme 657 1 0  // phi -> KLKS turned on
mdme 658 1 0  // phi -> rho- pi+ turned off
mdme 659 1 0  // phi -> rho0 pi0 turned off
mdme 660 1 0  // phi -> rho+ pi- turned on
mdme 661 1 0  // phi -> 3pi turned off
mdme 662 1 0  // phi -> gamma eta turned off
mdme 663 1 0  // phi -> pi0 gamma turned on
mdme 664 1 0  // phi -> ee turned off
mdme 665 1 1  // phi -> mumu turned on
mdme 666 1 0  // phi -> pi pi turned off

//insert the following lines to use CTEQ6
mstp    52 2  // usa LHAPDF
mstp    54 2
mstp    56 2
mstp    51 10041 // CTEQ6LL

parp 91 2.1  //set instrinsic kt value = 1.5
ckin    3  2.0  // min parton pt of 2.0
```

Appendix A.2 ρ Meson PYTHIA Configuration Code

```
roots   200
proj    p
targ    p
frame   cms
msel    1     // turn on QCD jets

mdme 579 1 0  // pi -> mu_nu turned off
mdme 630 1 0  // K -> mu_nu turned off
mdme 556 1 0  // rho -> pi pi  turned off
mdme 557 1 0  // rho -> pi0 gamma turned on
mdme 558 1 0  // rho -> eta gamma turned off
mdme 559 1 1  // rho -> mumu turned on
mdme 560 1 0  // rho -> e e turned off

//insert the following lines to use CTEQ6
mstp    52 2  // usa LHAPDF
mstp    54 2
mstp    56 2
mstp    51 10041 // CTEQ6LL

parp 91 2.1  //set instrinsic kt value = 1.5
ckin    3  2.0  // min parton pt of 2.0
```

Appendix A.3 ω Meson PYTHIA Configuration Code

```
roots   200
proj    p
targ    p
frame   cms
msel    1     // turn on QCD jets
pmas    113 1 0.78265 // change to omega mass from PDG 2011
pmas    113 2 0.00849 // change to omega width from PDG 2011
mdme 579 1 0  // pi -> mu_nu turned off
mdme 630 1 0  // K -> mu_nu turned off
mdme 556 1 0  // rho -> pi pi  turned off
mdme 557 1 0  // rho -> pi0 gamma turned off
mdme 558 1 0  // rho -> eta gamma turned off
mdme 559 1 1  // rho -> mumu turned on
mdme 560 1 0  // rho -> pi pi turned off
//mstp    51 7    // structure function for CTEQ5L
//mstp 51 4 // structure function for GRV94 L

//insert the following lines to use CTEQ6
mstp    52 2  // usa LHAPDF
mstp    54 2
mstp    56 2
mstp    51 10041 // CTEQ6LL

//parp 91 2.1 //set instrinsic kt value = 1.5
ckin    3  2.0  // min parton pt of 2.0
```

Appendix A.4 J/ψ Meson PYTHIA Configuration Code

```
roots   200
proj    p
targ    p
frame   cms
msel    0       // turn on all production mechanisms manually

msub 86 1 // g+g->j/psi
msub 106 1 // g+g->j/psi+gamma
msub 107 1 // g+gamma->j/psi+g
msub 108 1 // gamma+gamma->j/psi+gamma

mdme 858 1 0 // J/Psi -> ee turned OFF
mdme 859 1 1 // J/Psi -> mumu turned ON
mdme 860 1 0 // J/JPsi -> random turned OFF

//mstp 51 7 // structure function for CTEQ5L

//insert the following lines to use CTEQ6
mstp    52 2  // usa LHAPDF
mstp    54 2
mstp    56 2
mstp    51 10041 // CTEQ6LL
```